https://doi.org/10.5194/gmd-2019-291
Preprint. Discussion started: 26 November 2019
© Author(s) 2019. CC BY 4.0 License.

Geoscientific Model Development Discussions

ESMValTool v2.0 – Extended set of large-scale diagnostics for quasi-operational and comprehensive evaluation of Earth system models in CMIP

Veronika Eyring[1,2], Lisa Bock[1], Axel Lauer[1], Mattia Righi[1], Manuel Schlund[1], Bouwe Andela[3], Enrico Arnone[4,5], Omar Bellprat[6], Björn Brötz[1], Louis-Philippe Caron[6], Nuno Carvalhais[7,8], Irene Cionni[9], Nicola Cortesi[6], Bas Crezee[10], Edouard Davin[10], Paolo Davini[4], Kevin Debeire[1], Lee de Mora[11], Clara Deser[12], David Docquier[13], Paul Earnshaw[14], Carsten Ehbrecht[15], Bettina K. Gier[2,1], Nube Gonzalez-Reviriego[6], Paul Goodman[16], Stefan Hagemann[17], Steven Hardiman[14], Birgit Hassler[1], Alasdair Hunter[6], Christopher Kadow[18], Stephan Kindermann[15], Sujan Koirala[7], Nikolay Koldunov[19,20], Quentin Lejeune[10,21], Valerio Lembo[22], Tomas Lovato[23], Valerio Lucarini[22,24,25], François Massonnet[13], Benjamin Müller[26], Amarjiit Pandde[16], Núria Pérez-Zanón[6], Adam Phillips[12], Valeriu Predoi[27], Joellen Russell[16], Alistair Sellar[14], Federico Serva[28], Tobias Stacke[29], Ranjini Swaminathan[30], Verónica Torralba[6], Javier Vegas-Regidor[6], Jost von Hardenberg[4,31], Katja Weigel[2,1], and Klaus Zimmermann[32]

[1]Deutsches Zentrum für Luft- und Raumfahrt (DLR), Institut für Physik der Atmosphäre, Oberpfaffenhofen, Germany
[2]University of Bremen, Institute of Environmental Physics (IUP), Bremen, Germany
[3]Netherlands eScience Center, Science Park 140, 1098 XG Amsterdam, the Netherlands
[4]Institute of Atmospheric Sciences and Climate, Consiglio Nazionale delle Ricerche (ISAC-CNR), Italy
[5]Department of Physics, University of Torino, Italy
[6]Barcelona Supercomputing Center (BSC), Barcelona, Spain
[7]Department of Biogeochemical Integration, Max Planck Institute for Biogeochemistry, Jena, Germany.
[8]Departamento de Ciências e Engenharia do Ambiente, DCEA, Faculdade de Ciências e Tecnologia, FCT, Universidade Nova de Lisboa, 2829-516 Caparica, Portugal
[9]Agenzia nazionale per le nuove tecnologie, l'energia e lo sviluppo economico sostenibile (ENEA), Rome, Italy
[10]ETH Zurich, Institute for Atmospheric and Climate Science, Zurich, Switzerland
[11]Plymouth Marine Laboratory (PML), Plymouth, UK
[12]National Center for Atmospheric Research (NCAR), Boulder, CO, USA
[13]Georges Lemaître Centre for Earth and Climate Research, Earth and Life Institute, Université catholique de Louvain, Louvain-la-Neuve, Belgium
[14]Met Office, Exeter, UK
[15]Deutsches Klimarechenzentrum, Hamburg, Germany
[16]Department of Geosciences, University of Arizona, Tucson, AZ, USA
[17]Institute of Coastal Research, Helmholtz-Zentrum Geesthacht (HZG), Geesthacht, Germany
[18]Freie Universität Berlin (FUB), Berlin, Germany
[19]MARUM, Center for Marine Environmental Sciences, Bremen, Germany
[20]Alfred-Wegener-Institut Helmholtz-Zentrum für Polar- und Meeresforschung, Bremerhaven, Germany
[21]Climate Analytics, Berlin, Germany
[22]CEN, University of Hamburg, Meteorological Institute, Hamburg, Germany
[23]Fondazione Centro Euro-Mediterraneo sui Cambiamenti Climatici (CMCC), Bologna, Italy
[24]Department of Mathematics and Statistics, University of Reading, Department of Mathematics and Statistics, Reading, UK
[25]Centre for the Mathematics of Planet Earth, University of Reading, Centre for the Mathematics of Planet Earth Department of Mathematics and Statistics, Reading, UK
[26]Ludwig Maximilians Universität (LMU), Department of Geography, Munich, Germany
[27]NCAS Computational Modelling Services (CMS), University of Reading, Reading, UK
[28]Institute of Marine Sciences, Consiglio Nazionale delle Ricerche (ISMAR-CNR), Italy
[29]Max Planck Institute for Meteorology (MPI-M), Hamburg, Germany
[30]Department of Meteorology, University of Reading, Reading, UK
[31]Department of Environment, Land and Infrastructure Engineering, Politecnico di Torino, Turin, Italy
[32]Rossby Centre, Swedish Meteorological and Hydrological Institute (SMHI), Sweden

Correspondence to: Veronika Eyring (veronika.eyring@dlr.de)

https://doi.org/10.5194/gmd-2019-291
Preprint. Discussion started: 26 November 2019
© Author(s) 2019. CC BY 4.0 License.

Geoscientific Model Development Discussions

Abstract. The Earth System Model Evaluation Tool (ESMValTool) is a community diagnostics and performance metrics tool designed to improve comprehensive and routine evaluation of Earth System Models (ESMs) participating in the Coupled Model Intercomparison Project (CMIP). It has undergone rapid development since the first release in 2016 and is now a well-tested tool that provides end-to-end provenance tracking to ensure reproducibility. It consists of an easy-to-install, well documented Python package providing the core functionalities (ESMValCore) that performs common pre-processing operations and a diagnostic part that includes tailored diagnostics and performance metrics for specific scientific applications. Here we describe large-scale diagnostics of the second major release of the tool that supports the evaluation of ESMs participating in CMIP Phase 6 (CMIP6). ESMValTool v2.0 includes a large collection of diagnostics and performance metrics for atmospheric, oceanic, and terrestrial variables for the mean state, trends, and variability. ESMValTool v2.0 also successfully reproduces figures from the evaluation and projections chapters of the Intergovernmental Panel on Climate Change (IPCC) Fifth Assessment Report (AR5) and incorporates updates from targeted analysis packages, such as the NCAR Climate Variability Diagnostics Package for the evaluation of modes of variability the Thermodynamic Diagnostic Tool (TheDiaTo) to evaluate the energetics of the climate system, as well as parts of AutoAssess that contains a mix of top-down performance metrics. The tool has been fully integrated into the Earth System Grid Federation (ESGF) infrastructure at the Deutsches Klima Rechenzentrum (DKRZ) to provide evaluation results from CMIP6 model simulations shortly after the output is published to the CMIP archive. A result browser has been implemented that enables advanced monitoring of the evaluation results by a broad user community at much faster timescales than what was possible in CMIP5.

1. Introduction

The Intergovernmental Panel on Climate Change (IPCC) Fifth Assessment Report (AR5) concluded that the warming of the climate system is unequivocal and that the human influence on the climate system is clear (IPCC, 2013). Observed increases of greenhouse gases, warming of the atmosphere and ocean, sea ice decline, and sea level rise, in combination with climate model projections of a likely temperature increase between 2.1 and 4.7°C for a doubling of atmospheric CO_2 concentration, make it an international priority to improve our understanding of the climate system and to reduce greenhouse gas emissions. This is reflected for example in the Paris Agreement of the United Nations Framework Convention on Climate Change (UNFCCC) 21st session of the Conference of the Parties (COP21, UNFCCC (2015)).

Simulations with climate and Earth System Models (ESMs) performed by the major climate modelling centres around the world under common protocols are coordinated as part of the World Climate Research Programme (WCRP) Coupled Model Intercomparison Project (CMIP) since the early 90s (Eyring et al., 2016a; Meehl et al., 2000; Meehl et al., 2007; Taylor et al., 2012). CMIP simulations provide a fundamental source for IPCC Assessment Reports and for improving understanding of past, present and future climate change. Standardization of model output in a common format (Juckes et al., 2019) and publication of the CMIP model output on the Earth System Grid Federation (ESGF) facilitates multi-model evaluation and analysis (Balaji et al., 2018; Eyring et al., 2016b). This effort is additionally supported by observations for Model Intercomparison Project (obs4MIPs, Ferraro et al. (2015)) which provides the community with access to CMIP-like datasets (in terms of variables definitions, temporal and spatial coordinates, time frequencies and coverages) of satellite data. The

https://doi.org/10.5194/gmd-2019-291
Preprint. Discussion started: 26 November 2019
© Author(s) 2019. CC BY 4.0 License.

Geoscientific Model Development Discussions

availability of observations and models in the same format strongly facilitates model evaluation and analysis, but the full rewards of the effort devoted to this activity were yet to be realized.

CMIP is now in its 6th phase (CMIP6, Eyring et al. (2016a)) and is confronted with a number of new challenges. More centres are running more versions of more models of increasing complexity. An ongoing demand to resolve more processes requires increasingly higher model resolutions. Accordingly, the data volume of 2 PB in CMIP5 is expected to grow by a factor of 10-20 for CMIP6, resulting in a database of between 20 and 40 PB, depending on model resolution and the number of modelling centres ultimately contributing to the project. Archiving, documenting, subsetting, supporting, distributing, and analysing the huge CMIP6 output together with observations challenges the capacity and creativity of the largest data centres and fastest data networks. In addition, the growing dependency on CMIP products by a broad research community and by national and international climate assessments, as well as the increasing desire for operational analysis in support of mitigation and adaptation, means that a system has to be set in place that allows for an efficient and comprehensive analysis of the large volume of data from models and observations.

To achieve this, the Earth System Model Evaluation Tool (ESMValTool) is developed. A first version that was tested on CMIP5 models was released in 2016 (Eyring et al., 2016c). With the release of ESMValTool version 2.0 (v2.0), for the first time in CMIP an evaluation tool is now available that provides results from CMIP6 simulations as soon as the model output is published to the ESGF (https://cmip-esmvaltool.dkrz.de/). This is realized through text files that we refer to as recipes, each calling a certain set of diagnostics and performance metrics to reproduce analyses that have demonstrated to be of importance in ESM evaluation in previous peer-reviewed papers or assessment reports. The ESMValTool is developed as a community diagnostics and performance metrics tool that allows for routine comparison of single or multiple models, either against predecessor versions or against observations. It is developed as a community-effort currently involving more than 40 institutes with a rapidly growing developer and user community. It allows for full tractability and provenance of all figures and outputs produced.

The release of ESMValTool v2.0 is described in four companion papers: Righi et al. (2019) provide the technical overview of ESMValTool v2.0 and show a schematic representation of the *ESMValCore*, a Python package that provides the core functionalities, and the *Diagnostic Part* in their Figure 1. This paper describes recipes of the *Diagnostic Part* for the evaluation of large-scale diagnostics. Recipes for extreme events and in support of regional model evaluation are described by Weigel et al. (2019) and recipes for emergent constraints and model weighting by Lauer et al. (2019). The use of the tool is demonstrated by showing example figures for each recipe for either all or a subset of CMIP5 models. Section 2 describes the type of modelling and observational data currently supported by ESMValTool v2.0. In Section 3 an overview of the recipes for large-scale diagnostics provided with the ESMValTool v2.0 release is given along with their diagnostics and performance metrics and the variables and observations used. Section 4 describes the workflow of routine analysis of CMIP model output alongside the ESGF and the ESMValTool result browser. Section 5 closes with a summary and an outlook.

2. Models and observations

The open-source release of ESMValTool v2.0 that accompanies this paper is intended to work with CMIP5 and CMIP6 model output (and partly also with CMIP3), but the tool is compatible with any arbitrary model output, provided that it is in CF-compliant netCDF format and that the variables and metadata are following the CMOR

https://doi.org/10.5194/gmd-2019-291
Preprint. Discussion started: 26 November 2019
© Author(s) 2019. CC BY 4.0 License.

tables and definitions. As in ESMValTool v1.0, for the evaluation of the models with observations, we make use of the large observational effort to deliver long-term, high quality observations from international efforts such as observation for Model Intercomparison Project (obs4MIPs, Ferraro et al. (2015)) or observations from the ESA Climate Change Initiative (CCI), Lauer et al. (2017)). In addition, observations from other sources and reanalyses data are used in several diagnostics. The technical treatment of observations in ESMValTool v2.0 is described in Righi et al. (2019). The observations used by individual recipes and diagnostics are described in Section 3.

3. Overview of recipes included in ESMValTool v2.0

In this section, all recipes for large-scale diagnostics that have been newly added in v2.0 since the first release of the ESMValTool in 2016 (see Table 1 in Eyring et al. (2016c) for an overview of namelists (now called recipes) included in v1.0) are described. In each subsection, we first scientifically motivate the inclusion of the recipe by reviewing the main systematic biases in current ESMs and their importance and implications. We then give an overview of the recipes that can be used to evaluate such biases along with the diagnostics and performance metrics included, and the required variables and corresponding observations that are used in ESMValTool v2.0. For each recipe we provide 1-2 example figures that are applied to either all or a subset of the CMIP5 models. An assessment of CMIP5 or CMIP6 models is however not the focus of this paper. Rather, we attempt to illustrate how the recipes contained within ESMValTool v2.0 can facilitate the development and evaluation of climate models in the targeted areas. Therefore, the results of each figure are only briefly described in each figure caption. Table 1 provides a summary of all recipes included in ESMValTool v2.0 along with a short description, information on the quantities and ESMValTool variable names for which the recipe is tested and the corresponding diagnostic scripts.

We describe recipes separately for integrative measures of model performance (Section 3.1) and for the evaluation of processes in the atmosphere (Section 3.2), ocean and cryosphere (Section 3.3), land (Section 3.4), and biogeochemistry (Section 3.5). Recipes that reproduce chapters from the evaluation chapter of the IPCC Fifth Assessment Report (Flato et al., 2013) are described within these sections.

3.1 Integrative Measures of Model Performance

3.1.1 Performance metrics for essential climate variables for the atmosphere, ocean, sea ice and land

Performance metrics are quantitative measures of agreement between a simulated and observed quantity. Various statistical measures can be used to quantify differences between individual models or generations of models and observations. Atmospheric performance metrics were already included in *namelist_perfmetrics_CMIP5.nml* of ESMValTool v1.0. This recipe has now been extended to include additional atmospheric variables as well as new variables from the ocean, sea-ice and land. Similar to Figure 9.7 of Flato et al. (2013), Figure 1 shows the relative space-time root mean square error (RMSE) for the CMIP5 historical simulations (1980-2005) against a reference observation and, where available, an alternative observational data set [*recipe_perfmetrics_CMIP5.yml*]. Additional variables can be easily added if observations are available, see further details in Section 4.1.1 of Eyring et al. (2016c). In addition to the performance metrics displayed in Figure 1, several other quantitative measures of model performance are included in some of the recipes and are described throughout the respective sections of this paper.

https://doi.org/10.5194/gmd-2019-291
Preprint. Discussion started: 26 November 2019
© Author(s) 2019. CC BY 4.0 License.

Geoscientific Model Development Discussions
Open Access
EGU

3.1.2. Centered pattern correlations for different CMIP ensembles

Another example of a performance metric is the pattern correlation between the observed and simulated climatological annual mean spatial patterns. Following Figure 9.6 of the IPCC AR5 (Chapter 9, Flato et al. (2013)), a diagnostic for computing and plotting centered pattern correlations for different models and CMIP ensembles has been implemented (Figure 2) and added to *recipe_flato13ipcc.yml*. The variables are first regridded to a 4°x5° longitude by latitude grid to not favour specific model resolutions. The centered pattern correlations, which measure the similarity of two patterns after removing the global mean, are computed against a reference observation. Should the input models be from different CMIP ensembles, they are grouped by ensemble and each ensemble is plotted side by side per variable with a different colour. If an alternate model is given, it is shown as a solid green circle. The axis ratio of the plot reacts dynamically to the number of variables (n_var) and ensembles (n_ensemble) after it surpasses a combined number of n_var*n_ensemble = 16, and the y-axis range is calculated to encompass all values. The centered pattern correlation is good to see both the spread in models within a single variable, as well as a quick overview of how well other variables and aspects of the climate on a large scale are reproduced with respect to observations. Furthermore when using several ensembles, the progress made by each ensemble on a variable basis can be seen at a quick glance.

3.1.3 Single model performance index

Most model performance metrics only display the skill for a specific model and a specific variable at a time, not making an overall index for a model. This works well when only a few variables or models are considered, but can result in an overload of information for a multitude of variables and models. Following Reichler and Kim (2008), a Single Model Performance Index (SMPI) has been implemented in *recipe_smpi.yml*. The SMPI (called "I2") is based on the comparison of several different climate variables (atmospheric, surface and oceanic) between climate model simulations and observations or reanalyses, and evaluates the time-mean state of climate. For I2 to be determined, the differences between the climatological mean of each model variable and observations at each of the available data grid points are calculated, and scaled to the interannual variance from the validating observations. This interannual variability is determined by performing a bootstrapping method (random selection with replacement) for the creation of a large synthetic ensemble of observational climatologies. The results are then scaled to the average error from a reference ensemble of models, and in a final step the mean over all climate variables and one model is calculated. The plot shows the I2 values for each model (orange circles) and the multi-model mean (black circle), with the diameter of each circle representing the range of I2 values encompassed by the 5th and 95th percentiles of the bootstrap ensemble (Figure 3). The I2 values vary around one, with values greater than one for underperforming models, and values less than one for more accurate models. This diagnostic requires that all models have input for all of the variables considered, as this is the basis to have a comparable I2.

3.1.4 Auto-Assess

While highly condensed metrics are useful for comparing a large number of models, for the purpose of model development it is important to retain granularity on which aspects of model performance have changed, and why. For this reason, many modelling centres have their own suite of metrics which they use to compare candidate model versions against a predecessor. AutoAssess is such a system, developed by the UK Met Office and used in the development of HadGEM3 and UKESM1. The output of AutoAssess contains a mix of top-down metrics

https://doi.org/10.5194/gmd-2019-291
Preprint. Discussion started: 26 November 2019
© Author(s) 2019. CC BY 4.0 License.

evaluating key model output variables (e.g. temperature and precipitation) and bottom-up metrics which assess the realism of model processes and emergent behaviour such as cloud variability and El Niño–Southern Oscillation (ENSO). The output of AutoAssess includes around 300 individual metrics. To facilitate interpretation of the results they are grouped into 11 thematic areas, ranging from the broad-scale such as global tropic circulation and stratospheric mean state and variability, to the region- and process-specific, such as monsoon regions and the hydrological cycle.

It is planned that all the metrics currently in AutoAssess will be implemented in ESMValTool. At this time, a single assessment area (group of metrics) has been included as a technical demonstration: that for the stratosphere. These metrics have been implemented in a set of recipes named *recipe_autoassess_*.yml*. They include metrics of the Quasi-Biennial Oscillation (QBO) as a measure of tropical variability in the stratosphere. Zonal mean zonal wind at 30hPa is used to define metrics for the period and amplitude of the QBO. Figure 4 shows the downward propagation of the QBO for a single model using zonal mean zonal wind averaged between 5S and 5N. Metrics are also defined for the tropical tropopause cold point (100hPa, 10S-10N) temperature, and stratospheric water vapour concentrations at entry point (70hPa, 10S-10N). The cold point temperature is an important factor determining the entry point humidity, which in turn is important for the accurate simulation of stratospheric chemistry and radiative balance (Hardiman et al., 2015). Other metrics characterise the realism of the stratospheric easterly jet and polar night jet.

3.2 Diagnostics for the evaluation of processes in the atmosphere

3.2.1 Multi-model mean bias for temperature and precipitation

Near-surface air temperature (tas) and precipitation (pr) are the two variables most commonly requested by users of ESM simulations. Often, diagnostics for tas and pr are shown for the multi-model mean of an ensemble. Both of these variables are the end result of numerous interacting processes in the models, making it challenging to understand and improve biases in these quantities. For example, near surface air temperature biases depend on the models' representation of radiation, convection, clouds, land characteristics, surface fluxes, as well as atmospheric circulation and turbulent transport (Flato et al., 2013), each with their own potential biases that may either augment or oppose one another.

The diagnostic that calculates the multi model mean bias compared to a reference data set is part of the *recipe_flato13ipcc.yml* and reproduces Figures 9.2 and 9.4 of Flato et al. (2013). We extended the *namelist_flato13ipcc.xml* of ESMValTool v1.0 by adding the mean root mean square error of the seasonal cycle with respect to the reference dataset. Figures 5 and 6 show the CMIP5 multi-model average as absolute values and as biases for the annual mean surface air temperature relative to ERA-Interim and precipitation relative to the Global Precipitation Climatology Project (GPCP, Adler et al. (2003)) data, respectively. Figure 7 shows observed and simulated time series of the anomalies in annual and global mean surface temperature. The model datasets are subsampled by the HadCRUT4 observational data mask (Morice et al., 2012) and pre-processed as described by Jones et al. (2013). The figure reproduces Figure 9.8 of Flato et al. (2013) and is part of *recipe_flato13ipcc.yml*.

3.2.2 Precipitation quantile bias

Precipitation is a dominant component of the hydrological cycle, and as such a main driver of the climate system and human development. The reliability of climate projections and water resources strategies therefore depends

https://doi.org/10.5194/gmd-2019-291
Preprint. Discussion started: 26 November 2019
© Author(s) 2019. CC BY 4.0 License.

on how well precipitation can be reproduced by the models used for simulations. While CMIP5 models can reproduce the main patterns of mean precipitation (e.g., compared to observational data from GPCP (Adler et al., 2003)), they often show shortages and biases under particular conditions. Comparison of precipitation from CMIP5 models and observations shows a general good agreement for mean values at large scale (Kumar et al., 2013; Liu et al., 2012). Models carry a poor representation of frontal, convective, and mesoscale processes, resulting in substantial biases (Mehran et al., 2014) at regional scale: models tend to overestimate precipitation over complex topography and underestimate it especially over arid or peculiar subcontinental regions as for example northern Eurasia, eastern Russia, and central Australia. Biases are typically stronger at high quantiles of precipitation, making the study of precipitation quantile biases an effective diagnostic for addressing the quality of simulated precipitation. The *recipe_quantilebias.yml* implements calculation of the quantile bias to allow evaluation of the precipitation bias based on a user defined quantile in models as compared to a reference dataset following Mehran et al. (2014). The quantile bias (QB) is defined as the ratio of monthly precipitation amounts in each simulation to that of the reference dataset above a specified threshold t (e.g., the 75th percentile of all the local monthly values). An example is reported in Figure 8, where gridded observational data from the GPCP project were adopted. A quantile bias equal to 1 indicates no bias in the simulations, whereas a value above (below) 1 corresponds to a climate model's overestimation (underestimation) of the precipitation amount above the specified threshold t, with respect to that of the reference dataset. The recipe allows evaluation of the precipitation bias based on a user defined quantile in models as compared to the reference dataset.

3.2.3 Atmospheric dynamics

3.2.3.1 Stratosphere-troposphere coupling

The current generation of climate models include the representation of stratospheric processes, as the vertical coupling with the troposphere is important for the weather and climate at the surface (Baldwin and Dunkerton, 2001). Stratosphere-resolving models are able to internally generate realistic annular modes of variability in the extratropical atmosphere (Charlton-Perez et al., 2013) which are however too persistent in the troposphere and delayed in the stratosphere compared to reanalysis (Gerber et al., 2010), leading to biases in the simulated impacts on surface conditions.

The recipe *recipe_zmnam.yml* can be used to evaluate the representation of the Northern Annular Mode (NAM, (Wallace, 2000)) in climate simulations, using reanalysis datasets as reference. The calculation is based on the "zonal mean algorithm" of Baldwin and Thompson (2009), and is an alternative to pressure based or height-dependent methods. This approach provides a robust description of the stratosphere-troposphere coupling on daily timescales, requiring less subjective choices and a reduced amount of input data. Starting from daily mean geopotential height on pressure levels, the leading empirical orthogonal function/principal component are computed from zonal mean daily anomalies, with the principal component representing the zonal mean NAM index. The regression of the monthly mean geopotential height onto this monthly averaged index represents the NAM pattern for each selected pressure level. The outputs of the procedure are the time series (Figure 9, left) and the histogram (not shown) of the zonal-mean NAM index, and the regression maps for selected pressure levels (Figure 9, right). The users can select the specific datasets (climate model simulation and/or reanalysis) to be evaluated, and a subset of pressure levels of interest.

https://doi.org/10.5194/gmd-2019-291
Preprint. Discussion started: 26 November 2019
© Author(s) 2019. CC BY 4.0 License.

3.2.3.2 Atmospheric blocking indices

Atmospheric blocking is a recurrent mid-latitude weather pattern identified by a large-amplitude, quasi-stationary, long-lasting, high-pressure anomaly that ‘‘blocks’’ the westerly flow forcing the jet stream to split or meander (Rex, 1950). It is typically initiated by the breaking of a Rossby wave in a region at the exit of the storm track, where it amplifies the underlying stationary ridge (Tibaldi and Molteni, 1990). Blocking occurs more frequently in the Northern Hemisphere cold season, with larger frequencies observed over the Euro-Atlantic and North Pacific sectors. Its lifetime oscillates from a few days up to several weeks (Davini et al., 2012). To this day atmospheric blocking still represents an open issue for the climate modelling community since state-of-the-art weather and climate models show limited skill in reproducing it (Davini and D’Andrea, 2016; Masato et al., 2013). Models are indeed characterized by large negative bias over the Euro-Atlantic sector, a region where blocking is often at the origin of extreme events, leading to cold spells in winter and heat waves in summer (Coumou and Rahmstorf, 2012; Sillmann et al., 2011).

Several objective blocking indices have been developed aimed at identifying different aspects of the phenomenon (see Barriopedro et al. (2010) for details). The recipe *recipe_miles_block.yml* integrates diagnostics from the Mid-Latitude Evaluation System – MiLES v0.51 (Davini, 2018) tool in order to calculate two different blocking indices based on the reversal of the meridional gradient of daily 500 hPa geopotential height. The first one is a 1-d index, namely the Tibaldi and Molteni (1990) blocking index, here adapted to work with 2.5x.2.5 grids. Blocking is defined when the reversal of the meridional gradient at geopotential height at 60°N is detected, i.e. when easterly winds are found in the mid-latitudes. The second one is the atmospheric blocking index following Davini et al. (2012). It is a 2-d extension of Tibaldi and Molteni (1990) covering latitudes from 30°N up to 75°N. The recipe computes both the Instantaneous Blocking frequencies and the Blocking Events frequency (which includes both spatial and 5-day-minimum temporal constraints). It reports also two intensity indices, i.e. the Meridional Gradient Index and the Blocking Intensity index, and it evaluates the wave breaking characteristic associated with blocking (i.e. cyclonic or anticyclonic) through the Rossby wave orientation index. A supplementary Instantaneous Blocking index (named “ExtraBlock”) including an extra condition to filter out low-latitude blocking events is also provided. The recipe compares multiples datasets against a reference one (default is ERA-Interim) and provides output (in NetCDF4 Zip format) as well as figures for the climatology of each diagnostic. An example output is shown in Figure 10.

3.2.4 Thermodynamics of the climate system

The climate system can be seen as a forced and dissipative non-equilibrium thermodynamic system (Lucarini et al., 2014), converting potential into mechanical energy, and generating entropy via a variety of irreversible processes The atmospheric and oceanic circulation are caused by the inhomogeneous absorption of solar radiation, and, all in all, they act in such a way to reduce the temperature gradients across the climate system. When assessing model performances, this allows developing a comprehensive set of interrelated metrics, explaining climate variability over a large variety of scales and linking it to the first principles of physics. One of these metrics is the Top-of-Atmosphere (TOA) energy budget. At steady-state, assuming stationarity, the long term energy input and output should balance. Previous studies have shown that this is essentially not the case, and most of the models are affected by non-negligible energy drift (Lucarini et al., 2011; Mauritsen et al., 2012)). This severely impacts the prediction capability of state-of-the-art models, given that most of the energy imbalance is known to be taken up by oceans (Exarchou et al., 2015). This is why increasing attention is being

https://doi.org/10.5194/gmd-2019-291
Preprint. Discussion started: 26 November 2019
© Author(s) 2019. CC BY 4.0 License.

devoted to the retrieval of a consistent dataset of observational-based ocean heat uptake measurements (Von Schuckmann et al., 2016). Nonetheless, global energy biases are also associated to inconsistent thermodynamic treatment of processes taking place in the atmosphere, as the dissipation of kinetic energy (Lucarini et al., 2011) and of the water mass balance inside the hydrological cycle (Liepert and Previdi, 2012; Wild and Liepert, 2010). Climate models feature substantial disagreements in the peak intensity of the meridional heat transport, both in the ocean and in the atmospheric parts, whereas the position of the peaks of the (atmospheric) transport blocking are consistently captured (Lucarini and Pascale, 2014). In the atmosphere, these issues are related to inconsistencies in the models' ability to reproduce the mid-latitude atmospheric variability (Di Biagio et al., 2014; Lucarini et al., 2007) and intensity of the Lorenz Energy Cycle (Marques et al., 2011). Energy and water mass budgets, as well as the treatment of the hydrological cycle and atmospheric dynamics, all affect the material entropy production in the climate system, i.e. the entropy production related to irreversible processes in the system. Various methods have been proposed to account for that (Ambaum, 2010; Fraedrich et al., 2008; Lucarini and Ragone, 2011; Romps, 2008). It is possible to estimate the entropy production either via an indirect method, based on the radiative heat convergence in the atmosphere (the ocean accounts only for a minimal part of the entropy production), or via a direct method, based on the explicit computation of entropy production due to all irreversible processes (Goody, 2000). Ideally, the two methods are known to be equivalent, but differences emerge when considering coarse-grained data in space and/or in time (Lucarini and Pascale, 2014). Resolving subgrid-scale processes has long been known to be a critical issue, when attempting to provide an accurate climate entropy budget (Gassmann and Herzog, 2015; Kleidon and Lorenz, 2004; Kunz et al., 2008). While some systematic estimates of entropy production by climate models have been produced with the indirect method (Lucarini and Pascale, 2014), an extensive comparison with the estimates resulting from the direct method is to our best knowledge still lacking, due to the limited availability of climate model outputs with the necessary temporal and spatial resolution.

In the current release the diagnostic tool for thermodynamics of the climate system contains a number of independent modules for: (a) energy budgets and meridional heat transports, (b) water mass and latent energy budget, (c) Lorenz Energy Cycle, (d) material entropy production with either the indirect/direct method or both. The code is set to ingest monthly mean gridded datasets for the modules (a), (b), and (d). Daily mean data are required for the computation of the Lorenz Energy Cycle (c). The intensity of the Lorenz Energy Cycle is used for computation of the material entropy production with the direct method. If (c) is not performed, a reference value for material entropy production due to kinetic energy dissipation is provided. Input variables are monthly mean radiative fluxes at TOA and at the surface, surface turbulent latent and sensible heat fluxes, surface temperature, near-surface specific humidity, snowfall and total precipitation, surface pressure. The daily mean 3-dimensional fields of velocity, temperature, the two components of the near-surface horizontal velocity and near-surface temperature are required for the computation of the Lorenz Energy Cycle. If a land-sea mask is provided, energy and water mass budgets are also separately computed over oceans and continents. The outputs of the diagnostic modules are provided as annual mean quantities in NetCDF format. When possible (energy budgets, water mass and latent energy budgets, components of the material entropy production with the indirect method) horizontal maps for the average of annual means are provided. For the meridional heat transports, annual mean meridional sections are shown (Figure 11) (Lembo et al., 2017; Lucarini and Pascale, 2014; Trenberth et al., 2001). For the Lorenz Energy Cycle, a flux diagram (Ulbrich et al., 1991), showing all the storage, conversion, source and sink terms for every year, is provided (Figure 12). When a multi-model ensemble is provided, global

https://doi.org/10.5194/gmd-2019-291
Preprint. Discussion started: 26 November 2019
© Author(s) 2019. CC BY 4.0 License.


metrics are related in scatter plots, where each dot is a member of the ensemble, and the multi-model mean, together with uncertainty range, is displayed. An output log file contains all the information about the time-averaged global mean values, including all components of the material entropy production budget. The diagnostic tool is run through the recipe *recipe_thermodyn_diagtool.yml*, where the user can also specify the options on which modules have to be run. An extensive explanation of the methods used and a discussion of results with a subset of CMIP5 datasets can be found in Lembo et al. (2019) who describe the Thermodynamic Diagnostic Tool (TheDiaTo) v1.0.

3.2.5 Natural modes of climate variability and weather regimes

3.2.5.1. NCAR Climate Variability Diagnostic Package

Natural modes of climate variability co-exist with externally-forced climate change, and have large impacts on climate, especially at regional and decadal scales. These modes of variability are due to processes intrinsic to the coupled climate system, and exhibit limited predictability. As such, they complicate model evaluation and model inter-comparison, and confound assessments of anthropogenic influences on climate (Bengtsson and Hodges, 2019; Deser et al., 2012; Deser et al., 2014; Deser et al., 2017; Kay et al., 2015; Suárez-Gutiérrez et al., 2017). Despite their importance, systematic evaluation of these modes in Earth system models remains a challenge du to the wide range of phenomena to consider, the length of record needed to adequately characterize them, and uncertainties in the short observational data sets (Deser et al., 2010; Frankignoul et al., 2017; Simpson et al., 2018). While the temporal sequences of internal variability in models need not match those in the single realization of nature, their statistical properties (e.g., time scale, autocorrelation, spectral characteristics, and spatial patterns) need to be realistically simulated for credible climate projections.

In order to assess natural modes of climate variability in models, the NCAR Climate Variability Diagnostics Package (CVDP, Phillips et al. (2014)) has been implemented into the ESMValTool. The CVDP has been developed as a standalone tool. To allow for easy updating of the CVDP once a new version is released, the structure of the CVDP is kept in its original form and a single recipe *recipe_CVDP.yml* has been written to enable the CVDP to be run directly within ESMValTool. The CVDP facilitates evaluation of the major modes of climate variability, including ENSO (Deser et al., 2010), the Pacific Decadal Oscillation (PDO, (Deser et al., 2010; Mantua et al., 1997)), the Atlantic Multi-decadal Oscillation (AMO, Trenberth and Shea (2006)), the Atlantic Meridional Overturning Circulation (AMOC, Danabasoglu et al. (2012)), and atmospheric teleconnection patterns such as the Northern and Southern Annular Modes (NAM and SAM; (Hurrell and Deser, 2009; Thompson and Wallace, 2000)), North Atlantic Oscillation (NAO, Hurrell and Deser (2009)), and Pacific North and South American (PNA and PSA, Thompson and Wallace (2000)), patterns. For details on the actual calculation of these modes in CVDP we refer to the original CVDP package and explanations available at http://www.cesm.ucar.edu/working_groups/CVC/cvdp/.

Depending on the climate mode analysed, the CVDP package uses the following variables: precipitation (pr), sea level pressure (psl), near-surface air temperature (tas), skin temperature (ts), snow depth (snd), sea ice concentration (siconc), and basin-average ocean meridional overturning mass stream function (msftmz). The models are evaluated against a wide range of observations and reanalysis data, for example Berkeley Earth System Temperature (BEST) for near-surface air temperature, Extended Reconstructed Sea Surface Temperature v5 (ERSSTv5) for skin temperature, and ERA-20C extended with ERA-Interim for sea level pressure. Additional observations or reanalysis can be added by the user for these variables. The ESMValTool v2.0 recipe

https://doi.org/10.5194/gmd-2019-291
Preprint. Discussion started: 26 November 2019
© Author(s) 2019. CC BY 4.0 License.

runs on all CMIP5 models. As examples, Figure 13 shows the representation of ENSO teleconnections during the peak phase (December-February) and Figure 14 the representation of the AMO as simulated by 41 CMIP5 models and observations during the historical period.

3.2.5.2 Weather regimes

Weather Regimes (WRs) refer to recurrent large-scale atmospheric circulation structures that allow the characterization of complex atmospheric dynamics in a particular region (Michelangeli et al., 1995; Vautard, 1990). The identification of WRs reduces the continuum of atmospheric circulation to a few recurrent and quasi-stationary (persistent) patterns. WRs have been extensively used to investigate atmospheric variability at the mid-latitudes, as they are associated with extreme weather events such as heat waves or droughts (Yiou et al., 2008). For example, there is a growing recognition of their significance especially over the Euro-Atlantic sector during the winter season, where four robust weather regimes have been identified - namely the NAO+, NAO-, Atlantic Ridge and Scandinavian Blocking (Cassou et al., 2005). These WRs can also be used as a diagnostic tool to investigate the performance of state-of-the-art climate forecast systems: difficulties in reproducing the Atlantic Ridge and the Scandinavian blocking have been often observed (Dawson et al., 2012; Ferranti et al., 2015). Forecast systems which are not able to reproduce the observed spatial patterns and frequency of occurrence of WRs may be unsuitable for simulating climate variability and its long-term changes (Hannachi et al., 2017). Hence, the assessment of WRs can help improve our understanding of predictability on intra-seasonal to inter-annual time scales. In addition, the use of WRs to evaluate the impact of the atmospheric circulation on essential climate variables and sectoral climatic indices is of great interest to the climate services communities (Grams et al., 2017).

The recipe *recipe_modes_of_variability.yml* takes daily or monthly data from a particular region, season (or month) and period as input, and then applies k-mean clustering or hierarchical clustering either directly to the spatial data or after computing the EOFs. This recipe can be run for both a reference/observational dataset and climate projections simultaneously, and the root-mean-square error is then calculated between the mean anomalies obtained for the clusters from the reference and projection data sets. The user can specify the number of clusters to be computed. The recipe output consist of netCDF files of the time series of the cluster occurrences, the mean anomaly corresponding to each cluster at each location and the corresponding p-value, for both the observed and projected WR and the RMSE between them. The recipe also creates three plots: the observed/reference modes of variability (Figure 15), the reassigned modes of variability for the future projection (Figure 16) and a table displaying the RMSE values between reference and projected modes of variability (Figure 17). The recipe *recipe_miles_regimes.yml* integrates the diagnostics from the Mid-Latitude Evaluation System – MiLES v0.51 tool (Davini, 2018) in order to calculate the four relevant North Atlantic weather regimes. This is done by analysing the 500hPa geopotential height over the North Atlantic (80W-40E 30N-87.5N). Once a 5-day smoothed daily seasonal cycle is removed, the Empirical Orthogonal Functions which explain at least the 80% of the variance are extracted in order to reduce the phase-space dimensions. A k-means clustering using Hartigan-Wong algorithm with k=4 is then applied providing the final weather regimes identification. The recipe compares multiples datasets against a reference one (default is ERA-Interim) producing multiple figures which show the pattern of each regime and its difference against the reference dataset. Weather regimes patterns and timeseries are provided in NetCDF4 Zip format. Considering the limited physical significance of Euro-Atlantic weather regimes in other seasons, only winter is currently supported. An example output is shown in Figure 18.

https://doi.org/10.5194/gmd-2019-291
Preprint. Discussion started: 26 November 2019
© Author(s) 2019. CC BY 4.0 License.

Geoscientific Model Development Discussions

3.2.5.3 Empirical Orthogonal Functions

Empirical Orthogonal Function (EOF) analysis is a powerful method to decompose spatiotemporal data using an orthogonal basis of spatial patterns. In weather sciences, EOFs have been extensively used to identify the most important modes of climate variability and their associated teleconnection patterns: for instance, the North Atlantic Oscillation (NAO, (Ambaum, 2010; Wallace and Gutzler, 1981)) and the Arctic Oscillation (AO, Thompson and Wallace (2000)) are usually defined with EOFs. Biases in the representation of the NAO or the AO have been found to be typical in many CMIP5 models (Davini et al., 2012).

The recipe *recipe_miles_eof.yml* integrates diagnostics from the Mid-Latitude Evaluation System – MiLES v0.51 (Davini, 2018) tool in order to extract the first EOFs over a user-defined domain. Three default patterns are supported, namely the "NAO" (North Atlantic Oscillation, over the 90W-40E 20N-85N box), the "PNA" (Pacific North America pattern, over the 140W-80E, 20N-85N box) and the "AO" (Arctic Oscillation, over the 20N-85N box). The computation is based on Singular-Value Decomposition (SVD) applied to the anomalies of the monthly 500 hPa geopotential height. The recipe compares multiples datasets against a reference one (default is ERA-Interim) producing multiple figures which show the linear regressions of the Principal Component (PC) of each EOF on the monthly 500hPa geopotential and its differences against the reference dataset. PCs, EOF patterns, and percentage of variance explained are provided in NetCDF4 Zip format. By default the first four EOFs are stored and plotted. An example output is shown in Figure 19.

3.2.5.4 Indices from differences between area averages

In addition to indices and modes of variability obtained from EOF and clustering analyses, users may wish to compute their own indices based on area-weighted averages or difference in area-weighted averages. For example, the Niño 3.4 index is defined as the sea surface temperature (SST) anomalies averaged over [170–120°W, 5°N–5°S]. Similarly, the NAO index can be defined as the standardized difference between the weighted area-average mean sea level pressure of the domain bounded by [0–80° W, 30–50° N] and [0–80° W 60–80°N.

The functions for computing indices based on area averages in *recipe_combined_indices.yml* have been adapted to allow users to compute indices for the Niño 3, Niño 3.4, Niño 4, NAO and Southern Oscillation Index (SOI) defined region(s), with the option of selecting different variables (e.g. temperature of the ocean surface (tos, commonly named sea surface temperature) or pressure at sea level (psl, commonly named sea level pressure)) with the option to compute standardized variables, applying running means and select different seasons by selecting the initial and final months (e.g.: defining parameter 'moninf' as 6 (12) and 'monsup' as 8 (2), for the boreal summer (winter) June-July-August (December-January-February)). The output of this recipe is a netCDF file containing a time series of the computed indices and a time series of the evolution of the index for individual models and the multi model mean (see Figure 20).

3.3 Diagnostics for the evaluation of processes in the ocean and cryosphere

3.3.1 Physical ocean

The global ocean is a core component of the Earth system. A significant bias in the physical ocean can impact the performance of the entire model.

Several diagnostics exist in ESMValTool v2 to evaluate the broad behaviour of models of the global ocean. Figures 21 to 26 show several diagnostics of the ability of the CMIP5 models to simulate the global ocean. In these figures, model datasets are selected from the historical simulations (here, ensemble member r1i1p1). All

https://doi.org/10.5194/gmd-2019-291
Preprint. Discussion started: 26 November 2019
© Author(s) 2019. CC BY 4.0 License.

Geoscientific Model Development Discussions

available CF-compliant CMIP5 models are compared, however each figure shown in this section may include a different set of models, as not all CMIP5 models produced all the required datasets in a CF-compliant format. To minimise noise, these figures are shown with a 6 year moving window average.

The volume weighted global average temperature anomaly of the ocean is shown in Figure 21 and displays the change in the mean temperature of the ocean relative to the start of the historical simulation The temperature anomaly is calculated against the years 1850-1900. This figure was produced using the recipe *recipe_ocean_scalar_fields.yml*. The AMOC is an indication of the strength of the Northbound current in the Atlantic Ocean and is shown in Figure 22. It transfers heat from tropical waters to the Northern Atlantic ocean. The AMOC has an observed strength of 17.2 Sv (McCarthy et al., 2015). Previous modelling studies (Cheng et al., 2013; Gregory et al., 2005) have predicted a decline in the strength of the AMOC over the 20th century. The Drake Passage current is a measure of the strength of the Antarctic Circumpolar Current (ACC). This is the strongest current in the global ocean and runs clockwise around Antarctica. The ACC was recently measured through the Drake Passage at 173.3±10.7 Sv (Donohue et al., 2016). A comparison to CMIP5 models is shown in Figure 23. Figures 22 and 23 were produced using the recipe *recipe_ocean_amocs.yml*. The global total flux of CO_2 from the atmosphere into the ocean for several CMIP5 models is shown in Figure 24. This figure shows the absorption of atmospheric carbon by the ocean. At the start of the historic period, most of the models shown here have been spun up, meaning that the air to sea flux of CO_2 should be close to zero. As the CO_2 concentration in the atmosphere increases over the course of the historical simulation, the flux of carbon from the air into the sea also increases. The global total integrated primary production from phytoplankton is shown in Figure 25. Marine phytoplankton is responsible for 56±7 Pg of primary production per year (Buitenhuis et al., 2013), which is of similar magnitude to that of land plants (Field et al., 1998). In all cases, we do not expect to observe a significant change in primary production over the course of the historical period. However, the differences in the magnitude of the total integrated primary production inform us about the level of activity of the marine ecosystem. Figure 24 and 25 were both produced with the recipe *recipe_ocean_scalar_fields.yml*. The combination of these five key time series figures allows a coarse scale evaluation of the ocean circulation and biogeochemistry. The global volume weighted temperature shows the effect of warming ocean, the change in Drake passage and the AMOC show significant global changes in circulation. The integrated primary production shows changes in marine productivity and the air sea flux of CO_2 shows the absorption of anthropogenic atmospheric carbon by the ocean.

In addition, a diagnostic from Chapter 9 of IPCC AR5 for the ocean is added (Flato et al., 2013) which is included in *recipe_flato13ipcc.yml*. Figure 26 shows an analysis of the SST that documents the performance of models compared to one standard observational dataset, namely the SST part of the Hadley Centre Sea Ice and Sea Surface Temperature (HadISST) (Rayner et al., 2003) dataset. The SST plays an important role in climate simulations because it is the main oceanic driver of the atmosphere. As such, a good model performance for SST has long been a hallmark of accurate climate predictions. In this figure we reproduce Figure 9.14 of Flato et al. (2013). It shows both zonal mean and equatorial (meaning averaged over 5 degrees South to 5 degrees North) SST. For the zonal mean it shows (a) the error compared to observations for the individual models, (c) the multi model mean with the standard deviation. For the equatorial average it shows (b) the individual model errors and (d) the multi model mean of the temperatures together with the observational dataset. In this way we can give a good overview of both the error and the absolute temperatures, resolved at the individual model level.

https://doi.org/10.5194/gmd-2019-291
Preprint. Discussion started: 26 November 2019
© Author(s) 2019. CC BY 4.0 License.

3.3.2 Southern ocean

The Southern ocean is central to the global climate and the global carbon cycle, and to the climate's response to increasing levels of atmospheric greenhouse gases, as it ventilates a large fraction of the global ocean volume. Roemmich et al. (2015) concluded that the Southern Ocean was responsible for 67-98% of the total oceanic heat uptake; the oceanic increase in heat accounts for 93% of the radiative imbalance at the top of the atmosphere. Global coupled climate models and Earth system models, however, vary widely in their simulations of the Southern Ocean and its role in and response to anthropogenic forcing. Due to the region's complex water-mass structure and dynamics, Southern Ocean carbon and heat uptake depend on a combination of winds, eddies, mixing, buoyancy fluxes, and topography. Russell et al. (2018) laid out a series of diagnostic, observational-based metrics that highlight biases in critical components of the Southern Hemisphere climate system, especially those related to the uptake of heat and carbon by the ocean. These components include the surface fluxes (including wind and heat and carbon), the frontal structure, the circulation and transport within the ocean, the carbon system (in the ESMs) and the sea ice simulation. Each component is associated with one or more model diagnostics, and with relevant observational data sets that can be used for the model evaluation. Russell et al. (2018) noted that biases in the strength and position of the surface westerlies over the Southern Ocean were indicative of biases in several other variables. The strength, extent, and latitudinal position of the Southern Hemisphere surface westerlies are crucial to the simulation of the circulation, vertical exchange and overturning, and heat and carbon fluxes over the Southern Ocean. The net transfer of wind energy to the ocean depends critically on the strength and latitudinal structure of the winds. Equatorward-shifted winds are less aligned with the latitudes of the Drake Passage and are situated over shallower isopycnal surfaces, making them less effective at both driving the ACC and bringing dense deep water up to the surface.

Figure 27 shows the annually-averaged, zonally-averaged zonal wind stress over the Southern Ocean from a sample of the CMIP5 climate simulations and the equivalent quantity from the Climate Forecast System Reanalysis (Saha et al., 2013). While most model metrics indicate that simulations generally bracket the observed quantity, this metric indicates that ALL of the models have an equatorward bias relative to the observations, an indication of a deeper modelling issue. Although Russell et al. (2018) only included six of the simulations submitted as part of CMIP5, the recipe *recipe_russell18jgr.yml* will recreate all of the metrics of this study for all CMIP5 simulations. Each metric assesses a simulated variable, or a climatically-relevant quantity calculated from one or more simulated variables (e.g. heat content is calculated from the simulated ocean temperature, thetao, while the meridional heat transport depends on both the temperature, thetao, and the meridional velocity, vo) relative to the observations. The recipe focuses on factors affecting the simulated heat and carbon uptake by the Southern Ocean. Figure 28 shows the relationship between the latitudinal width of the surface westerly winds over the Southern Ocean with the net heat uptake south of 30°S – the correlation (-0.8) is significant above the 98% level.

3.3.3 Arctic ocean

The Arctic ocean is one of the areas of the Earth where the effects of climate change are especially visible today. Two most prominent processes are Arctic amplification (Serreze and Barry, 2011) and decrease of the sea ice area and thickness (see Section 3.3.2). Both receive good coverage in the literature and are already well-studied. Much less attention is paid to the interior of the Arctic Ocean itself. In order to increase our confidence in projections of the Arctic climate future proper representation of the Arctic Ocean hydrography is necessary.

https://doi.org/10.5194/gmd-2019-291
Preprint. Discussion started: 26 November 2019
© Author(s) 2019. CC BY 4.0 License.

The vertical structure of temperature and salinity (T and S) in the ocean model is a key diagnostic that is used for ocean model evaluation. Realistic temperature and salinity distributions mean that the models properly represent dynamic and thermodynamic processes in the ocean. Different ocean basins have different hydrological regimes so it is important to perform analysis of vertical TS distribution for different basins separately. The basic diagnostic in this sense is mean vertical profiles of temperature and salinity over some basin averaged for a relatively long period of time. Figure 29 shows the mean (1970-2005) vertical ocean potential temperature distribution in the Eurasian Basin of the Arctic Ocean as produced with *recipe_arctic_ocean.yml*. In addition to individual vertical profiles for every model, we also show the mean over all participating models and similar profile from climatological data (PHC3, Steele et al. (2001)). The characteristics of vertical TS distribution can change with time, and consequently the vertical TS distribution is an important indicator of the behaviour of the coupled ocean-sea ice-atmosphere system in the North Atlantic and Arctic Oceans. One way to evaluate these changes is by using Hovmoller diagrams. We have created Hovmoller diagrams for two main Arctic Ocean basins – Eurasian and Amerasian with T and S spatially averaged on a monthly basis for every vertical level. This diagnostic allows the temporal evolution of vertical ocean potential temperature distribution to be assessed. The T-S diagrams allow the analysis of water masses and their potential for mixing. The lines of constant density for specific ranges of temperature and salinity are shown on the background of the T-S diagram. The dots on the diagram are individual grid points from specified region at all model levels within user specified depth range. The depths are colour coded. Examples of the mean (1970-2005) T-S diagram for Eurasian Basin of the Arctic Ocean shown in Figure 30 refer to *recipe_arctic_ocean.yml*.

The spatial distribution of basic oceanographic variables characterises the properties and spreading of ocean water masses. For the coupled models, capturing the spatial distribution of oceanographic variables is especially important in order to correctly represent the ocean-ice-atmosphere interface. We have implemented plots with spatial maps of temperature, salinity and current speeds at original model levels. For temperature and salinity, we have also implemented spatial maps of model biases from the observed climatology with respect to PHC3 climatology. For the model biases, values from the original model levels are linearly interpolated to the climatology levels and then spatially interpolated from the model grid to the regular PHC3 climatology grid. Resulting fields show model performance in simulating spatial distribution of temperature and salinity. Vertical transects through arbitrary sections are important for analysis of vertical distribution of ocean water properties and especially useful when exchange between different ocean basins is evaluated. Therefore, diagnostics that allow for the definition of an arbitrary ocean section by providing set of points on the ocean surface are also implemented. For each point, a vertical profile on the original model levels is interpolated. All profiles are then connected to form a transect. The great-circle distance between the points is calculated and used as along-track distance. One of the main use cases for transects is to create vertical sections across ocean passages. Transects that follow the pathway of the Atlantic water according to Ilıcak et al. (2016) are also included. Atlantic water is a key water mass of the Arctic Ocean and its proper representation is one of the main challenges in Arctic Ocean modelling. A diagnostic that calculates the temperature of the Atlantic water core for every model as the maximum potential temperature between 200 and 1000-meter depth in the Eurasian Basin is included in this release. The depth of the Atlantic water core is calculated as the model level depth where the maximum temperature is found in Eurasian Basin (Atlantic water core temperature). In order to evaluate the spatial distribution of Atlantic water in different climate models we also provide diagnostics with maps of the spatial distribution of water temperature at the depth of Atlantic water core in *recipe_arctic_ocean.yml*.

https://doi.org/10.5194/gmd-2019-291
Preprint. Discussion started: 26 November 2019
© Author(s) 2019. CC BY 4.0 License.

3.3.4 Sea Ice

Sea ice is a critical component of the climate system, which considerably influences the ocean and atmosphere through different processes and feedbacks (Goosse et al., 2018). In the Arctic, sea ice has been dramatically retreating (Stroeve and Notz, 2018) and thinning (Kwok, 2018) in the past decades. In the Antarctic, there has been a small but significant increase in sea-ice cover from the beginning of satellite observations with large interannual variability, showing for example a sudden sea-ice retreat since late 2015 (Meehl et al., 2019; Schlosser et al., 2018)). Climate models constitute a useful tool to make projections of the future changes in sea ice (Massonnet et al., 2012). However, the different climate models largely disagree on the magnitude of sea-ice changes (Stroeve et al., 2012). One of the reasons for this disagreement is the lack of understanding and representing core thermodynamic and dynamic processes and feedbacks related to sea ice.

In order to better understand and reduce model errors, two recipes related to sea ice have been implemented into ESMValTool v2.0. The first recipe, *recipe_seaice_feedback.yml*, is related to the negative sea-ice growth–thickness feedback (Massonnet et al., 2018). In this recipe, one process-based diagnostic named the Ice Formation Efficiency (IFE) is computed based on monthly mean sea-ice volume estimated north of 80°N. The choice of this domain is motivated by the desire to minimize the influence of dynamic processes but also by the availability of sea-ice thickness measurements. The diagnostic intends to evaluate the strength of the negative sea-ice thickness/growth feedback, which causes late-summer negative anomalies in sea-ice area and volume to be partially recovered during the next growing season (Notz and Bitz, 2017). A chief cause behind the existence of this feedback is the non-linear inverse dependence between heat conduction fluxes and sea-ice thickness, which implies that thin sea ice grows faster than thick sea ice. To estimate the strength of that feedback, anomalies of the annual minimum of sea-ice volume north of 80°N are first estimated. Then, the increase in sea-ice volume until the next annual maximum is computed for each year. The IFE is defined as the regression of this ice volume production onto the baseline summer volume anomaly (Figure 31). The IFE was applied to the CMIP5 ensemble (Massonnet et al., 2018). It was first found that all CMIP5 models, without exception, simulate negative IFE over the historical period, implying that all these models display a basic mechanism of ice volume recovery when large negative anomalies occur in late summer. However, the strength of the IFE was found to be simulated very differently by the models. The IFE was in fact found to be closely associated with the background mean sea-ice state of the models (defined as the annual mean sea-ice volume north of 80°N) with stronger feedback strength ice thins. In parallel, it was found that the strength of the IFE was directly connected to the long-term variability (persistence, year-to-year variability, decadal trends), providing prospects for the application of emergent constraints. However, the shortness of observational records of sea-ice thickness and their large uncertainty precluded rigorous applications of such constraints. The analyses nevertheless allowed (1) to pin down that the spread in CMIP5 ice volume projections is inherently linked to the way they represent the strength of sea ice feedbacks, which itself is closely linked to the model mean states, and (2) to provide guidance for the development of future observing systems in the Arctic, by stressing the need for more reliable estimates of sea ice thickness in the central Arctic basin. The second recipe, *recipe_sea_ice_drift.yml*, allows to quantify the relationships between Arctic sea-ice drift speed, concentration and thickness (Docquier et al., 2017). A decrease in concentration or thickness, as observed in recent decades in the Arctic Ocean (Kwok, 2018; Stroeve and Notz, 2018), leads to reduced sea-ice strength and internal stress, and thus larger sea-ice drift speed (Rampal et al., 2011). This in turn could provide higher export of sea ice out of the Arctic Basin, resulting in lower sea-ice concentration and further thinning. Olason and Notz (2014) investigate the relationships between Arctic sea-ice

https://doi.org/10.5194/gmd-2019-291
Preprint. Discussion started: 26 November 2019
© Author(s) 2019. CC BY 4.0 License.

drift speed, concentration and thickness using satellite and buoy observations. They show that both seasonal and recent long-term changes in sea ice drift are primarily correlated to changes in sea ice concentration and thickness. Our recipe allows to quantify these relationships in climate models. In this recipe, four process-based metrics are computed based on the multi-year monthly mean sea-ice drift speed, concentration and thickness, averaged over the Central Arctic. The first metric is the ratio between the modelled drift-concentration slope and the observed drift-concentration slope. The second metric is similar to the first one, except that sea-ice thickness is involved instead of sea-ice concentration. The third metric is the normalised distance between the model and observations in the drift-concentration space. The fourth metric is similar to the third one, except that sea-ice thickness is involved instead of sea-ice concentration. Sea-ice concentration from the European Organisation for the Exploitation of Meteorological Satellites Ocean and Sea Ice Satellite Application Facility (Lavergne et al., 2019)), sea-ice thickness from the Pan-Arctic Ice-Ocean Modeling and Assimilation System reanalysis (PIOMAS, Zhang and Rothrock (2003)) and sea-ice drift from the International Arctic Buoy Programme (IABP, Tschudi et al. (2016)) are used as reference products to compute these metrics (Figure 32).

3.4 Diagnostics for the evaluation of land processes

3.4.1 Land Cover

Land cover (LC) is either prescribed in the CMIP models or simulated using a Dynamic Global Vegetation Model (DGVM). Within the recent decade, numerous studies focused on the quantification of the impact of land cover change on climate (see Mahmood et al. (2014) and references therein for a comprehensive review). There is a growing body of evidence that vegetation, especially tree cover, significantly affects the terrestrial water cycle, energy balance (Alkama and Cescatti, 2016; Duveiller et al., 2018b) and carbon cycle (Achard et al., 2014). However, understanding the impact of LC change on climate remains controversial and is still work in progress (Bonan, 2008; Ellison et al., 2012; Mahmood et al., 2014; Sheil and Murdiyarso, 2009). In order to judge the LC related ESM results, an independent assessment of the accuracy of the simulated spatial distributions of major land cover types is desirable to evaluate the DGVM accuracy for present climate conditions (Lauer et al., 2017).

Recently in the frame of the European Space Agency (ESA) Climate Change Initiative (CCI), a new global LC dataset has been published (Defourny et al., 2014; Defourny et al., 2016) that can be used to evaluate or prescribe vegetation distributions for climate modelling. Effects of LC uncertainty in the ESA CCI LC dataset on land surface fluxes and climate are described by Hartley et al. (2017) and Georgievski and Hagemann (2018), respectively. Satellite derived LC classes cannot directly be used for the evaluation of ESM vegetation due to the different concepts of vegetation representation in DGVMs, which are typically based on the concept of plant functional types (PFTs) that are supposed to represent groups of LC with similar functional behaviour. Thus, an important first step is to map the ESA CCI LC classes to PFTs as described by Poulter et al. (2015). As the PFTs in ESMs differ, the current LC diagnostic analyses only major LC types (bare soil, crops, grass, shrubs, trees), which is similar to the approach chosen by Brovkin et al. (2013) and Lauer et al. (2017). The corresponding evaluation metric was implemented into the ESMValTool in *recipe_landcover.yml*. It evaluates areas, mean fractions and biases compared to ESA CCI LC data over four major regions (global land area, tropics (30°S-30°N), northern extratropical land areas north of 30°N), and southern extratropical land areas south of 30°S). Currently the evaluation is using ESA CCI LC data for the epoch 2008-2012 that have been generated with the ESA CCI LC user tool at 0.5 degree resolution. Consequently, model data are interpolated to the same

https://doi.org/10.5194/gmd-2019-291
Preprint. Discussion started: 26 November 2019
© Author(s) 2019. CC BY 4.0 License.

Geoscientific Model Development Discussions

resolution. For the calculation of mean fractions per major region, a land area of these regions needs to be specified, which is currently taken from ESA CCI land cover. Example plots of accumulated area and biases in major LC types for different models are shown in Figure 33.

690 **3.4.2 Albedo changes associated to land cover transitions**

Land Cover Changes (LCC) can modify climate by altering land surface properties such as surface albedo, surface roughness and evaporative fraction. In particular, historical deforestation is believed to have led to an increase in surface albedo corresponding to a global radiative forcing of -0.15 +/- 0.10 Wm^{-2} (Change, 2013). There are however large uncertainties, even concerning the sign of the effect, regarding the impacts of LUC on
695 near-surface temperature due to persistent model disagreement (Davin et al., 2019; de Noblet-Ducoudré et al., 2012; Lejeune et al., 2017; Pitman et al., 2009). These disagreements arise from uncertainties in 1) the interplay between radiative (albedo) and non-radiative processes (surface roughness and evaporative fraction), 2) the role of local versus large scale processes and feedbacks (Winckler et al., 2017) and 3) in the magnitude of change in given surface properties (e.g. albedo). Concerning the latter, Myhre et al. (2005) and Kvalevåg et al. (2010)
700 suggest that the albedo change between natural vegetation and croplands is usually overestimated in climate simulations compared to satellite-derived observational evidence. In addition to this potential bias compared to observational data, there is a substantial spread in the models' parameterized albedo response to land-cover perturbations. Boisier et al. (2012) identified that this is responsible for half of the dispersion in the albedo response to LCC since preindustrial times among models participating in the LUCID project, the remaining
705 uncertainty resulting from differences in the imposed Land Cover. A more systematic evaluation of model performance in simulating LUC-induced changes in albedo based on latest available observations is therefore essential in order to reduce these uncertainties.

A satellite-based dataset providing potential effect of a range of land cover transitions on the full surface energy balance (including albedo), at global scale, 1°-resolution, and monthly timescale was recently made available
710 (Duveiller et al., 2018b). The potential albedo changes associated to vegetation transitions were extracted by a statistical treatment combining the recent ESA CCI LC data (see 3.4.1 for references) and the mean of the white-sky and black-sky albedo values of the NASA MCD43C3 albedo product for the 2008-2012 period (see (Schaaf et al., 2002) for information on the retrieval algorithm). Because land cover-specific albedo values are not a standard output of climate models, in order to retrieve them a diagnostic was implemented into the ESMValTool
715 in *recipe_albedolandcover.yml*. It follows a similar approach but applied on model outputs, i.e. determines the coefficients of multiple linear regressions fitted between the albedo values and the tree, shrub, short vegetation (crops and grasses) and bare soil fractions of each grid cell within spatially moving windows encompassing 5x5 model grid cells. Solving these regressions provides the albedo values for trees, shrubs and short vegetation (crops and grasses) from which the albedo changes associated with transitions between these three LC types are
720 derived. The diagnostic is applied on monthly data, and based on the value of the snow area fraction (snc) distinguishes between snow-free (snc<0.1) and snow-covered (snc>0.9) grid cells for each month. It can calculate albedo estimates for each of these two cases and each of the three land cover types. It eventually plots global maps of the albedo changes associated with the corresponding LC transitions for each model in their original resolution, next to the satellite-derived estimates from Duveiller et al. (2018a). Two versions of this
725 observational dataset, corresponding to two vegetation classifications, are both freely available. The diagnostic shows data according to the IGBPgen classification, which entails only four LC classes that can be directly

https://doi.org/10.5194/gmd-2019-291
Preprint. Discussion started: 26 November 2019
© Author(s) 2019. CC BY 4.0 License.

compared to model PFTs. An example plot is shown in Figure 34 for the July albedo change associated with a transition from trees to short vegetation types (crops and grasses). Almost only snow-free areas are visible for this month, while grey areas indicate where the spatial coexistence of the two LC classes was not high enough for the regression technique to be performed, where the regression results did not pass the required quality checks, or grid cells which could not be categorised either as snow-free or as snow-covered (Duveiller et al., 2018a).

3.5 Diagnostics for the evaluation of biogeochemical processes

3.5.1 Terrestrial biogeochemistry

With CO_2 being the most important anthropogenic greenhouse gas, it is vital for ESMs to have a realistic representation of the carbon cycle. Atmospheric concentration of CO_2 can be inferred from the difference between anthropogenic emissions and the land and ocean carbon sinks simulated by the models. These sinks are affected by atmospheric CO_2 and climate change, thus introducing feedbacks between the climate system and the carbon cycle (Arora et al., 2013; Friedlingstein et al., 2006). Quantification of these feedbacks to estimate the evolution of these carbon sinks and thus the atmospheric CO_2 concentration and the resulting climate change is paramount (Cox et al., 2013; Friedlingstein et al., 2014; Wenzel et al., 2014; Wenzel et al., 2016). The Anav et al. (2013) paper evaluated CMIP5 models in three different time scales: long-term trends, interannual variability and seasonal cycles for the main climatic variables controlling both the spatial and temporal characteristics of the carbon cycle, i.e. surface land temperature (tas), precipitation over land (pr), sea surface temperature (tos), land-atmosphere (nbp) and ocean-atmosphere fluxes ($fgco_2$), gross primary production (gpp), leaf area index (lai), and carbon content in soil and vegetation (csoil, cveg). Models are able to simulate key characteristics of the main climatic variables and their seasonal evolution, but deficiencies in the simulation of specific variables, especially in the land carbon cycle with a general overestimation of photosynthesis and leaf area index, as well as an underestimation of the primary production in the ocean, exist.

The analysis from the Anav et al. (2013) can be reproduced with *recipe_anav13jclim.yml*. Alongside porting the existing recipe to v2, plots for the timeseries anomalies of tas, pr, SST, as well as timeseries for nbp and $fgco_2$ have been added, reproducing Figures 1, 2, 3, 5, and 13 of Anav et al. (2013), with the latter two also forming Figure 26 of Flato et al. (2013). In ESMValTool v2, observational estimates of gpp are included from the latest data release of the FLUXCOM project (Jung et al., 2019) which integrates FLUXNET measurements, satellite remote sensing and climate data with machine learning to provide improved global products of land-atmosphere fluxes for evaluation. The routines needed to make carbon and energy fluxes from the FLUXCOM project CMOR-compliant to facilitate process based model evaluation is also made available as part of ESMValTool v2. As an example of the newly added plots, Figure 35 shows the timeseries for the land-atmosphere carbon flux nbp, similar to Figure 5 of Anav et al. (2013). Shading indicates the confidence interval of the CMIP5 ensemble standard deviation, derived from assuming a t-distribution centered on the ensemble mean (inner curve), while the gray shading shows the overall range of variability of the models.

3.5.2 Ecosystem Turnover Times of Carbon

The exchange of carbon between the land biosphere and atmosphere represents a key feedback mechanism that will determine the effect of global changes on the carbon cycle and vice-versa (Heimann and Reichstein, 2008). Despite significant implications, the uncertainties in simulated land carbon stocks that integrates the land-

https://doi.org/10.5194/gmd-2019-291
Preprint. Discussion started: 26 November 2019
© Author(s) 2019. CC BY 4.0 License.

atmosphere carbon exchange are large, and, therefore, represent a major challenge for ESMs (Friedlingstein et al., 2014; Friend et al., 2014). One of the major factors leading to these uncertainties is the turnover time of carbon, the time period that a carbon atom on average spends in land ecosystems, from assimilation through photosynthesis to its release back into the atmosphere. This emergent ecosystem property, calculated, for example, as a ratio of long-term average total carbon stock to gross primary productivity, is not well-reproduced by most of the ESMs (Carvalhais et al., 2014; Koven et al., 2015).

Carvalhais et al. (2014) evaluated the biases in ecosystem carbon turnover time in CMIP5 models, their associations with climate variables, and then quantified multimodel biases and agreements. The *recipe_carvalhais2014nat.yml* reproduces the analysis of Carvalhais et al. (2014). It requires the simulations of total ecosystem carbon stock (or its components), gross primary productivity, as well as precipitation and temperature. As an example, an evaluation of the zonal means of turnover time in CMIP5 models is shown in Figure 36. Most CMIP5 models (and multi-model ensemble) have a much shorter turnover time than the observation-based estimate across the whole latitudinal range. The spread among the models is also large and can vary by an order of magnitude. This results in not only a large bias in turnover time, but also a considerable disagreement among the models. In fact, the majority of CMIP5 models simulate turnover time more than four times shorter than the observation-based estimate in most regions globally (Figure 37). In arid and semi-arid regions model agreement is also low with 2 or fewer (out of 10) models within the observational uncertainty. In addition, the recipe also produces the full factorial model-model-observation comparison matrix that can be used to evaluate individual models. It further provides a quantitative measure of turnover times across different biomes, as well as its relationship with precipitation and temperature.

3.5.3 Marine biogeochemistry

ESMValTool v2 now includes a wide set of metrics to assess marine biogeochemistry performances of ESMs, contained in *recipe_ocean_bgc.yml*. This recipe allows a direct comparison of the models against observational data for temperature (thetao), salinity (so), oxygen (o2), nitrate (no3), phosphate (po4) and silicate (si) from World Ocean Atlas 2013 (WOA, Garcia et al. (2013)), CO_2 air-sea fluxes ($fgco_2$) estimated by Landschuetzer et al. (2016), Chlorophyll-a (chl) fields from ESACCI-OC (Volpe et al., 2019) and primary production expressed as carbon (intpp) produced by Oregon State University using MODIS data (Behrenfeld et al., 1997).

We first demonstrate the recipe using the nitrate concentration in the CMIP5 HadGEM2-ES model in the r1i1p1 ensemble member of the historical experiment in the years 2001-2005. However, this recipe can be expanded to include any other CMOR-ised ESM with a marine biogeochemical component, or any other field with a suitable observational dataset. The analysis produced by the recipe is a point to point comparison of the model against the observational dataset, similar to the method described in (De Mora et al., 2013). Figures 38 and 39 show the results of a comparison the surface dissolved nitrate concentration in the CMIP5 HadGEM2-ES model compared against the World Ocean Atlas nitrate. To produce these two figures, the surface layer is extracted, an average over the time dimension is produced, then the model are observational data are re-gridded to a common grid. Figure 38 includes four panels; the model and observations in the top two panes, then the difference and the quotient in the lower two panes. Figure 39 uses the same preprocessed data as Figure 38, with the model data plotted along the x axis and the observational data along the y-axis. A linear regression line of best fit is shown as a black line. A dashed line indicates the 1:1 line. The results of a linear regression are shown in the top left corner of the figure, where $\widehat{\beta}_0$ is the intercept, β_1 is the slope, R is the correlation, P is the P value, and N is the

https://doi.org/10.5194/gmd-2019-291
Preprint. Discussion started: 26 November 2019
© Author(s) 2019. CC BY 4.0 License.

number of data point pairs. Together, Figures 38 and 39 show a clear indication of the presence of biases in the surface layer, but also the spatial distribution of the model and observational data. Figure 40 shows the global average depth profile of the dissolved nitrate concentration in the CMIP5 HadGEM2-ES model and against the World Ocean Atlas dataset. The colour scale indicates the annual average, although in this specific case there is little observed inter-annual variability. This class of figure is useful to evaluate biases between model and observations over the entire depth profile of the ocean. A multiple panel comparison of satellite derived observations for marine primary production against 16 CMIP5 models over the period 1995-2004 is shown in Figure 41. By means of ESMValTool preprocessor, both observation and models data are redefined over a regular 1-degree horizontal grid and differences are then computed.

3.5.4 Stratospheric temperature and trace species influencing stratospheric ozone chemistry

The *recipe_eyring06jgr.yml* is integrated in v2.0 from the CCMVal-Diag tool described by Gettelman et al. (2012) to evaluate coupled chemistry-climate model (CCM) based on a set of core processes relevant for stratospheric ozone concentrations, centered around four main categories (radiation, dynamics, transport, and stratospheric chemistry). Each process is associated with one or more model diagnostics, and with relevant observational data sets that can be used for the model evaluation (Eyring et al., 2006; Eyring et al., 2005).
Since most of the chemical reactions determining ozone distribution in the stratosphere depend on temperature, *recipe_eyring06jgr.yml* allows the comparison of modelled stratospheric temperature with observations in terms of climatological mean, variability and trends (Figure 42). *Recipe_eyring06jgr.yml* evaluates the main features of the atmospheric transport by examining the distribution of long-lived traces (such as methane or N_2O), the vertical propagation of the annual cycle of water vapour ("tape recorder") and the mean age of air. Due to its important role in driving stratospheric ozone depletion, especially in the polar regions, the recipe also includes the vertical distribution and temporal evolution of modelled chlorine (Cl_y). It also assesses the capability of the models to simulate realistic ozone vertical distributions (Figure 43) and total ozone annual cycle.

4. Routine evaluation of CMIP6 models

4.1 Running the ESMValTool alongside the ESGF

The semi-automatic and automatic execution of the ESMValTool at DKRZ on CMIP6 data published in ESGF is supported by the following components: A) a locally hosted CMIP6 replica data pool, B) an automatic CMIP6 data replication process, embracing ESMValTool data needs as replication priorities, C) a query mechanism to inform the ESMValTool on the availability on new data in the data pool. Based on these components both regularly scheduled ESMValTool executions as well as executions triggered by the availability of new data can be realised. Initially the automatic regular execution was implemented. The replica pool is hosted as part of the parallel Lustre HPC file system at DKRZ and associated to a dedicated data project which is supervised by a panel deciding on CMIP6 data storage priorities.
ESMValTool data needs are managed in a GitHub repository and automatically integrated into the synda tool based CMIP6 replication pipeline at DKRZ. The content of the data pool is regularly indexed thus providing a high performance query mechanism on locally available data. This index is used to automatically update several recipes with all available CMIP6 models. If new model output has been published to the ESGF, an ESMValTool

https://doi.org/10.5194/gmd-2019-291
Preprint. Discussion started: 26 November 2019
© Author(s) 2019. CC BY 4.0 License.

Geoscientific Model Development Discussions

execution is triggered and new plots are created. The results produced by the ESMValTool runs are automatically copied to the result cache which is used by the result browser (see next section).

4.2 ESMValTool result browser at DKRZ

A result browser has been set up at http://cmip-esmvaltool.dkrz.de/. The ESMValTool results are visualized with the Freie University evaluation system (FREVA). Freva provides efficient and comprehensive access to the evaluation results and datasets. The application system is developed as an easy to use low-end application minimizing technical requirements for users and tool developers. Initially this website shows CMIP5 results that are already published. Newly produced results for CMIP6 are initially water-marked and are only made available without water-mark once quality control has happened and possible papers have been written. This strategy has been supported, encouraged, and approved by the WCRP Working Group of Coupled Modelling (WGCM). The result browser includes a search function that allows to sort by (a) ESMValTool recipes, (b) Projects, (c) CMIP6 Realms, (d) Themes, (e) Domain, (f) Plot Type, (g) Statistics, (h) References, (i) Variables, (j) Models (including the multi-model mean and observations), and (k) Results. Each figure includes a figure caption that is displayed alongside with the figure, and also includes metadata. These metadata include the ESMValTool configuration used to calculate and plot the figure, Software versions, Date of production, Input data, Program's output, Notes, and Results.

5. Summary and Outlook

The Earth System Model Evaluation Tool (ESMValTool) is a community diagnostics and performance metrics tool specifically targeted to facilitate and enhance comprehensive evaluation of Earth System Models (ESMs) participating in the Coupled Model Intercomparison Project (CMIP). Since the first ESMValTool release in 2016 (v1.0, Eyring et al. (2016c)), substantial technical improvements have been made by a continuously growing developer community and additional diagnostics have been added. The tool is now developed by more than 40 institutions as open source code on a Github repository (https://github.com/ESMValGroup).

This paper is part of a series of publications that describe the release of ESMValTool version 2.0 (v2.0). One of the main structural changes compared to v1.0 is the separation of the tool into *ESMValCore* and a *Diagnostic Part*. *ESMValCore* is an easy-to-install, well documented Python package that provides the core functionalities to perform common pre-processing operations and writes the output from models and observations to netCDF files (Righi et al., 2019). These preprocessed output files are then read by the *Diagnostic Part* that includes tailored diagnostics and performance metrics for specific scientific applications that are called by *recipes*. These recipes reproduce sets of diagnostics or performance metrics that have demonstrated their importance in ESM evaluation in the peer-reviewed literature.

This paper describes recipes for the evaluation of large-scale diagnostics in ESMValTool v2.0. It focuses on those diagnostics that were not part of the first major release of the tool (Eyring et al., 2016c) and includes (1) integrative measures of model performance, as well as diagnostics for the evaluation of processes in (2) the atmosphere, (3) ocean and cryosphere, (4) land and (5) biogeochemistry. Recipes for extreme events and in support of regional model evaluation are described by Weigel et al. (2019) and recipes for emergent constraints and model weighting by Lauer et al. (2019).

https://doi.org/10.5194/gmd-2019-291
Preprint. Discussion started: 26 November 2019
© Author(s) 2019. CC BY 4.0 License.

Compared to v2.0, the integrative measures of model performance have been expanded with additional atmospheric variables as well as new variables from the ocean, sea-ice and land (extending Figure 9.7 of Flato et al. (2013)). In addition, the centered pattern correlation that allows the quantification of progress between different ensembles of CMIP models for multiple variables (extending Figure 9.6 of Flato et al. (2013)) and the single model performance index proposed by Reichler and Kim (2008) that allows an overall assessment of model performance have been added. For the purpose of model development it is important to look at many different metrics. AutoAssess that is developed by the UK Met Office therefore includes a mix of top-down metrics evaluating key model output variables and bottom-up process-oriented metrics. AutoAssess includes 11 thematic areas which will all be implemented in ESMValTool, but for v2.0 as a technical demonstration only the area for the stratosphere was implemented.

For the evaluation of processes in the atmosphere, the recipe to calculate multi-model averages (e.g., for surface temperature and precipitation) now not only includes absolute values but also the mean root mean square error of the seasonal cycle compared to observations. The time series of the anomalies in annual and global mean surface temperature with the models being subsampled as in the observations from HadCRUT4 is also included. In addition, a recipe for the evaluation of the precipitation quantile bias has been added. For atmospheric dynamics recipes to evaluate stratosphere-troposphere coupling and atmospheric blocking indices have been included. A new diagnostic tool for the evaluation of the water, energy and entropy budgets in climate models (TheDiaTo (v1.0), Lembo et al. (2019)) has been newly implemented and v2.0 was updated with a new version of the NCAR Climate Variability Diagnostic Package (Phillips et al., 2014). In addition, several other diagnostics to evaluate modes of variability as well as weather regimes calculated by the MiLES package (Davini, 2018) have been added in v2.0.

To evaluate the broad behaviour of models for the global ocean, several diagnostics have been newly implemented, including diagnostics to evaluate the volume weighted global average temperature anomaly, the AMOC, the Drake Passage current, the global total flux of CO_2 from the atmosphere into the ocean, and the global total integrated primary production from phytoplankton. A recipe to evaluate specifically the Southern ocean following Russell et al. (2018) has been included and for the Arctic ocean vertical ocean distributions (e.g. temperature and salinity) for different Artic ocean basins and a transect that follows the pathway of the Atlantic water can now be calculated. For sea-ice, a recipe related to the evaluation of the negative sea-ice growth–thickness feedback which includes the Ice Formation Efficiency (IFE) aa a process-based diagnostic (Massonnet et al., 2018) and a recipe that can quantify the relationships between Arctic sea-ice drift speed, concentration and thickness (Docquier et al., 2017) have been added.

For the evaluation of land processes, satellite derived land cover classes cannot directly be used for ESM vegetation evaluation because Dynamic Global Vegetation Models (DGVMs) use different concepts for vegetation representation, typically based on plant functional types (PFTs). A recipe has therefore been added that maps the ESA CCI land cover classes to PFTs as described by Poulter et al. (2015). It includes major land cover types (bare soil, crops, grass, shrubs, trees) similar to the evaluation study by Lauer et al. (2017). In addition, a recipe has been added that can be used to evaluate albedo changes associated to land cover transitions using the ESA CCI dataset of Duveiller et al. (2018b).

For the terrestrial biosphere, a recipe that allows the evaluation of the main climatic variables controlling both the spatial and temporal characteristics of the carbon cycle on three different time scales (long-term trends, interannual variability and seasonal cycles) has been added following Anav et al. (2013). These key variables

https://doi.org/10.5194/gmd-2019-291
Preprint. Discussion started: 26 November 2019
© Author(s) 2019. CC BY 4.0 License.

include surface land temperature, precipitation over land, sea surface temperatures, land-atmosphere and ocean-atmosphere fluxes, gross primary production, leaf area index, and carbon content in soil and vegetation. To evaluate the simulated land carbon stocks that integrates the land-atmosphere carbon exchange, a recipe to evaluate biases in ecosystem carbon turnover time, the time period that a carbon atom on average spends in land ecosystems, from assimilation through photosynthesis to its release back into the atmosphere (Carvalhais et al., 2014) has been added. For marine biogeochemistry, v2.0 now includes a recipe that allows a direct comparison of the models against observational data for several variables including temperature, salinity, oxygen, nitrate, phosphate, silicate, CO_2 air-sea fluxes, chlorophyll-a and primary production. The point to point comparison of the model against the observational dataset is similar to De Mora et al. (2013). To evaluate stratospheric dynamics and chemistry a recipe based on a set of core processes relevant for stratospheric ozone concentrations, centered around four main categories (radiation, dynamics, transport, and stratospheric chemistry) has been added (Eyring et al., 2006). Overall these recipes together with those already included in v1.0 allow a broad characterization of the models for key variables (such as temperature and precipitation) on the large-scale, but v2.0 also includes several process-oriented diagnostics.

With this release, for the first time in CMIP it is now possible to evaluate the models as soon as the output is published to the Earth System Grid Federation (ESGF) in a quasi-operational manner. To achieve this, the ESMValTool has been fully integrated into the ESGF structure at the Deutsches Klima Rechenzentrum (DKRZ). The data from the ESGF are first copied to a local replica and the ESMValTool is then automatically executed alongside the ESGF as soon as new output arrives. An ESMValTool result browser has been set up that makes the evaluation results available to the wider community (http://cmip-esmvaltool.dkrz.de/).

Another major advancement of ESMValTool v2.0 is that it provides full provenance and traceability (see Section 5.2. in Righi et al. (2019) for details). Provenance information for example includes technical information such as global attributes of all input netCDF files, preprocessor settings, diagnostic script settings, and software version numbers but also diagnostic script name and recipe authors, funding projects, references for citation purposes, as well as tags for categorizing the result plots into various scientific topics (like chemistry, dynamics, sea-ice, etc.) realms (land, atmosphere, ocean, etc.) or statistics applied (RMSE, anomaly, trend, climatology, etc.). This not only facilitates the sorting of the results in the ESMValTool result browser but also qualifies the tool for the use in studies or assessments where provenance and traceability is particularly important. The current approach to provenance and tags (i.e. what is reported) can be adjusted to international provenance standards as they become available.

These recent ESMValTool developments and their coupling to the ESGF results can now be exploited by global and regional ESM developers as well as by the data analysis and user communities, to better understand the large CMIP ensemble and to support data exploitation. In particular with the addition of provenance, the tool can also provide a valuable source to produce figures in national and international assessment reports (such as the IPCC climate assessments) to enhance the quality control, reproducibility and traceability of the figures included.

The ESMValTool development community will further enhance the capabilities of the tool. Targeted technical enhancements will for example include the development of quicklook capabilities that allow to monitor the simulations while they are running to help identifying errors in the simulations early on, a further extension to the application to regional models so that a consistent evaluation between global

https://doi.org/10.5194/gmd-2019-291
Preprint. Discussion started: 26 November 2019
© Author(s) 2019. CC BY 4.0 License.

and regional models can be provided, and distributed computing functionalities. In addition, the tool will be expanded with additional diagnostics in various projects to further enhance comprehensive evaluation and analysis of the CMIP models.

6. Code availability

ESMValTool v2.0 is released under the Apache License, VERSION 2.0. The latest release of ESMValTool v2.0 is publicly available on Zenodo at https://doi.org/10.5281/zenodo.3401363. The source code of the ESMValCore package, which is installed as a dependency of the ESMValTool v2.0, is also publicly available on Zenodo at https://doi.org/10.5281/zenodo.3387139. ESMValTool and ESMValCore are developed on the GitHub repositories available at https://github.com/ESMValGroup.

7. Data availability

CMIP5 data are available freely and publicly from the Earth System Grid Federation. Observations used in the evaluation are detailed in the various sections of the manuscript. They are not distributed with the ESMValTool, that is restricted to the code as open source software.

Author contribution. VE coordinated the ESMValTool v2.0 diagnostic effort and led the writing of the paper. LB, AL, MR, and MS coordinated the diagnostic implementation in ESMValTool v2.0. CE and SK helped with the coupling of ESMValTool v2.0 and CK with the visualization of the results at the ESMValTool result browser. All other co-authors contributed individual diagnostics to this release. All authors contributed to the text.

Competing interests. The authors declare that they have no conflict of interest

Acknowledgements. We dedicate this paper to our great friend and colleague, Alexander Loew, who lost his life in a tragic traffic accident. Our thoughts are with his family and his department. The diagnostic development of ESMValTool v2.0 for this paper was supported by different projects with different scientific focus, in particular by (1) European Union's Horizon 2020 Framework Programme for Research and Innovation "Coordinated Research in Earth Systems and Climate: Experiments, kNowledge, Dissemination and Outreach (CRESCENDO)" project under Grant Agreement No. 641816, (2) Copernicus Climate Change Service (C3S) "Metrics and Access to Global Indices for Climate Projections (C3S-MAGIC)" project, (3) European Union's Horizon 2020 Framework Programme for Research and Innovation "Advanced Prediction in Polar regions and beyond: Modelling, observing system design and LInkages associated with a Changing Arctic climate (APPLICATE)" project under Grant Agreement No. 727862, (4) European Union's Horizon 2020 Framework Programme for Research and Innovation "PRocess-based climate sIMulation: AdVances in high-resolution modelling and European climate Risk Assessment (PRIMAVERA)" project under Grant Agreement No. 641727, (5) Federal Ministry of Education and Research (BMBF) CMIP6-DICAD project, (6) ESA Climate Change Initiative Climate Model User Group (ESA CCI CMUG), (7) Helmholtz Society project "Advanced Earth System Model Evaluation for CMIP (EVal4CMIP)" and (8) project S1 (Diagnosis and Metrics in Climate

https://doi.org/10.5194/gmd-2019-291
Preprint. Discussion started: 26 November 2019
© Author(s) 2019. CC BY 4.0 License.

Models) of the Collaborative Research Centre TRR 181 "Energy Transfer in Atmosphere and Ocean" funded by the Deutsche Forschungsgemeinschaft (DFG, German Research Foundation) Project No 274762653. In addition, we received technical support on the ESMValTool v2.0 development from the European Union's Horizon 2020 Framework Programme for Research and Innovation "Infrastructure for the European Network for Earth System Modelling (IS-ENES3)" project under Grant Agreement No 824084. We acknowledge the World Climate Research Program's (WCRP's) Working Group on Coupled Modelling (WGCM), which is responsible for CMIP, and we thank the climate modelling groups for producing and making available their model output. We thank Mariano Mertens (DLR) for his helpful comments on a previous version and Michaela Langer (DLR) for her help with editing the manuscript. The computational resources of the Deutsches Klima RechenZentrum (DKRZ, Hamburg) were essential for developing and testing this new version and are kindly acknowledged.

https://doi.org/10.5194/gmd-2019-291
Preprint. Discussion started: 26 November 2019
© Author(s) 2019. CC BY 4.0 License.

Geoscientific Model Development Discussions

Tables

Table 1. Overview of standard recipes implemented in ESMValTool v2.0 along with the section they are described, a brief description, the variables used and the diagnostic scripts included. For further details we refer to the GitHub repository.

Recipe name	Chapter	Description	Variables	Diagnostic scripts
Section 3.1: Integrative Measures of Model Performance				
recipe_perfmetrics_CMIP5.yml	3.1.2.1	Recipe for plotting the performance metrics for the CMIP5 datasets, including the standard ECVs as in Flato et al. (2013), and some additional variables (e.g., ozone, sea-ice, aerosol)	ta ua va zg hus tas ts pr clt rlut rsut lwcre swcre od550aer od870aer abs550aer od550lt1aer toz sm	perfmetrics/main.ncl perfmetrics/collect.ncl
recipe_smpi.yml	3.1.2.3	Recipe for computing Single Model Performance Index. Follows Reichler and Kim (2008)	ta va ua hus tas psl pr tos sic hfds tauu tauv	perfmetrics/main.ncl perfmetrics/collect.ncl

https://doi.org/10.5194/gmd-2019-291
Preprint. Discussion started: 26 November 2019
© Author(s) 2019. CC BY 4.0 License.

Geoscientific Model Development Discussions

recipe_autoassess_*.yml	3.1.2.4	Recipe for mix of top-down metrics evaluating key model output variables and bottom-up metrics	tas tsl snw mrsos rsns rlns rtnt rsnt swcre lwcre rsns rlns rsut rlut rsutcs rldscs rlutcs prw pr cllmtisccp clltkisccp clmmtisccp clmtkisccp clhmtisccp clhtkisccp ta ua hus	autoassess/autoassess_area_base.py autoassess/plot_autoassess_metrics.py autoassess/autoassess_radiation_rms.py
Section 3.2: Detection of systematic biases in the physical climate: atmosphere				
recipe_flato13ipcc.yml	3.1.2 3.2.1 3.3.1	Reproducing selected figures from IPCC AR5, chap. 9 (Flato et al., 2013) 9.2, 9.4, 9.5, 9.6, 9.8, 9.14.	tas pr swcre lwcre netcre rlut tos	clouds/clouds_bias.ncl clouds/clouds_ipcc.ncl ipcc_ar5/tsline.ncl ipcc_ar5/ch09_fig09_06.ncl ipcc_ar5/ch09_fig09_06_collect.ncl ipcc_ar5/ch09_fig09_14.py
recipe_quantilebias.yml	3.2.2	Recipe for calculation of precipitation quantile bias	pr	quantilebias/quantilebias.R
recipe_zmnam.yml	3.2.3.1	Recipe for zonal mean Northern Annular Mode. The diagnostics compute the index and the spatial pattern to assess the simulation of the strat-trop coupling in the boreal hemisphere	zg	zmnam/zmnam.py
recipe_miles_block.yml	3.2.3.2	Recipe for computing 1-d and 2-d atmospheric blocking indices and diagnostic	zg	miles/miles_block.R

https://doi.org/10.5194/gmd-2019-291
Preprint. Discussion started: 26 November 2019
© Author(s) 2019. CC BY 4.0 License.

Geoscientific Model Development Discussions
Open Access
EGU

recipe_thermodyn_diagtool.yml	3.2.4	Recipe for the computation of various aspects associated with the thermodynamics of the climate system, such as energy and water mass budgets, meridional enthalpy transports, the Lorenz Energy Cycle and the material entropy production.	hfls hfss pr ps prsn rlds rlus rlut rsds rsus rsdt rsut ts hus tas uas vas ta ua va wap	thermodyn_diagtool/thermodyn_diagnostics.py
recipe_CVDP.yml	3.2.5.1	Recipe for executing the NCAR CVDP pakage in the ESMValTool framework.	ts tas pr psl	cvdp/cvdp_wrapper.py
recipe_modes_of_variability.yml	3.2.5.2	Recipe to compute the RMSE between the observed and modelled patterns of variability obtained through classification and their relative bias (percentage) in the frequency of occurrence and the persistence of each mode.	zg	magic_bsc/weather_regime.r
recipe_miles_regimes.yml	3.2.5.2	Recipe for computing Euro-Atlantic weather regimes using the MiLES package based on k-means clustering	zg	miles/miles_regimes.R
recipe_miles_eof.yml	3.2.5.3	Recipe for computing and the Northern Hemisphere EOFs	zg	miles/miles_eof.R

https://doi.org/10.5194/gmd-2019-291
Preprint. Discussion started: 26 November 2019
© Author(s) 2019. CC BY 4.0 License.

Geoscientific Model Development Discussions

recipe_combined_indices.yml	3.2.5.4	Recipe for computing seasonal means or running averages, combining indices from multiple models and computing area averages	psl	magic_bsc/combined_indices.r
Section 3.3: Detection of systematic biases in the physical climate: ocean and cryosphere				
recipe_ocean_scalar_fields.yml	3.3.1	Recipe to reproduce time series figures of scalar quantities in the ocean.	gtintpp gtfgco2 amoc mfo thetaoga soga zostoga	ocean/diagnostic_timeseries.py
recipe_ocean_amoc.yml	3.3.1	Recipe to reproduce time series figures of the AMOC, the Drake passage current and the stream function	amoc mfo msftmyz	ocean/diagnostic_timeseries.py ocean/diagnostic_transects.py
recipe_russell18jgr.yml	3.3.2	Recipe to reproduce figure from Russell et al. (2018)	tauu tauuo thetao uo sic so vo fgco2 ph	russell18jgr/russell18jgr-polar.ncl russell18jgr/russell18jgr-fig*.ncl
recipe_arctic_ocean.yml	3.3.3	Recipe for evaluation of ocean components of climate models in the Arctic Ocean	thetao(K) so (0.001)	arctic_ocean/arctic_ocean.py
recipe_seaice_feedback.yml	3.3.4	Recipe to evaluate the negative ice growth- and ice thickness feedback	sit	seaice_feedback/negative_seaice_feedback.py
recipe_sea_ice_drift.yml	3.3.4	Recipe for sea ice drift evaluation	sic sithick sispeed	seaice_drift/seaice_drift.py
recipe_SeaIce.yml	3.3.4	Recipe for plotting sea ice diagnostics at the Arctic and Antarctic	sic	seaice/SeaIce_ancyc.ncl seaice/SeaIce_tsline.ncl seaice/SeaIce_polcon.ncl seaice/SeaIce_polcon_diff.ncl
Section 3.4: Detection of systematic biases in the physical climate: land				

https://doi.org/10.5194/gmd-2019-291
Preprint. Discussion started: 26 November 2019
© Author(s) 2019. CC BY 4.0 License.

Geoscientific Model Development Discussions

recipe_landcover.yml	3.4.1	Recipe for plotting the accumulated area, average fraction and bias of landcover classes in comparison to ESA_CCI_LC data for the full globe and large scale regions.	baresoilFrac grassFrac treeFrac shrubFrac cropFrac	landcover/landcover.py
recipe_albedolandcover.yml	3.4.2	Recipe for evaluate land cover-specific albedo values.	alb	landcover/albedolandcover.py
Section 3.5: Detection of biogeochemical biases				
recipe_anav13jclim.yml	3.5.1	Recipe to reproduce most of the figures of Anav et al. (2013)	tas pr tos nbp_grid lai_grid gpp_grid cSoil_grid cVeg_grid fgco2_grid	carbon_cycle/mvi.ncl carbon_cycle/main.ncl carbon_cycle/two_variables.ncl perfmetrics/main.ncl perfmetrics/collect.ncl
recipe_carvalhais2014nat.yml	3.5.2	Recipe to evaluated the biases in ecosystem carbon turnover time.	tau (non-CMOR variable, that is derived as the ratio of total ecosystem carbon stock and gross primary productivity)	regrid_areaweighted.py compare_tau_modelVobs_matrix.py compare_tau_modelVobs_climatebins.py compare_zonal_tau.py compare_zonal_correlations_tauVclimate.py
recipe_ocean_bgc.yml	3.5.3	Recipe to evaluate the marine biogeochemistry models of CMIP5. There are also some physical evaluation metrics.	thetao so no3 o2 si chl dfe talk intpp mfo fgco2	ocean/diagnostic_timeseries.py ocean/diagnostic_profiles.py ocean/diagnostic_maps.py ocean/diagnostic_model_vs_obs.py ocean/diagnostic_transects.py
recipe_eyring06jgr.yml	3.5.4	Recipe to reproduce stratospheric dynamics and chemistry figures from Eyring et al. (2006)	ta ua vt100 vmrch4 vmrh2o mnstrage vmrhcl vmrcly vmro3 toz	eyring06jgr/eyring06jgr_fig*.ncl

https://doi.org/10.5194/gmd-2019-291
Preprint. Discussion started: 26 November 2019
© Author(s) 2019. CC BY 4.0 License.

Geoscientific Model Development Discussions

Figures

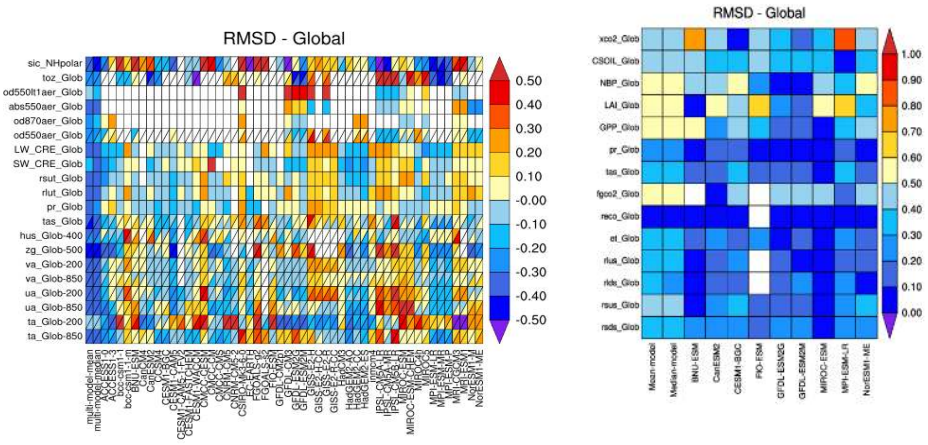

Figure 1. Relative space-time root-mean-square deviation (RMSD) calculated from the climatological seasonal cycle of the CMIP5 simulations. The years averaged depend on the years with observational data available. A relative performance is displayed, with blue shading indicating better and red shading indicating worse performance than the median of all model results. A diagonal split of a grid square shows the relative error with respect to the reference data set (lower right triangle) and the alternative data set (upper left triangle). White boxes are used when data are not available for a given model and variable. The performance metrics are shown separately for atmosphere, ocean and sea-ice (left), and land (right). The figure shows that performance varies across CMIP5 models and variables, with some models comparing better with observations for one variable and another model performing better for a different variable. Except for global average temperatures at 200 hPa (ta_Glob-200) where most but not all models have a systematic bias, the multi-model mean outperforms any individual model. Extended from Figure 9.7 of Flato et al. (2013) and produced with *recipe_perfmetrics_CMIP5.yml.*, see details in Section 3.1.1.

https://doi.org/10.5194/gmd-2019-291
Preprint. Discussion started: 26 November 2019
© Author(s) 2019. CC BY 4.0 License.

Geoscientific Model Development Discussions

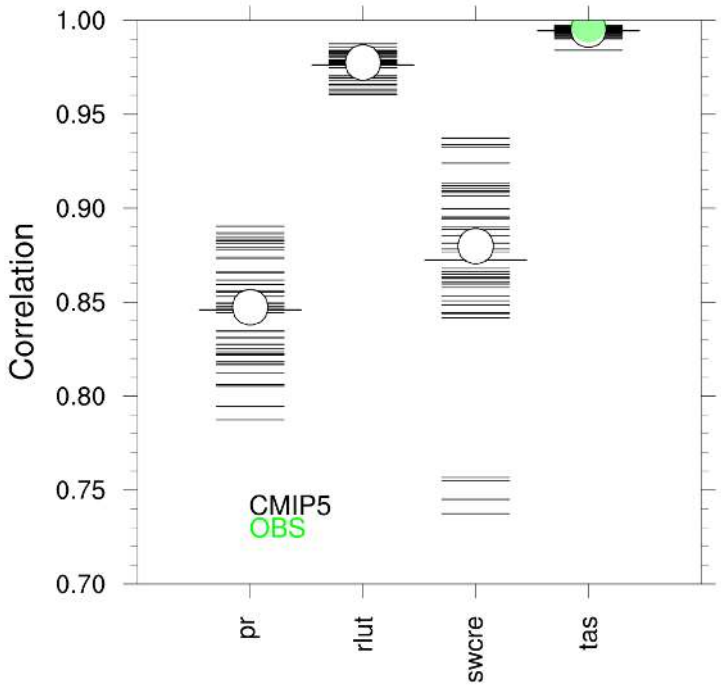

Figure 2. Centred pattern correlations for the annual mean climatology over the period 1980-1999 between models and observations. Results for individual CMIP5 models are shown (thin dashes), as well as the ensemble average (longer thick dash) and median (open circle). The correlations are computed between the models and the reference dataset. When an alternate observational dataset is present, its correlation to the reference dataset is also shown (solid green circles). The models are first regridded to 4° longitude by 5° latitude to ensure the pattern correlations give a fair comparison across all model resolutions. The figure shows both a large model spread as well as a large spread in the correlation depending on the variable, signifying that some aspects of the simulated climate agree better with observations than others. Similar to Figure 9.6 of Flato et al. (2013) and produced with *recipe_flato13ipcc.yml*, see details in Section 3.1.2.

https://doi.org/10.5194/gmd-2019-291
Preprint. Discussion started: 26 November 2019
© Author(s) 2019. CC BY 4.0 License.

Geoscientific Model Development Discussions
Open Access
EGU

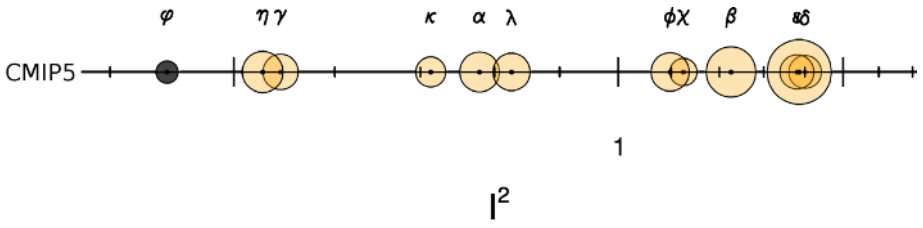

α: CNRM-CM5
β: CSIRO-Mk3-6-0
χ: GFDL-ESM2G
δ: MIROC-ESM
ε: MIROC-ESM-CHEM
ϕ: MIROC5
γ: MPI-ESM-LR
η: MPI-ESM-MR
ι: MRI-CGCM3
φ: multi-model-mean
κ: NorESM1-M
λ: NorESM1-ME

Figure 3. Single Model Performance Index I2 for individual models (orange circles). The size of each circle represents the 95% confidence interval of the bootstrap ensemble. The black circle indicates the I2 of the CMIP5 multi-model mean. The I2 values vary around one, with underperforming models having a value greater than one, while values below one represent more accurate models. This allows for a quick estimation which models are performing the best on average across the sampled variables and in this case shows that the common practice of taking the multi-model mean as best overall model is accurate. Similar to Reichler and Kim (2008) Figure 1 and produced with *recipe_smpi.yml*, see details in Section 3.1.3.

https://doi.org/10.5194/gmd-2019-291
Preprint. Discussion started: 26 November 2019
© Author(s) 2019. CC BY 4.0 License.

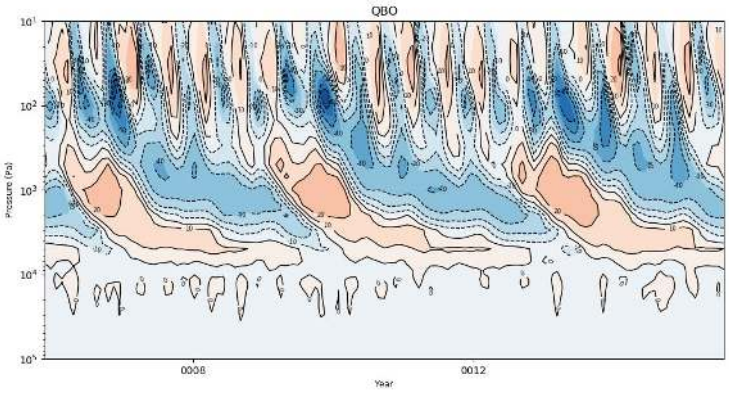

Figure 4. AutoAssess time-height plot of zonal mean zonal wind averaged between 5S and 5N for UKESM1-0-LL over the period 1995-2014. Zonal wind anomalies propagate downward from the upper stratosphere. The figure shows that the period of the QBO in this model is about 6 years, significantly longer than the observed period of ~2.3 years. Produced with recipe_*autoassess_*.yml.*, see details in Section 3.1.4.

https://doi.org/10.5194/gmd-2019-291
Preprint. Discussion started: 26 November 2019
© Author(s) 2019. CC BY 4.0 License.

Geoscientific Model Development Discussions

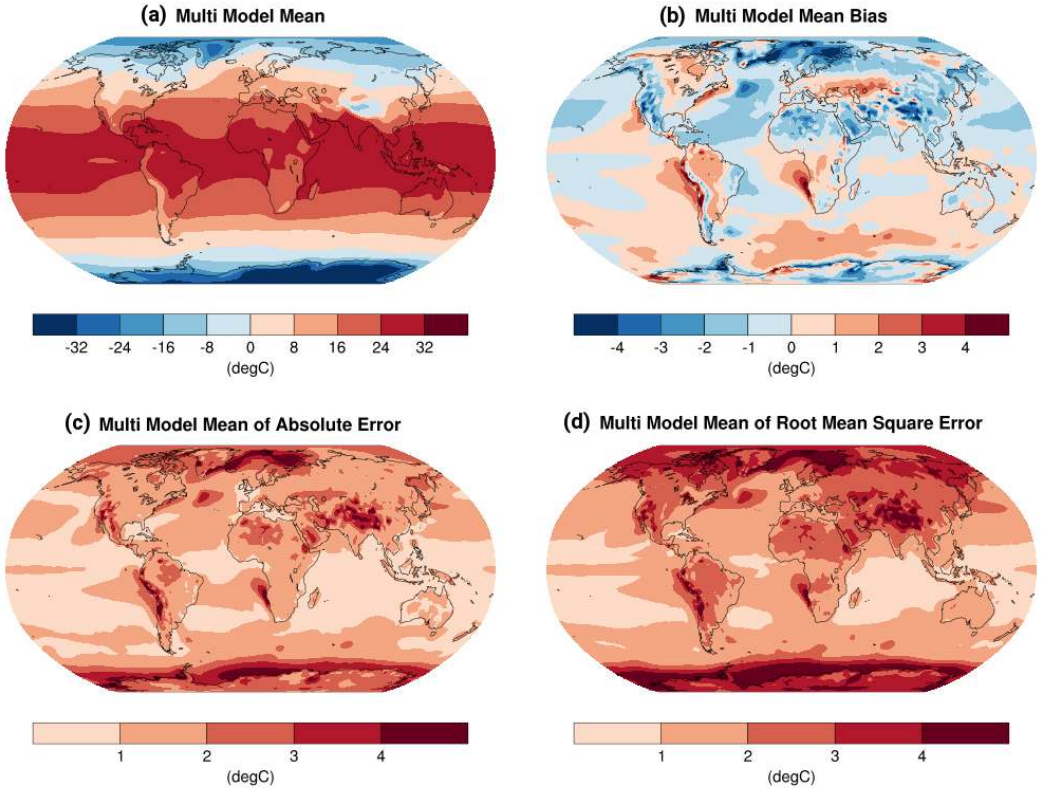

Figure 5. Annual-mean surface (2 m) air temperature (°C) for the period 1980-2005. (a) Multi-model (ensemble) mean constructed with one realization of all available models used in the CMIP5 historical experiment. (b) Multi-model mean bias as the difference between the CMIP5 multi-model mean and the climatology from ECMWF reanalysis of the global atmosphere and surface conditions (ERA)-Interim (Dee et al., 2011). (c) Mean absolute model error with respect to the climatology from ERA-Interim. (d) Mean root mean square error of the seasonal cycle with respect to the ERA-Interim. The multi-model mean near-surface temperature agrees with ERA-Interim mostly within ±2 C. Larger biases can be seen in regions with sharp gradients in temperature, for example in areas with high topography such as the Himalaya, the sea ice edge in the North Atlantic, and over the coastal upwelling regions in the subtropical oceans. Updated from Fig. 9.2 of Flato et al. (2013) and produced with *recipe_flato13ipcc.yml*, see details in Section 3.2.1.

https://doi.org/10.5194/gmd-2019-291
Preprint. Discussion started: 26 November 2019
© Author(s) 2019. CC BY 4.0 License.

Geoscientific Model Development Discussions
Open Access
EGU

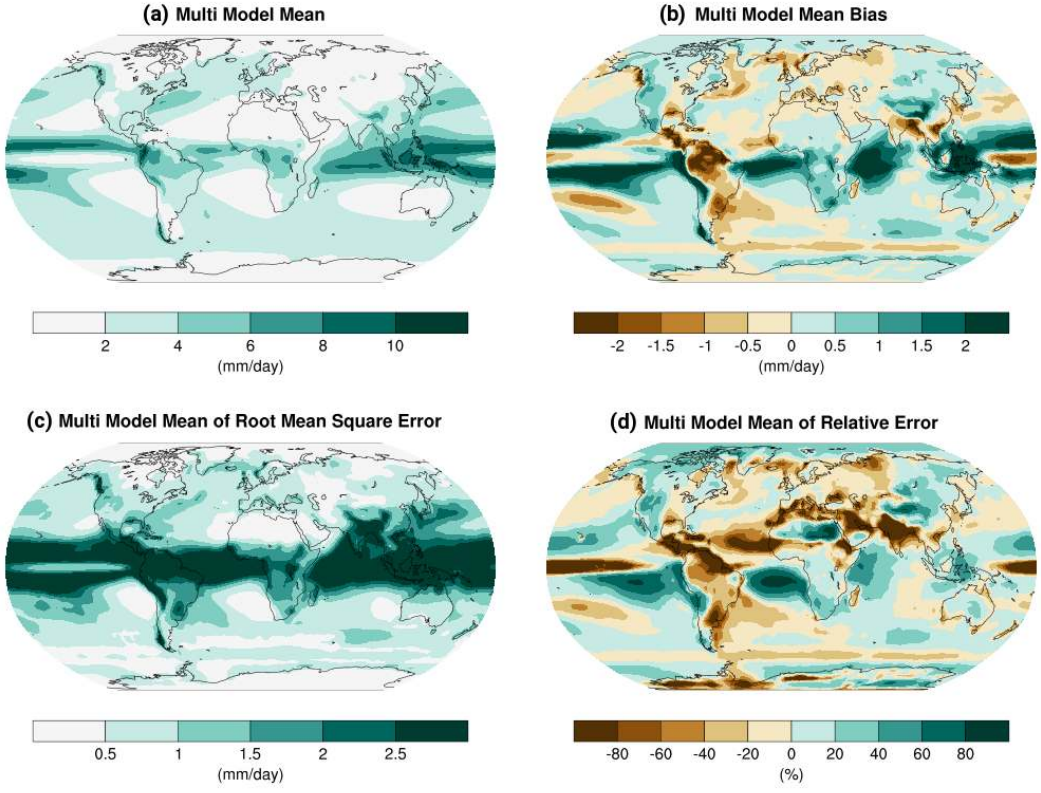

Figure 6. Annual-mean precipitation rate (mm day^{-1}) for the period 1980-2005. (a) Multi-model (ensemble) mean constructed with one realization of all available models used in the CMIP5 historical experiment. (b) Multi-model mean bias as the difference between the CMIP5 multi-model mean and the analyses from the Global Precipitation Climatology Project (Adler et al., 2003). (c) Mean root mean square error of the seasonal cycle with respect toobservations. (d) Mean relative model error with respect to observations. Biases in the simulated multi-model mean precipitation include too low precipitation along the Equator in the western Pacific and too high precipitation amounts in the tropics south of the Equator. Updated from Fig. 9.4 of Flato et al. (2013) and produced with *recipe_flato13ipcc.yml*, see details in Section 3.2.1.

https://doi.org/10.5194/gmd-2019-291
Preprint. Discussion started: 26 November 2019
© Author(s) 2019. CC BY 4.0 License.

Geoscientific Model Development Discussions

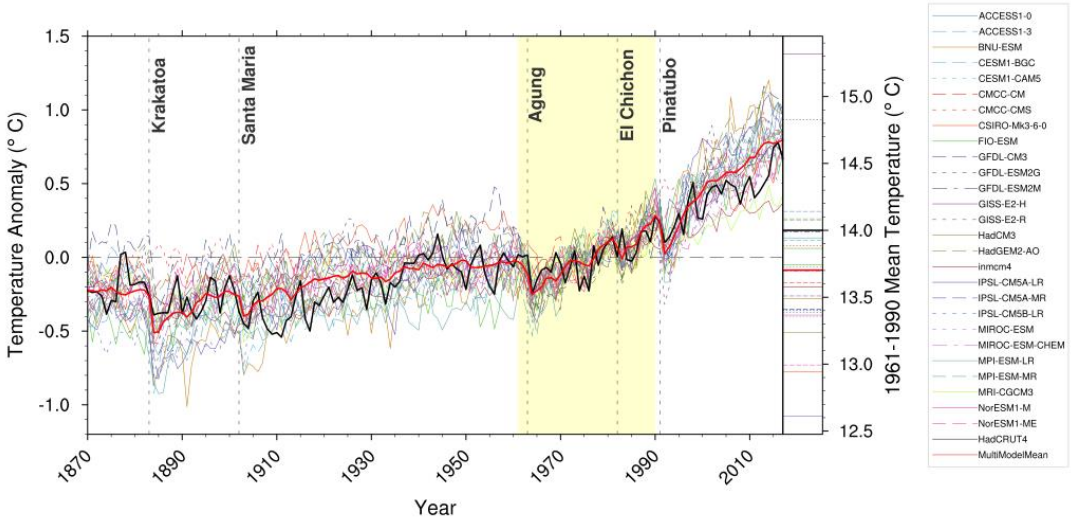

Figure 7. Anomalies in annual and global mean surface temperature of CMIP5 models and HadCRUT4 observations. Yellow shading indicates the reference period (1961 -1990); vertical dashed grey lines represent times of major volcanic eruptions. The right bar shows the global mean surface temperature of the reference period. CMIP5 model data are subsampled by the HadCRUT4 observational data mask and processed like described in Jones et al. (2013). All simulations are historical experiments up to and including 2005 and the RCP 4.5 scenario after 2005. Overall, the models represent quite good the annual global-mean surface temperature increase over the historical period including the more rapid warming in the second half of the 20th century and the cooling immediately following large volcanic eruptions. Extended from Figure 9.8 of Flato et al. (2013) and produced with *recipe_flato13ipcc.yml*, see details in Section 3.2.1.

https://doi.org/10.5194/gmd-2019-291
Preprint. Discussion started: 26 November 2019
© Author(s) 2019. CC BY 4.0 License.

Geoscientific Model Development Discussions

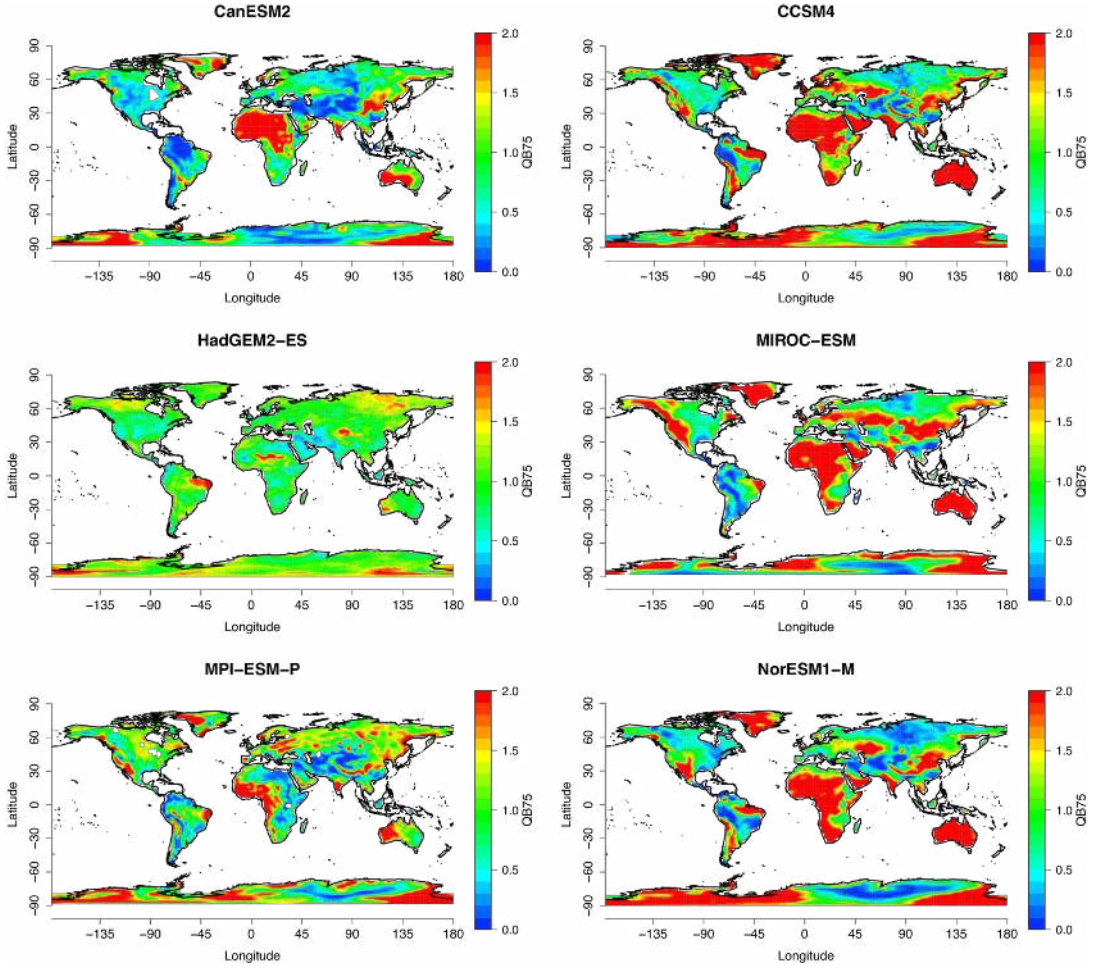

Figure 8. Quantile (75%) bias evaluated for an example subset of CMIP5 models over the period 1979 to 2005 using GPCP-SG v 2.3 gridded precipitation as a reference dataset. Biases depend on models and geographical regions but similar patterns can be recognized (see e.g., overestimation over Africa for models in the right column and the underestimation pattern crossing central Asia from Siberia to the Arabic pensinsula). The HadGEM2-ES model show a largely reduced bias as compared to the other models in this subset. Similar to Mehran et al. (2014) and produced with *recipe_quantilebias.yml*. See details in Section 3.2.2.

https://doi.org/10.5194/gmd-2019-291
Preprint. Discussion started: 26 November 2019
© Author(s) 2019. CC BY 4.0 License.

Geoscientific Model Development Discussions
Open Access
EGU

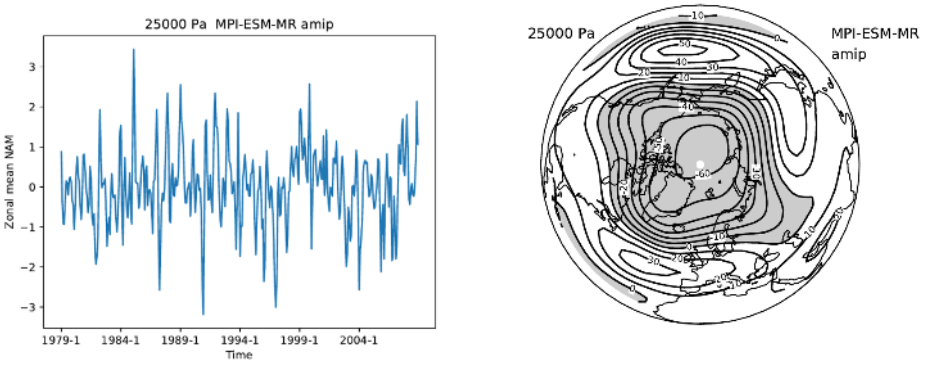

Figure 9. The zonal mean NAM index (left) at 250 hPa for the atmosphere-only CMIP5 simulation of the Max Planck Institute for Meteorology (MPI-ESM-MR) model, and the regression map of the monthly geopotential height on this zonal-mean NAM index (right). Note the variability on different temporal scales of the index, from monthly to decadal. The well-known annular pattern, with opposite anomalies between polar and mid-latitudes, can be appreciated in the regression plot. Similar to Figure 2 of Baldwin and Thompson [2009] and produced with *recipe_zmnam.yml*, see details in Section 3.2.3.1.

https://doi.org/10.5194/gmd-2019-291
Preprint. Discussion started: 26 November 2019
© Author(s) 2019. CC BY 4.0 License.

Geoscientific Model Development Discussions
Open Access
EGU

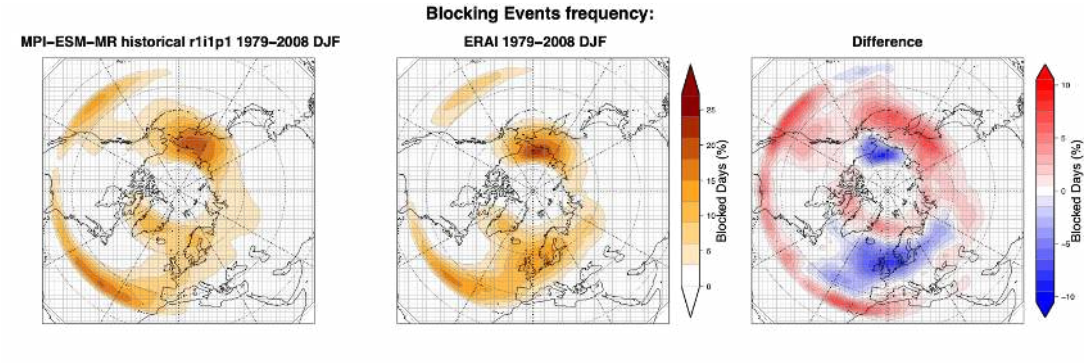

1105 **Figure 10. 2-d Blocking Events following the Davini et al. (2012) index over the 1979-2008 DJF period for (left) CMIP5 MPI-ESM-MR historical r1i1p1 run (center) ERA-Interim Reanalysis and (right) their differences. The MPI-ESM-MR shows the well-known underestimation of atmospheric blocking – typical of many climate models – over Central Europe, where blocking frequencies are about the half when compared to reanalysis. Slight overestimation of low latitude blocking and North Pacific blocking can be also observed, while Greenland blocking frequencies show**
1110 **negligible bias. Produced with *recipe_miles_block.yml*, see details in Section 3.2.3.2.**

https://doi.org/10.5194/gmd-2019-291
Preprint. Discussion started: 26 November 2019
© Author(s) 2019. CC BY 4.0 License.

Geoscientific Model Development Discussions

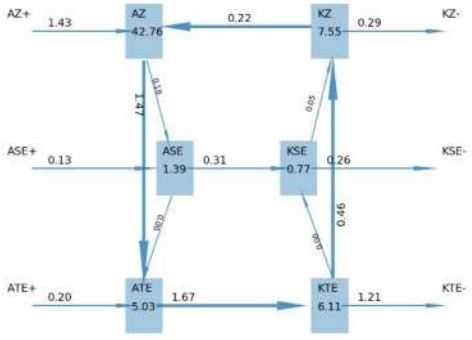

Figure 11. A Lorenz Energy Cycle flux diagram for one year of a CMIP5 model pre-industrial control run (cfr. (Ulbrich et al., 1991)). "A" stands for available potential energy (APE), "K" for kinetic energy (KE), "Z" for zonal mean, "S" for stationary eddies, "T" for transient eddies. "+" indicates source of energy, "-" a sink. For the energy reservoirs, the unit of measure is J*m-2, for the energy conversion terms, the unit of measure is W*m-2. Most of the energy is clearly stored in terms of APE in the zonal mean flux. The energy conversion happens almost instantly in converting APE energy from the zonal mean flow into the eddy and through them into KE. The two processes are usually referred to as "baroclinic conversion". For a non-steady state equilibrium system, the APE source has to equal the KE dissipation (through frictional heating in the zonal mean flow and eddies). Similar to Figure 5 of Lembo et al. (2019) and produced with *recipe_thermodyn_diagtool.yml,* see details in Section 3.2.4.

https://doi.org/10.5194/gmd-2019-291
Preprint. Discussion started: 26 November 2019
© Author(s) 2019. CC BY 4.0 License.

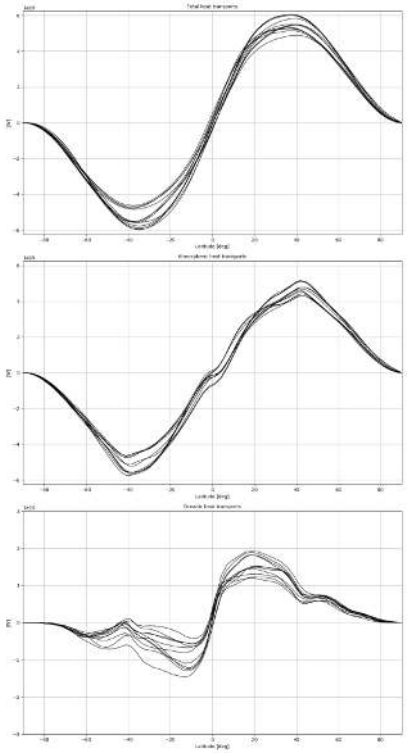

Figure 12. annual mean meridional sections of zonal mean meridional total (top), atmospheric (middle), oceanic (bottom) heat transports for 12 CMIP5 models control runs. Transports are implied from meridionally integrating TOA, atmospheric and surface energy budgets (cfr. Trenberth et al. (2001)), then applying the usual correction accounting for energy imbalances, as in Carissimo et al. (1985). Values are in W. The model spread has roughly the same magnitude in the atmospheric and oceanic transports, but its relevance is much larger for the oceanic transports. The model spread is also crucial in the magnitude and sign of the atmospheric heat transports across the Equator, given its implications for the atmospheric general circulation. Add brief discussion of the results. Similar to Figure 8 of Lembo et al. (2019) and produced with *recipe_thermodyn_diagtool.yml,* see details in Section 3.2.4.

https://doi.org/10.5194/gmd-2019-291
Preprint. Discussion started: 26 November 2019
© Author(s) 2019. CC BY 4.0 License.

Geoscientific Model Development Discussions
Open Access
EGU

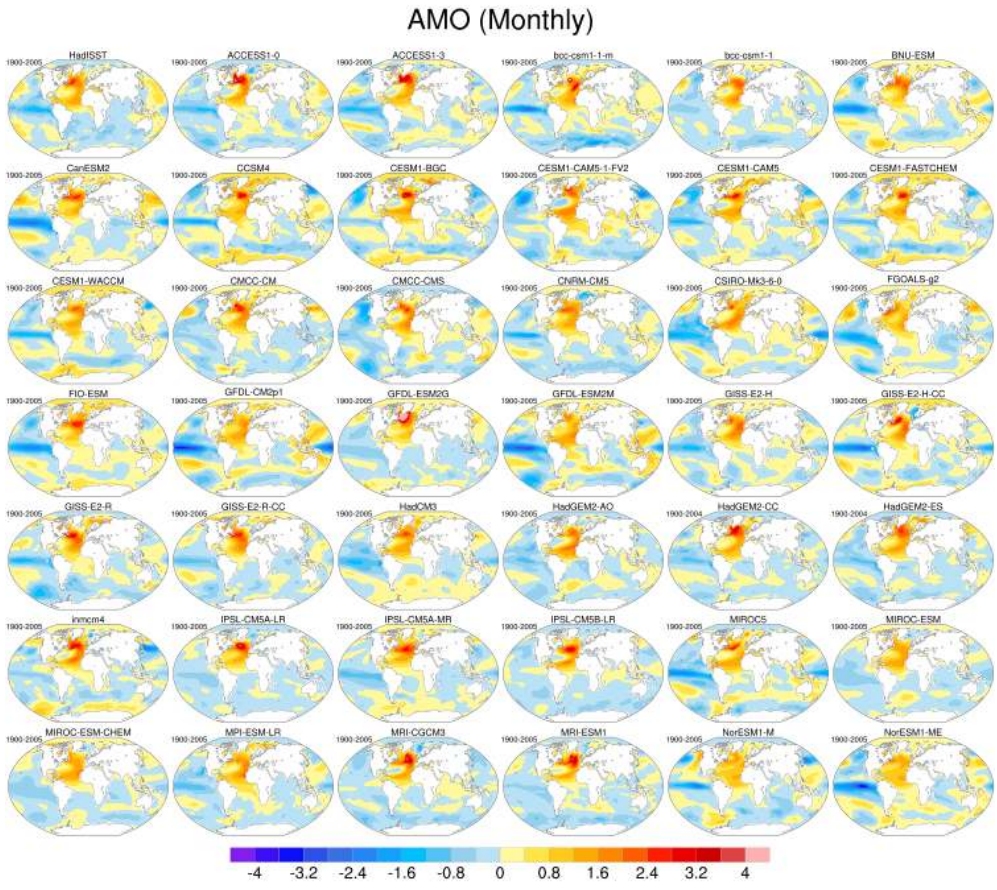

Figure 13. Global ENSO teleconnections during the peak phase (December-February) as simulated by 41 CMIP5 models (individual panels labelled by model name) and observations (upper left panel) for the historical period (1900-2005 for models and 1920-2017 for observations). These patterns are based on composite differences between all El Nino events and all La Nina events (using a +/- 1 standard deviation threshold of the Nino3.4 SST Index) occurring in the period of record. Color shading denotes SST and terrestrial TREFHT (◦C), and contours denote SLP (contour interval of 2hPa, with negative values dashed). The period of record is given in the upper left of each panel, and the number of El Nino and La Nina events that contribute to the composites are given in the upper right (for example, "18/14" denotes 18 El Nino events and 14 La Nina events). Observational composites use ERSSTv5 for SST, BEST for TAS and ERA20C updated with ERA-I for PSL. Models produce a wide range of ENSO amplitudes and teleconnections. Note that even when based on over 100 years of record, the ENSO composites are subject to uncertainty due to sampling variability (Deser et al., 2017) ,Deser et al., 2018). Figure produced with *recipe_CVDP.yml.*, see details in Section 3.2.5.1.

https://doi.org/10.5194/gmd-2019-291
Preprint. Discussion started: 26 November 2019
© Author(s) 2019. CC BY 4.0 License.

Geoscientific Model Development Discussions
Open Access
EGU

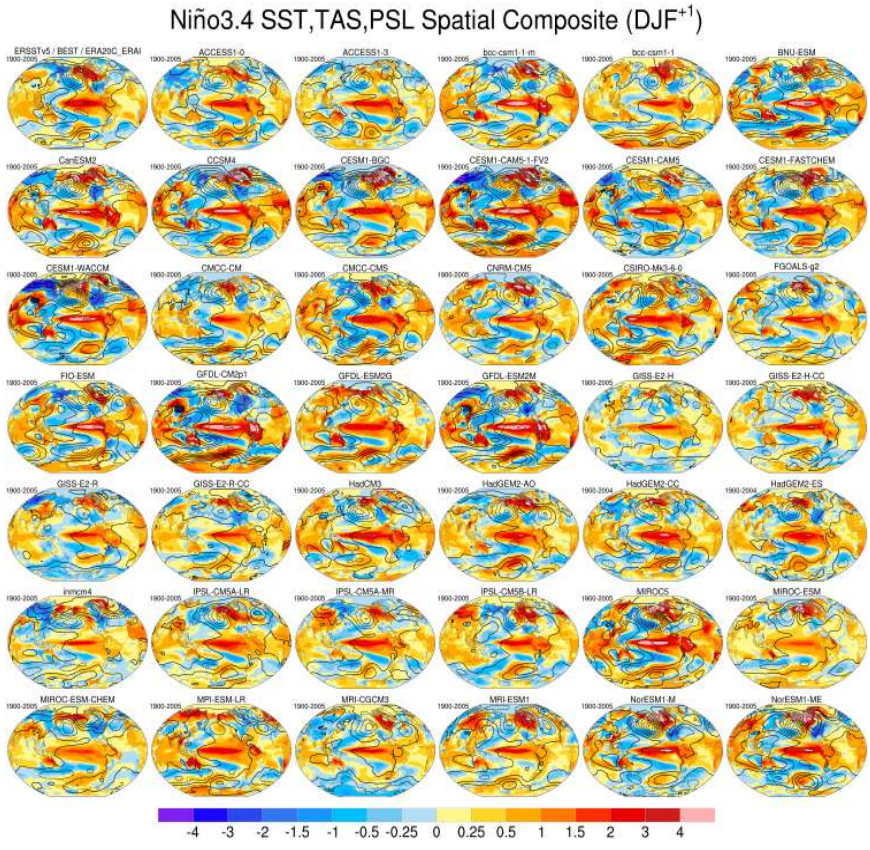

Figure 14. Representation of the AMO in 41 CMIP5 models (individual panels labelled by model name) and observations (upper left panel) for the historical period (1900-2005 for models and 1920-2017 for observations). These patterns are based regressing monthly SST anomalies (denoted SSTA*) at each grid box onto the timeseries of the AMO SSTA* Index (defined as SSTA* averaged over the North Atlantic 0-60N, 80W-0W), where the asterisk denotes that the global (60N-60S) mean SSTA has been subtracted from SSTA at each grid box following Trenberth and Shea (2006). The pattern of SSTA* associated with the AMO is generally realistically simulated by models within the North Atlantic basin, although its amplitude varies. However, outside of the North Atlantic, the models show a wide range of spatial patterns and polarities of the AMO. Figure produced with *recipe_CVDP.yml.*, see details in Section 3.2.5.1.

https://doi.org/10.5194/gmd-2019-291
Preprint. Discussion started: 26 November 2019
© Author(s) 2019. CC BY 4.0 License.

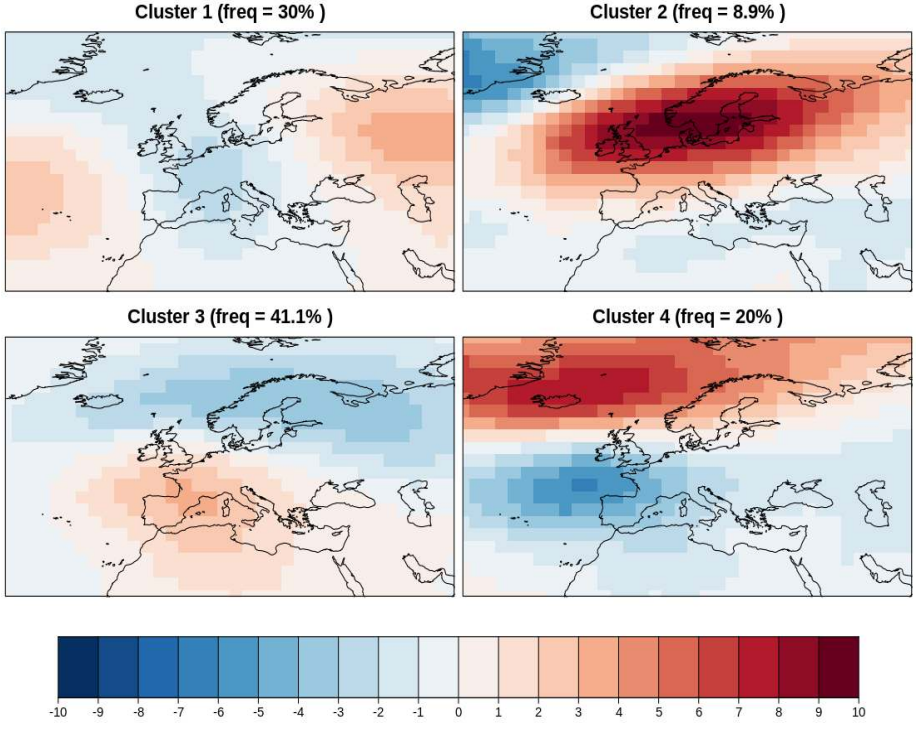

Figure 15. Four modes of variability for autumn (September-October-November) in the North Atlantic European Sector during the reference period 1971-2000 for the BCC-CSM1-1 historical simulations. The frequency of occurrence of each variability mode is indicated in the title of each map. The four clusters are reminiscent of the Atlantic Ridge, the Scandinavian blocking, the NAO+ and the NAO- pattern, respectively. Result for *recipe_modes_of_variability.yml*, see details in Section 3.2.5.2.

https://doi.org/10.5194/gmd-2019-291
Preprint. Discussion started: 26 November 2019
© Author(s) 2019. CC BY 4.0 License.

Geoscientific Model Development Discussions
Open Access
EGU

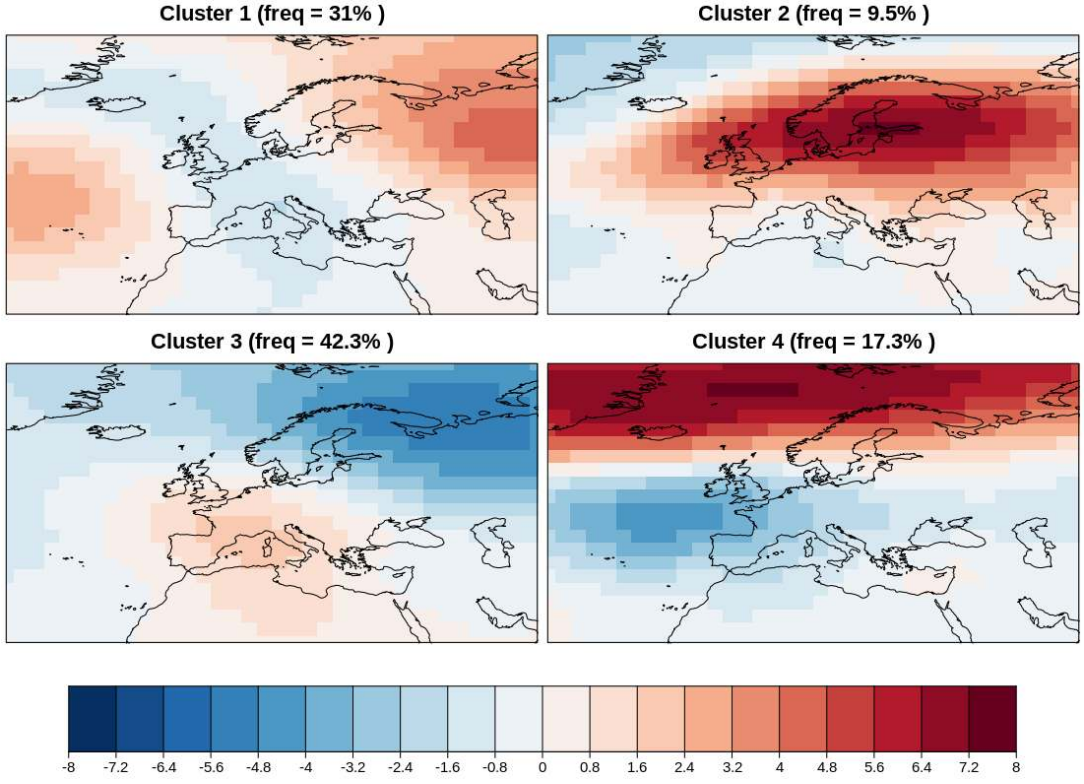

Figure 16. Four modes of variability for autumn (September-October-November) in the North Atlantic European Sector for the RCP 8.5 scenario using BCC-CSM1-1 future projection during the period 2020-2075. The frequency of occurrence of each variability mode is indicated in the title of each map. The four clusters are reminiscent of the Atlantic Ridge, the Scandinavian blocking, the NAO+ and the NAO- pattern, respectively. Result for *recipe_modes_of_variability.yml*, see details in Section 3.2.5.2.

https://doi.org/10.5194/gmd-2019-291
Preprint. Discussion started: 26 November 2019
© Author(s) 2019. CC BY 4.0 License.

Geoscientific Model Development Discussions

	Obs 1	Obs 2	Obs 3	Obs 4
Pre 1	107.49	349.18	304.09	375.63
Pre 2	280.68	149.67	405.82	449.04
Pre 3	303.96	497.06	112.14	505.27
Pre 4	415.69	529.9	491.15	122.16

1170 **Figure 17. RMSE between the spatial patterns obtained for the future 'Pre' (2020-2075) and the reference 'Obs' (1971-2000) modes of variability from the BCC-CSM1-1 simulations in autumn (September-October-November). Low RMSE values along the diagonal show that the modes of variability simulated by the future projection (Figure 16) match the reference modes of variability (Figure 15). Result for *recipe_modes_of_variability.yml* see details in Section 3.2.5.2.**

https://doi.org/10.5194/gmd-2019-291
Preprint. Discussion started: 26 November 2019
© Author(s) 2019. CC BY 4.0 License.

Geoscientific Model Development Discussions
Open Access
EGU

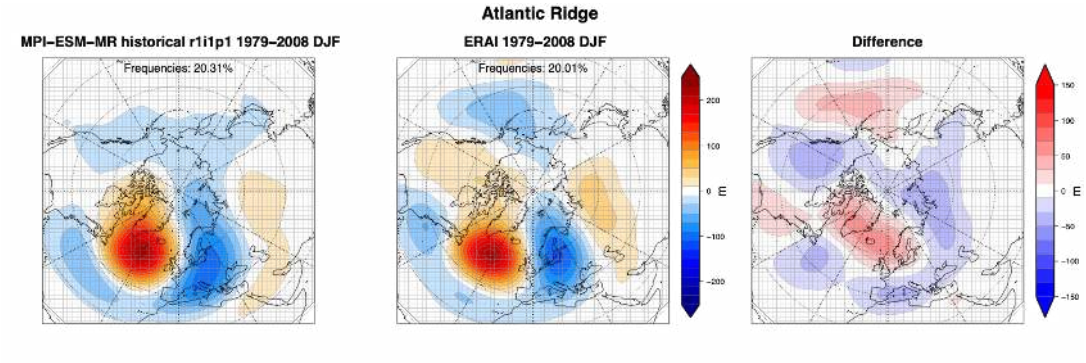

1175

Figure 18. 500 hPa geopotential height anomalies associated to the Atlantic Ridge weather regime over the 1979-2008 DJF period for (left) CMIP5 MPI-ESM-MR historical r1i1p1 run (center) ERA-Interim Reanalysis and (right) their differences. The frequency of occupancy of each regime is reported on the top of each panel. The Atlantic ridge regimes, which is usually badly simulated by climate models, it is reproduced with the right frequency of occupancy
1180 **and pattern in MPI-ESM-MR when compared to ERA-Interim reanalysis. Produced with *recipe_miles_regimes.yml*, see details in Section 3.2.5.2.**

https://doi.org/10.5194/gmd-2019-291
Preprint. Discussion started: 26 November 2019
© Author(s) 2019. CC BY 4.0 License.

Geoscientific Model Development Discussions

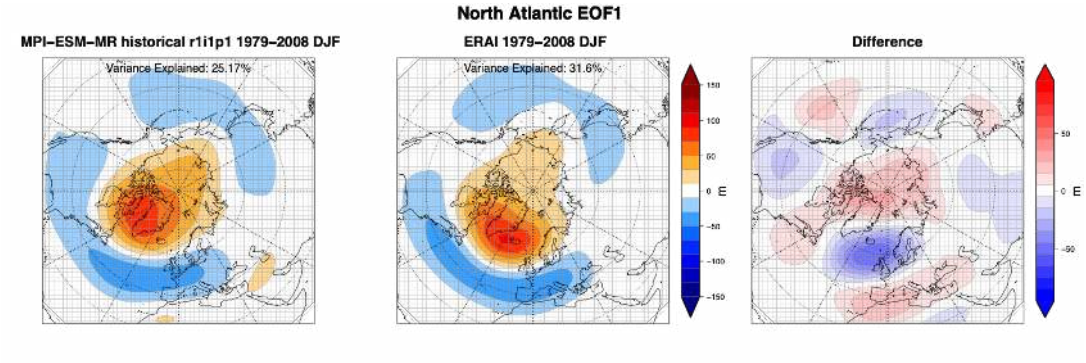

1185 **Figure 19. Linear regression over the 500hPa geopotential height of the first North Atlantic EOF (i.e. the North Atlantic Oscillation, NAO) over the 1979-2008 DJF period for (left) CMIP5 MPI-ESM-MR historical r1i1p1 run (center) ERA-Interim Reanalysis and (right) their differences. The variance explained is reported on the top of each panel. It is possible to see how the NAO is well represented by MPI-ESM-LR, although the variance explained is underestimated and the northern center of action, which is found close to Iceland in reanalysis, is westward displaced over Greenland. Produced with *recipe_miles_eof.yml*, see details in Section 3.2.5.3.**

1190

https://doi.org/10.5194/gmd-2019-291
Preprint. Discussion started: 26 November 2019
© Author(s) 2019. CC BY 4.0 License.

Geoscientific Model Development Discussions

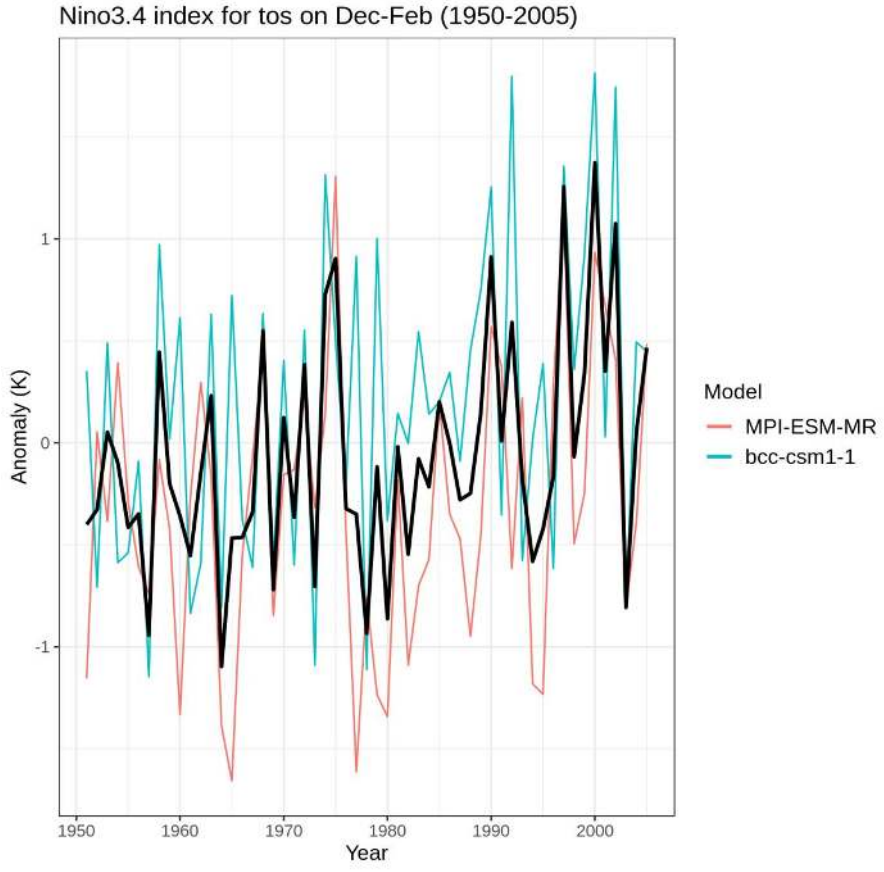

Figure 20. Time series of the standardized sea surface temperature (tos) area averaged over the Nino 3.4 region during the boreal winter (December-January-February). The time series correspond to the MPI-ESM-MR (red) and BCC-CSM1-1 (blue) models and their mean (black) during the period 1950-2005 for the ensemble r1p1i1 of the historical simulations. Produced with *recipe_combined_indices.yml*., see details in Section 3.2.5.4.

https://doi.org/10.5194/gmd-2019-291
Preprint. Discussion started: 26 November 2019
© Author(s) 2019. CC BY 4.0 License.

Geoscientific Model Development Discussions

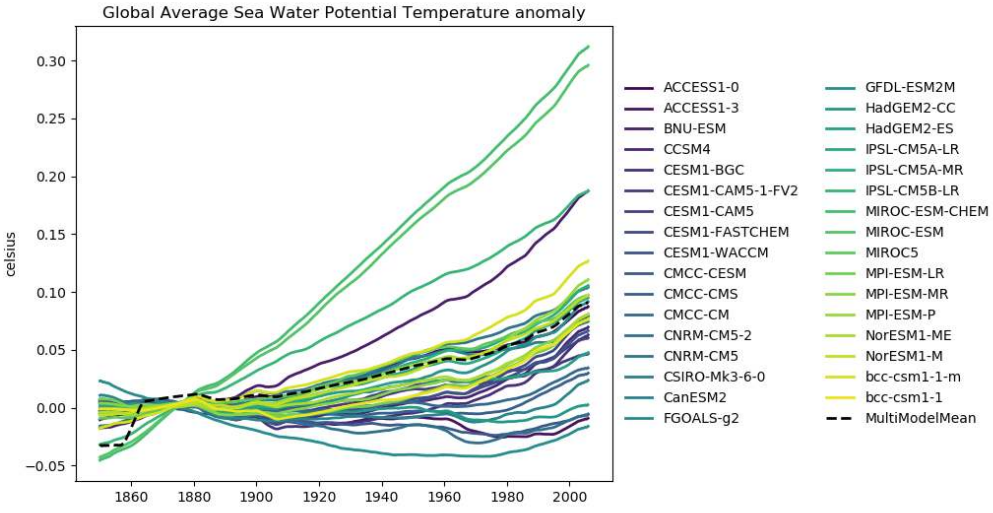

Figure 21. The volume weighted global mean temperature anomaly in several CMIP5 models, in the historical experiment, in the r1i1j1 ensemble member, with a 6 year moving average smoothing function. The anomaly is calculated against the mean of all years in the historical experiment before 1900. The multi model mean is shown as a dashed line. Nearly all CMIP5 models show an increase in the mean temperature of the ocean over the historical period. Produced with *recipe_ocean_scalar_fields.yml* described in Section 3.3.1.

https://doi.org/10.5194/gmd-2019-291
Preprint. Discussion started: 26 November 2019
© Author(s) 2019. CC BY 4.0 License.

Geoscientific Model Development Discussions
Open Access
EGU

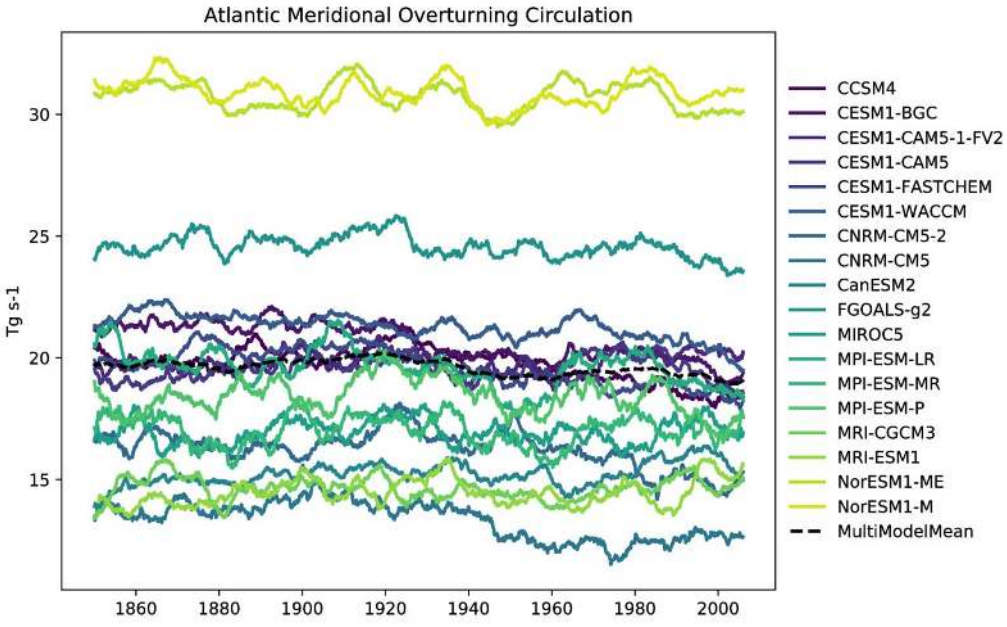

1205 **Figure 22. The Atlantic Meridional Overturn Circulation (AMOC) in several CMIP5 models, in the historical experiment, in the r1i1j1 ensemble member, with a 6 year moving average smoothing function. The multi model mean is shown as a dashed line. The AMOC indicates the strength of the northbound current and this current transfers heat from tropical water to the North Atlantic. All CMIP5 models show some interannual variability in the AMOC behaviour, but it is not clear whether the decline in the multi model mean over the historical period is statistically significant. Produced with *recipe_ocean_amoc.yml* described in Section 3.3.1.**

https://doi.org/10.5194/gmd-2019-291
Preprint. Discussion started: 26 November 2019
© Author(s) 2019. CC BY 4.0 License.

Geoscientific Model Development Discussions

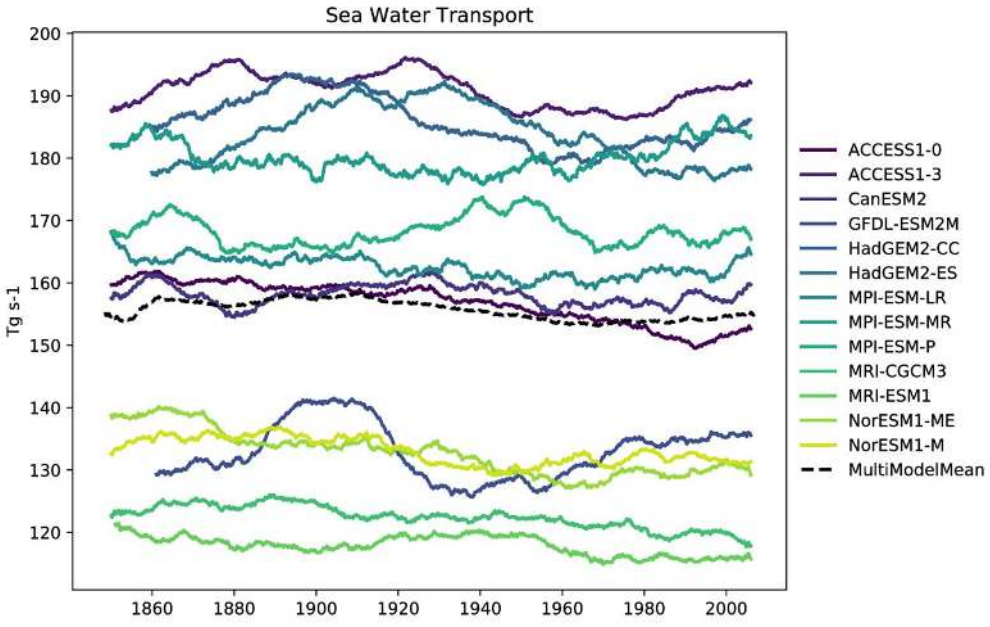

1210

Figure 23. The Antarctic circumpolar current calculated through Drake Passage for a range of CMIP5 models in the historical experiment in the r1i1j1 ensemble member, with a 6 year moving average smoothing function. The multi model mean is shown as a dashed line. The ACC was recently measured through the Drake Passage at 173.3±10.7 Sv [Donohue et al., 2016], and four of the CMIP5 models fall within this range. Produced with *recipe_ocean_amoc.yml* described in Section 3.3.1.

1215

https://doi.org/10.5194/gmd-2019-291
Preprint. Discussion started: 26 November 2019
© Author(s) 2019. CC BY 4.0 License.

Geoscientific Model Development Discussions
Open Access
EGU

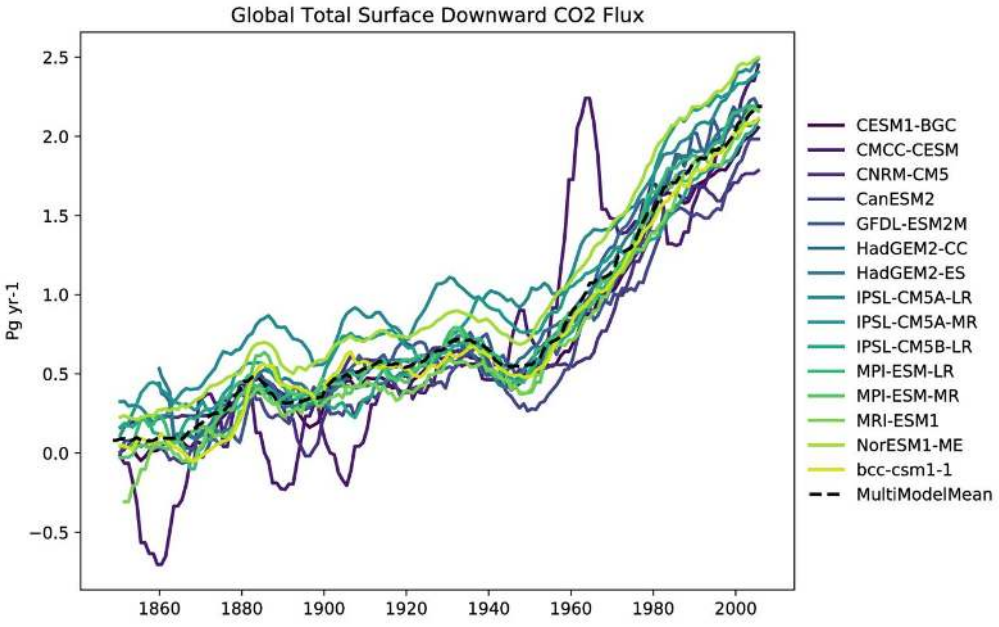

Figure 24. The global total air to sea flux of CO2 for a range of CMIP5 models in the historical experiment in the r1i1j1 ensemble member, with a 6 year moving average smoothing function. The multi model mean is shown as a dashed line. These models agree very closely on the behaviour of the air to sea flux of CO_2 over the historical period; all models show an increase from close to zero, and rising up to approximately 2 Pg of Carbon per year by the start of the 21st century. Produced with *recipe_ocean_scalar_fields.yml* described in Section 3.3.1.

https://doi.org/10.5194/gmd-2019-291
Preprint. Discussion started: 26 November 2019
© Author(s) 2019. CC BY 4.0 License.

Geoscientific Model Development Discussions
Open Access
EGU

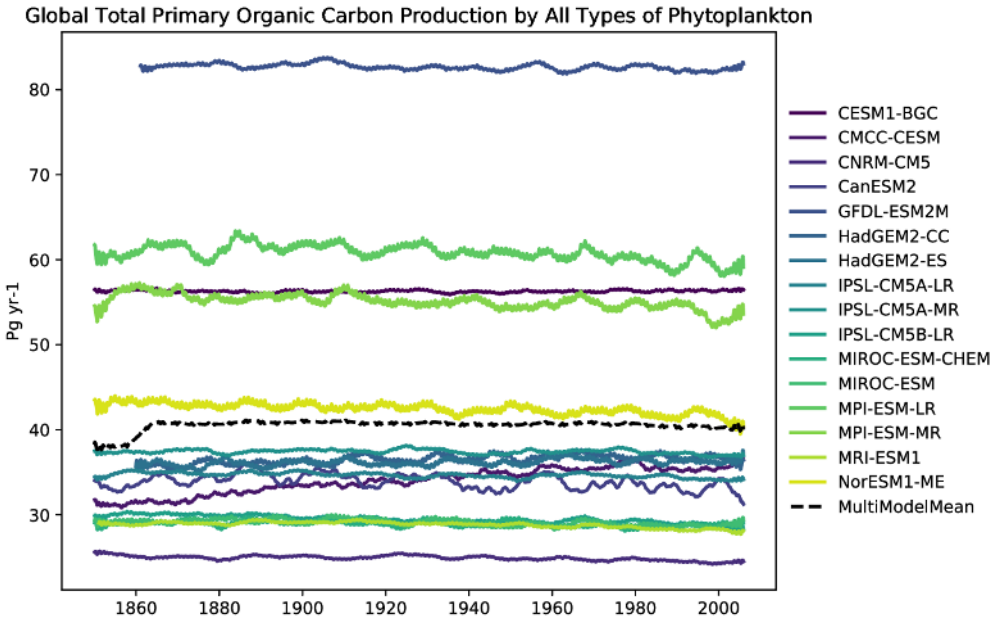

1225 **Figure 25. The global total integrated primary production from phytoplankton for a range of CMIP5 models in the historical experiment in the r1i1j1 ensemble member, with a 6 year moving average smoothing function. The multi model mean is shown as a dashed line. All CMIP5 models show little inter-annual variability in the integrated marine primary production, and there is no clear trend in the multi model mean. Produced with *recipe_ocean_scalar_fields.yml* described in Section 3.3.1.**

https://doi.org/10.5194/gmd-2019-291
Preprint. Discussion started: 26 November 2019
© Author(s) 2019. CC BY 4.0 License.

Geoscientific Model Development Discussions

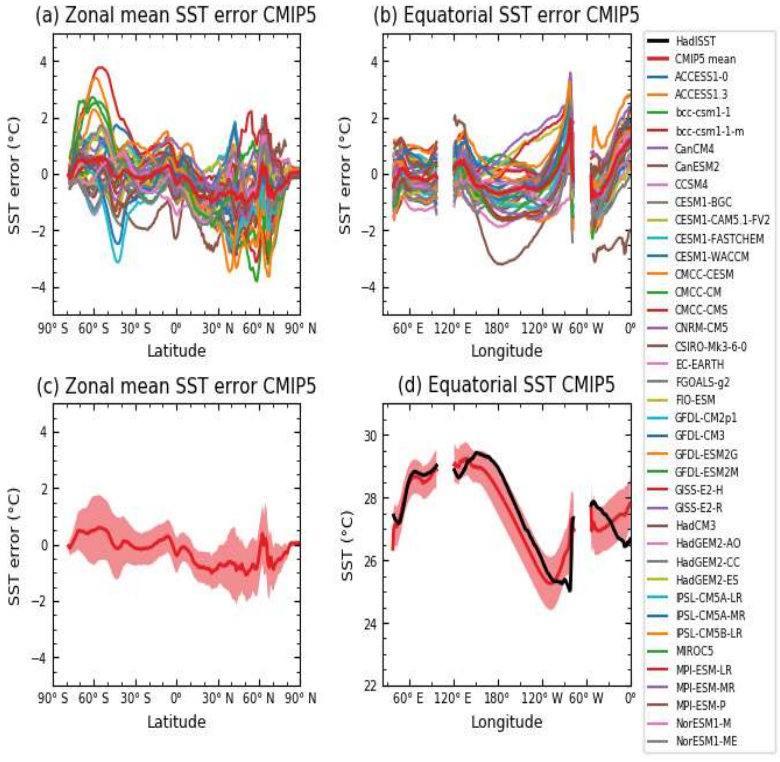

Figure 26. (a) Zonally averaged sea surface temperature (SST) error in CMIP5 models. (b) Equatorial SST error in CMIP5 models. (c) Zonally averaged multi-model mean SST error for CMIP5 together with inter-model standard deviation (shading). (d) Equatorial multi-model mean SST in CMIP5 together with inter-model standard deviation (shading) and observations (black). Model climatologies are derived from the 1979-1999 mean of the historical simulations. The Hadley Centre Sea Ice and Sea Surface Temperature (HadISST) (Rayner et al., 2003) observational climatology for 1979-1999 is used as a reference for the error calculation (a), (b), and (c); and for observations in (d). This figure is a reproduction of Fig. 9.14 of AR5 and shows the overall good agreement of the CMIP5 models among themselves as well as compared to observations, but also highlights the global areas with largest uncertainty and biggest room for improvement. This is an important benchmark for the upcoming CMIP6 ensemble of models. It is produced as part of *recipe_flato13ipcc.yml* and documented in Section 3.3.1.

https://doi.org/10.5194/gmd-2019-291
Preprint. Discussion started: 26 November 2019
© Author(s) 2019. CC BY 4.0 License.

Geoscientific Model Development Discussions
Open Access
EGU

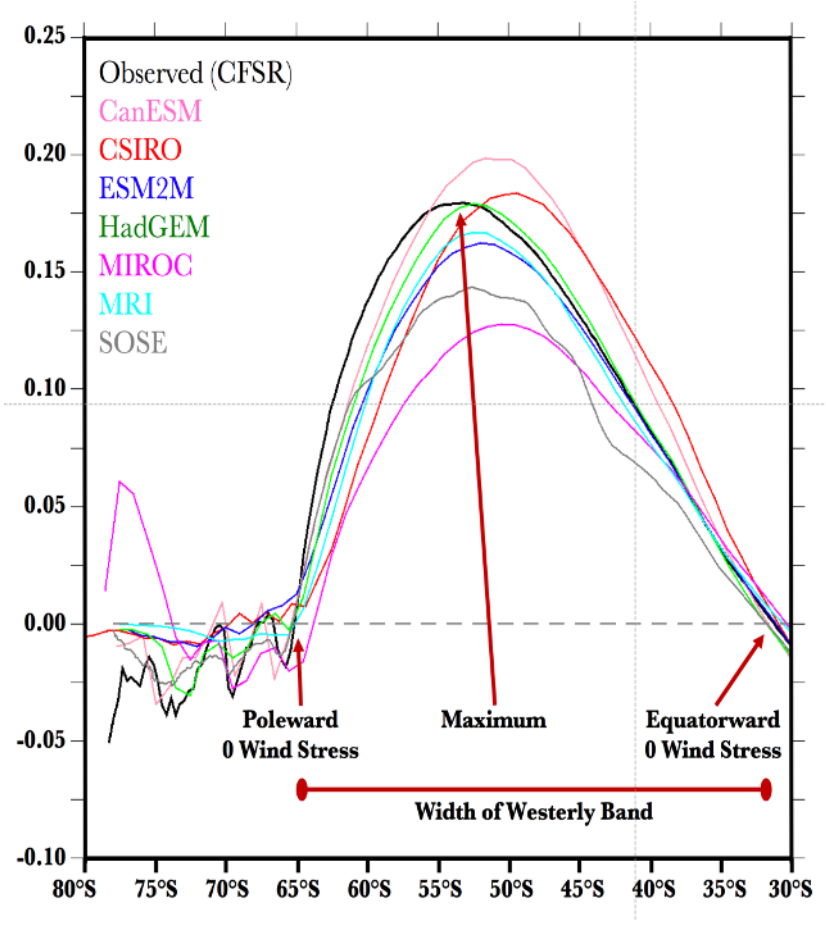

1245 **Figure 27. The zonal and annual means of the zonal wind stress (N/m2) for the reanalysis, six of the CMIP5 simulations and the BSOSE state estimate—note that each of the model simulations (colors) and B-SOSE (gray) have the peak wind stress equatorward of the observations (black). Also shown are the latitudes of the observed ‘‘poleward zero wind stress’’ and the ‘‘equatorward zero wind stress’’ which delineate the ‘‘width of the westerly band” that is highly correlated with total heat uptake by the Southern Ocean. Enhanced from figure produced by *recipe_russell18jgr.yml*. see Section 3.3.2. For further discussion of this figure, see the original in Russell et al. (2018).**

https://doi.org/10.5194/gmd-2019-291
Preprint. Discussion started: 26 November 2019
© Author(s) 2019. CC BY 4.0 License.

Geoscientific Model Development Discussions
Open Access
EGU

1250

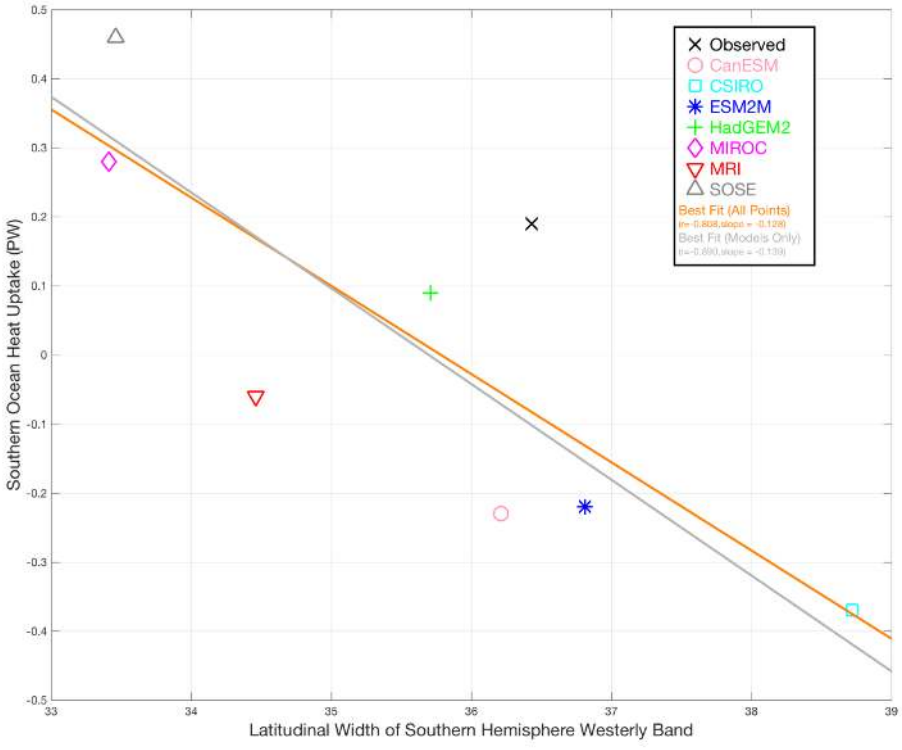

Figure 28. Scatter plot of the width of the Southern Hemisphere westerly wind band (in degrees of latitude) against the annual-mean integrated heat uptake south of 30°S (in PW—negative uptake is heat lost from the ocean), along with the ''best fit'' linear relationship for the models and observations shown. Enhanced from figure produced by *recipe_russell18jgr.yml*. see in Section 3.3.2. For further discussion of this figure, see the original in Russell et al. (2018). The calculation of the ''observed'' heat flux into the Southern Ocean is described in the text. The correlation is significant above the 98% level based on a simple t test.

1255

https://doi.org/10.5194/gmd-2019-291
Preprint. Discussion started: 26 November 2019
© Author(s) 2019. CC BY 4.0 License.

Geoscientific Model Development Discussions

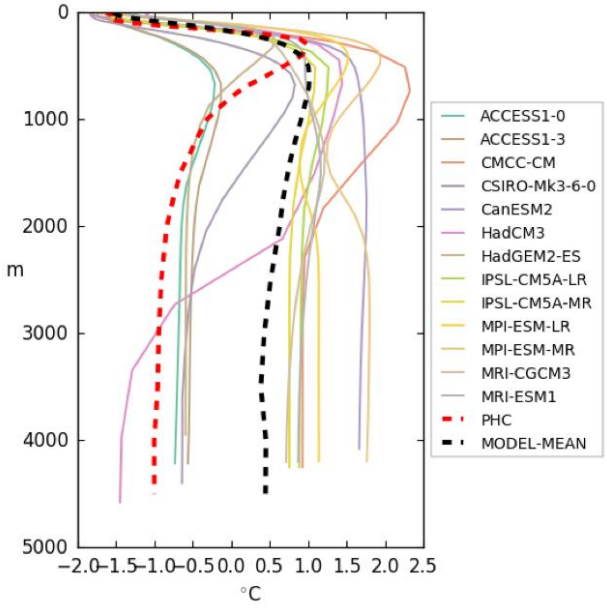

1260 **Figure 29. Mean (1970-2005) vertical potential temperature distribution in the Eurasian basin for CMIP5 coupled ocean models, PHC3 climatology (dotted red line) and multi-model mean (dotted black line). Models tend to overestimate temperature in the interior of the Arctic Ocean and have too deep Atlantic water depth. Similar to Figure 7 of Ilıcak, et al. 2016 and produced with recipe_arctic_ocean.yml , see details in Section 3.3.3.**

https://doi.org/10.5194/gmd-2019-291
Preprint. Discussion started: 26 November 2019
© Author(s) 2019. CC BY 4.0 License.

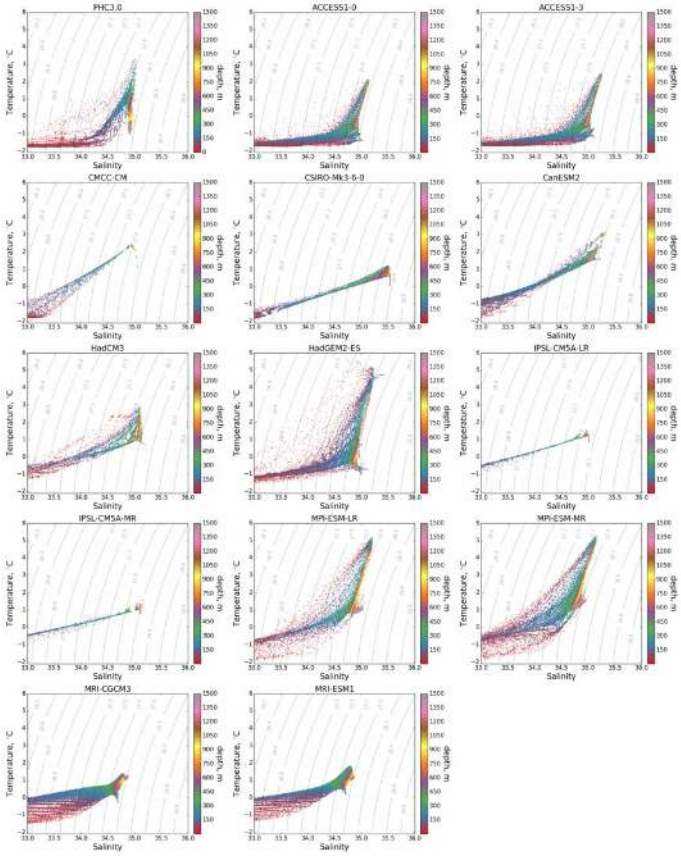

Figure 30. Mean (1970-2005) T-S diagrams for Eurasian Basin of the Arctic Ocean. PHC3.0 shows climatological values for selected CMIP5 models and PHC3.0 observations. Most models can't properly represent Arctic Ocean water masses and ether have wrong values for temperature and salinity or miss specific water masses completely. Produced with *recipe_arctic_ocean.yml* , see details in Section 3.3.3.

https://doi.org/10.5194/gmd-2019-291
Preprint. Discussion started: 26 November 2019
© Author(s) 2019. CC BY 4.0 License.

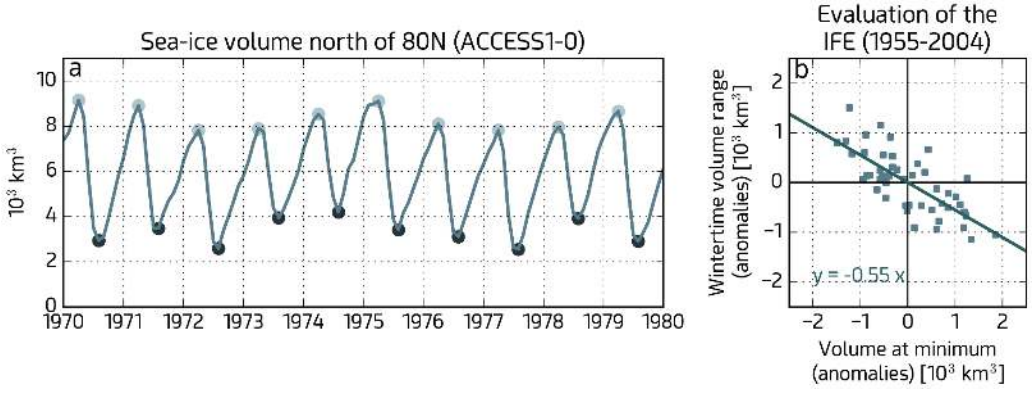

Figure 31. Quantitative evaluation of the Ice Formation Efficiency (IFE). (a) Example time series (1970-1979) of the monthly mean Arctic sea-ice volume north of 80°N of one CMIP5 model (ACCESS1-0), with its annual minimum and maximum values marked with the dark and light dots, respectively. (b) Estimation of the IFE, defined as the regression between anomalies of sea-ice volume produced during the growing season (difference between one annual maximum and the preceding minimum) and anomalies of the preceding minimum. A value IFE = -1 means that the late-summer ice volume anomaly is fully recovered during the following winter (strong negative feedback damping all anomalies) while a value IFE = 0 means that the wintertime volume production is essentially decoupled from the late-summer anomalies (inexistent feedback). Similar to Extended Data Figure 7a-b of Massonnet et al. (2018) and produced with *recipe_seaice_feedback.yml,* see details in Section 3.3.4.

https://doi.org/10.5194/gmd-2019-291
Preprint. Discussion started: 26 November 2019
© Author(s) 2019. CC BY 4.0 License.

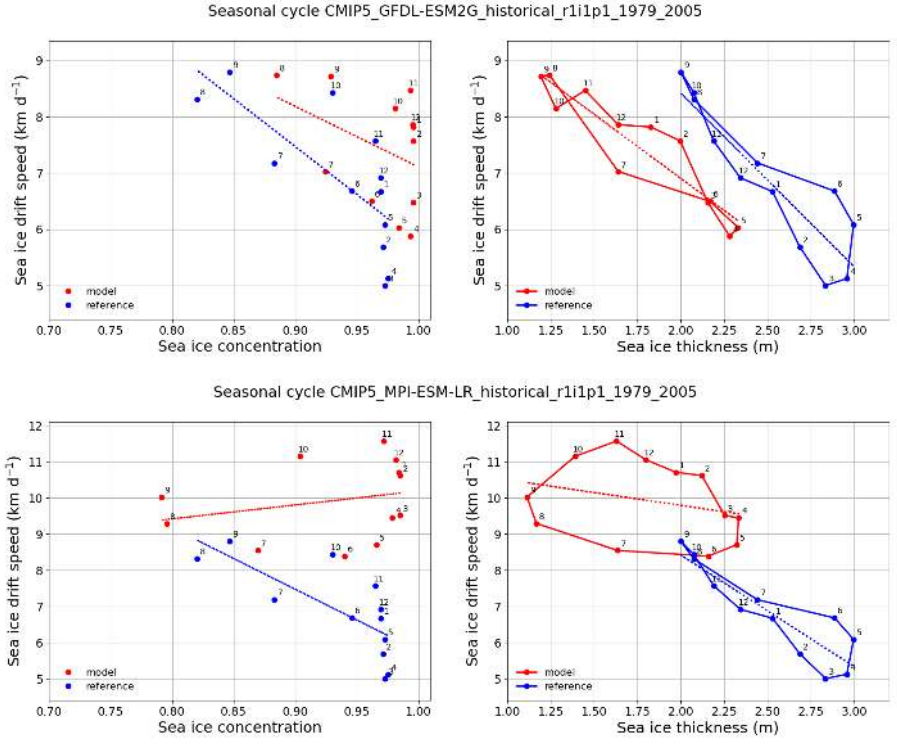

Figure 32. Scatter plots of modelled (red) and observed (blue) monthly mean sea-ice drift speed against sea-ice concentration (left panels) and sea-ice thickness (right panels) temporally averaged over the period 1979–2005 and spatially averaged over the SCICEX box. Top panels show results from the GDFL-ESM2G model and bottom panels show results from the MPI-ESM-LR model (CMIP5 historical runs). Observations/reanalysis are shown in all panels (IABP for drift speed, OSI-450 for concentration, and PIOMAS for thickness). Numbers denote months. Dotted lines show linear regressions. Results show that the GFDL-ESM2G model can reproduce the sea-ice drift speed - concentration/thickness relationships compared to observations, with higher drift speed with lower concentration/thickness, despite the too thin ice in the model, while the MPI-ESM-LR model cannot reproduce this result. This figure was produced in a similar way as Figure 4 of Docquier et al. (2017) with *recipe_sea_ice_drift.yml*, see details in Section 3.3.4.

https://doi.org/10.5194/gmd-2019-291
Preprint. Discussion started: 26 November 2019
© Author(s) 2019. CC BY 4.0 License.

Geoscientific Model Development Discussions
Open Access
EGU

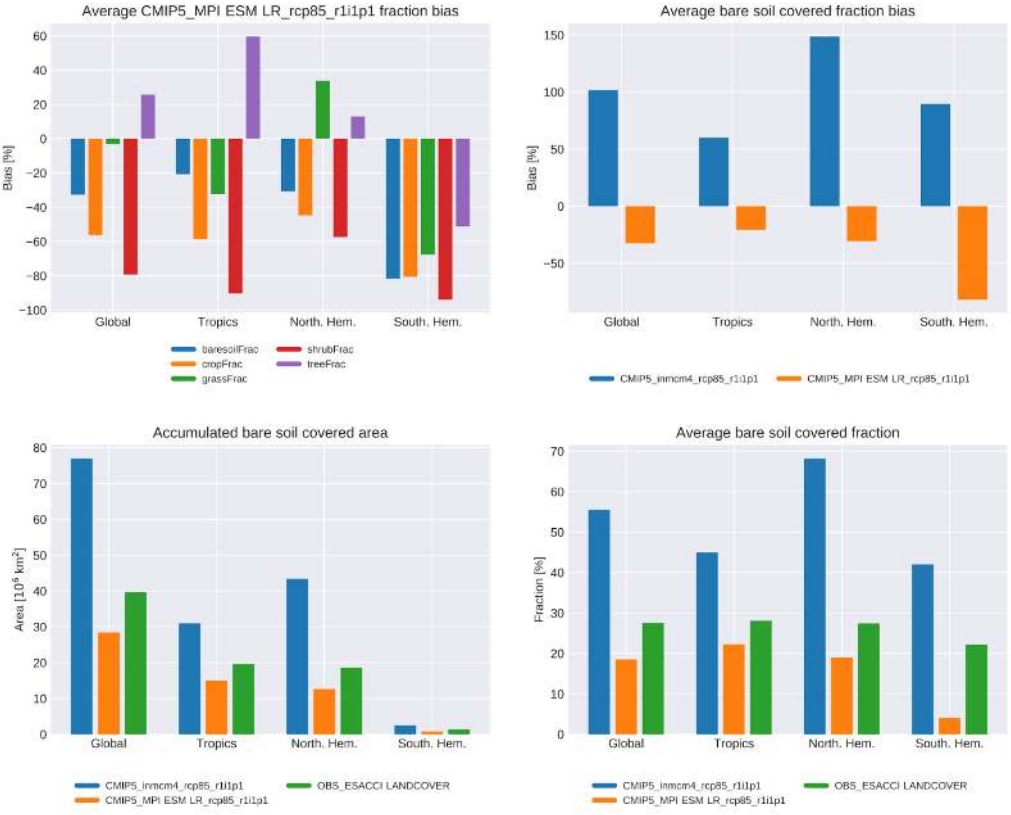

Figure 33. Panels show plots produced by the metric *recipe_landcover.yml* using model output from historical CMIP5 simulations (period 2008-2012) of the ESMs MPI-ESM and INMCM4 compared to land cover observations provided by ESA CCI for different regions. The upper two panels display the relative bias [%] between the models and the observations for either one model (i.e. MPI-ESM) and several land cover types (upper, left) or for one land cover type (i.e. bare soil fraction) and all selected models (upper, right). The lower plots display the accumulated area [10^6 km^2] (lower, left) as well as the average cover fraction [%] (lower, right) for a selected land cover type (bare soil fraction) and all selected models and observations for different. Thus, the landcover analysis provides a quick overview for major land cover types and the ability of different models to reproduce them. The metric is based on the analysis presented in Lauer et al. (2017) and Georgievski et al. (2018) and discussed in section 3.4.1.

https://doi.org/10.5194/gmd-2019-291
Preprint. Discussion started: 26 November 2019
© Author(s) 2019. CC BY 4.0 License.

Geoscientific Model Development
Discussions
Open Access
EGU

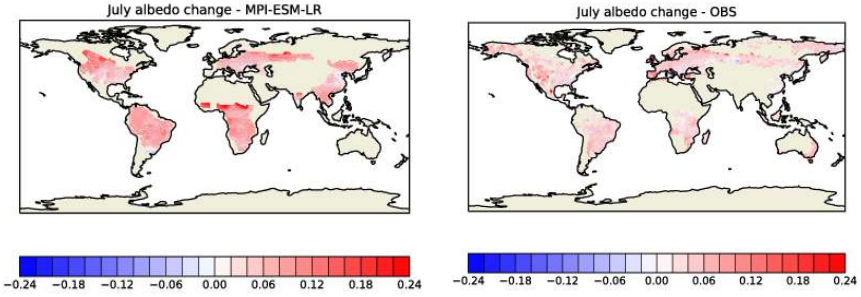

Figure 34. Albedo change due to a transition from landcover type 'tree' to 'crops and grasses' calculated through fitting, for each grid cell, a multiple linear regression model to the different land cover fractions (predictors) and albedo (predictant) within a window encompassing 5X5 grid cells centered over that grid cell of interest . Results are shown for (left) the MPI-ESM-LR model (2001-2005 July mean) and (right) the observational dataset from Duveiller et al. (2018) (2008-2012 July mean). July albedo difference between trees and crops or grasses is about at least twice as high in the MPI-ESM-LR model as in the observations, strongly suggesting that the simulated summer albedo increase from historical land cover changes is overestimated in this model. The results reveal that the July albedo difference between trees and crops or grasses is about at least twice as high in the MPI-ESM-LR model as in the observations, strongly suggesting that the simulated summer albedo increase from historical LCC is overestimated in this model. Produced with *recipe_landcoveralbedo.yml*, see details in Section 3.4.2.

https://doi.org/10.5194/gmd-2019-291
Preprint. Discussion started: 26 November 2019
© Author(s) 2019. CC BY 4.0 License.

Geoscientific Model Development
Discussions
Open Access
EGU

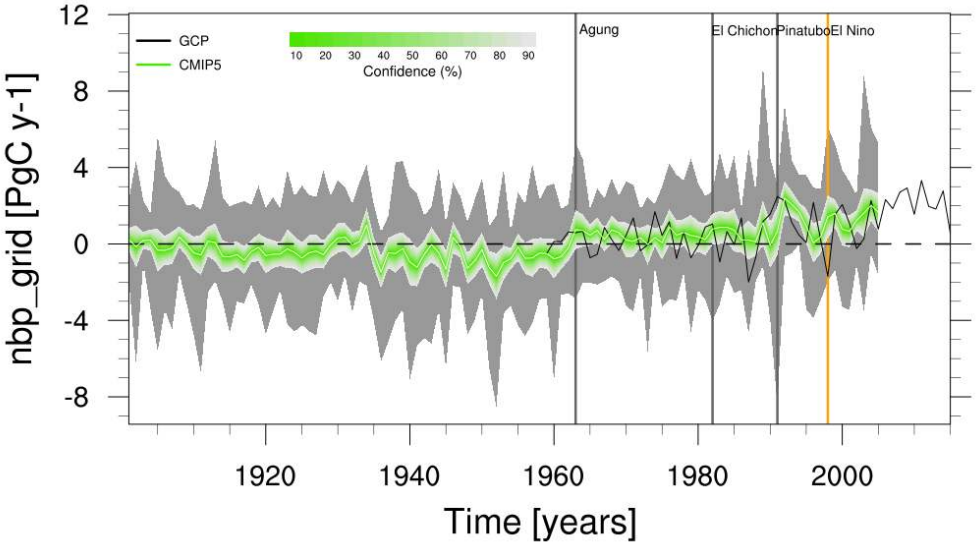

Figure 35. Timeseries plot of the global land-atmosphere CO_2 flux (*nbp*) for CMIP5 models compared to observational estimates by GCP, Le Quere et al. (2018)) (black line). Gray shading represents the range of the CMIP5 models, green shading shows the confidence interval evaluated from the CMIP5 ensemble standard deviation assuming a *t* distribution centered at the multi-model mean (white line). Vertical lines indicate volcanic eruptions (grey) and El Niño events (orange). As positive values correspond to a carbon uptake of the land, the plot shows a slight increase in the land carbon uptake over the whole period. Similar to Figure 5 of Anav et al. (2013) and produced with *recipe_anav13jclim.yml*, see details in Section 3.5.1.

https://doi.org/10.5194/gmd-2019-291
Preprint. Discussion started: 26 November 2019
© Author(s) 2019. CC BY 4.0 License.

Geoscientific Model Development Discussions
Open Access
EGU

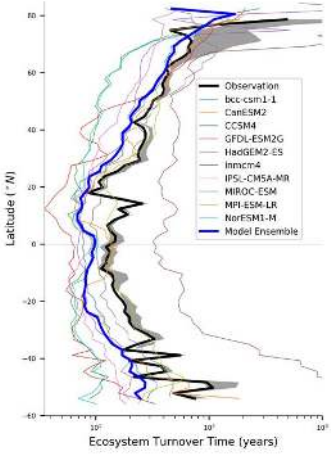

Figure 36. Zonal distribution of ecosystem turnover time of carbon (in years). The zonal values are calculated as the ratio of total carbon stock and the gross primary productivity per latitude. The individual models are plotted in coloured thin lines, the multimodel ensemble in thick blue line, and the observation-based estimate (Carvalhais et al., 2014) in thick black line with shaded region showing the observational uncertainty. The median of all models is adopted as the multimodel ensemble. Note the logarithmic horizontal axis. The models follow the gradient of increasing turnover times of carbon from tropics to higher latitudes, much related to temperature decreases, as observed in observations. However, for most of the latitudinal bands, with the exception of one model, most simulations reveal turnover times that are faster than the observations. Produced with *recipe_carvalhais2014nat.yml*, see details in Section 3.5.2.

https://doi.org/10.5194/gmd-2019-291
Preprint. Discussion started: 26 November 2019
© Author(s) 2019. CC BY 4.0 License.

Geoscientific Model Development Discussions
Open Access
EGU

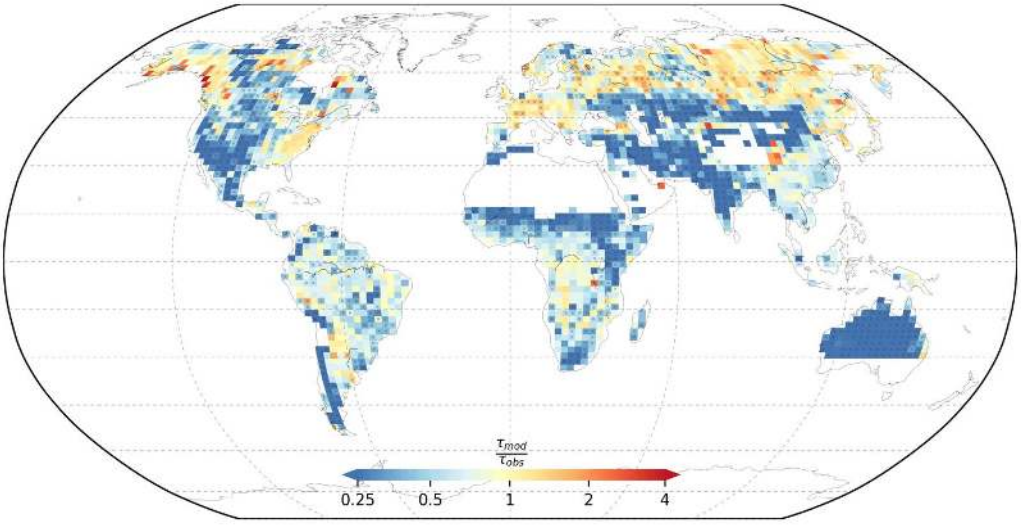

Figure 37. Global distribution of the biases in the multi-model ensemble ecosystem turnover time of carbon (years) and the multi-model agreement in CMIP5 models. The bias is calculated as the ratio between multi-model ensemble and observation-based estimate (Carvalhais et al., 2014). The stippling indicates the regions where only two or fewer models (out of 10) are within the range of observational uncertainties (5th and 95th percentiles). A generalized underestimation of turnover times of carbon is apparently dominant in water limited regions. In most of these regions most models show estimates outside of the observational uncertainties (stippling). These results challenge the combined effects of water and temperature limitations on turnover times of carbon and suggest the need for improvement on the description of the water cycle in terrestrial ecosystems. Produced with *recipe_carvalhais2014nat.yml*, see details in Section 3.5.2.

https://doi.org/10.5194/gmd-2019-291
Preprint. Discussion started: 26 November 2019
© Author(s) 2019. CC BY 4.0 License.

Geoscientific Model Development Discussions
Open Access
EGU

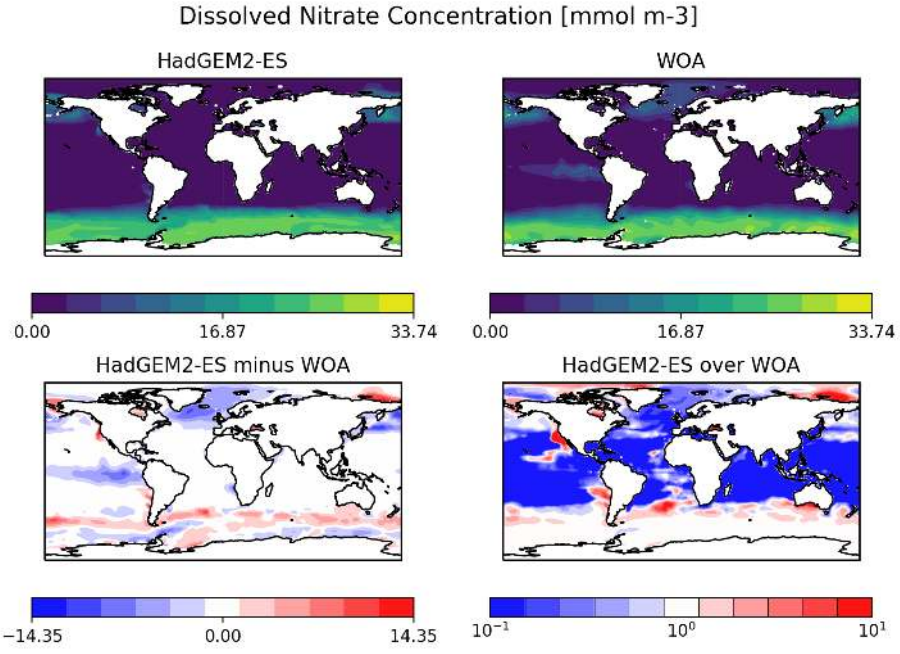

1350

Figure 38. The surface dissolved nitrate concentration in the CMIP5 HadGEM2-ES model compared against the World Ocean Atlas 2013 nitrate. The top two figures show the surface fields, the bottom two show the difference and the quotient between the two datasets. This figure highlights that the HadGEM2-ES model is proficient at reproducing the surface nitrate concentration in the Atlantic ocean, and in mid latitudes, but may struggle to
1355 **reproduce observations at high latitudes. Produced with *recipe_ocean_bgc.yml*, see details in Section 3.5.3.**

https://doi.org/10.5194/gmd-2019-291
Preprint. Discussion started: 26 November 2019
© Author(s) 2019. CC BY 4.0 License.

Geoscientific Model Development Discussions

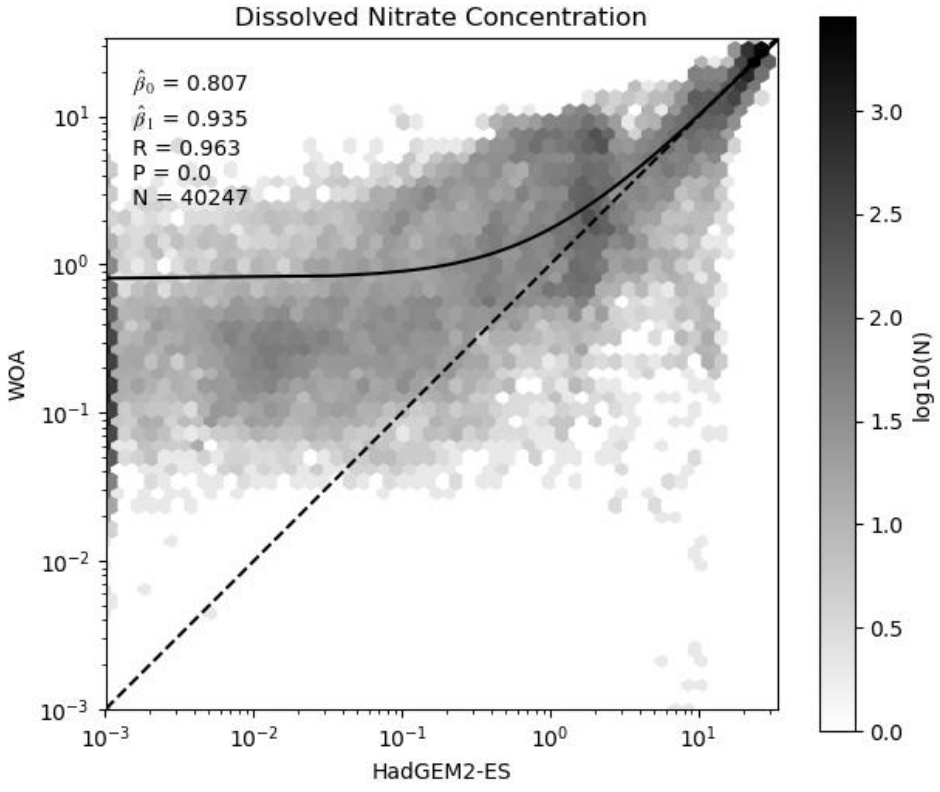

Figure 39. The surface dissolved nitrate concentration in the CMIP5 HadGEM2-ES model compared against the World Ocean Atlas 2013 nitrate. This figure shows the paired model and observational datasets. A linear regression line of best fit is shown as a black line. A dashed line indicates the 1:1 line. The result of a linear regression are shown in the top left corner of the figure, where $\hat{\beta}_0$is the intersect, β_1 is the slope, R is the correlation, P is the P value, and N is the number of data point pairs As both the fitted slope and the correlation coefficient are near one, the HadGEM2-ES simulation excelled at reproducing the observed values of the surface nitrate concentration. Produced with *recipe_ocean_bgc.yml*, see details in Section 3.5.3.

https://doi.org/10.5194/gmd-2019-291
Preprint. Discussion started: 26 November 2019
© Author(s) 2019. CC BY 4.0 License.

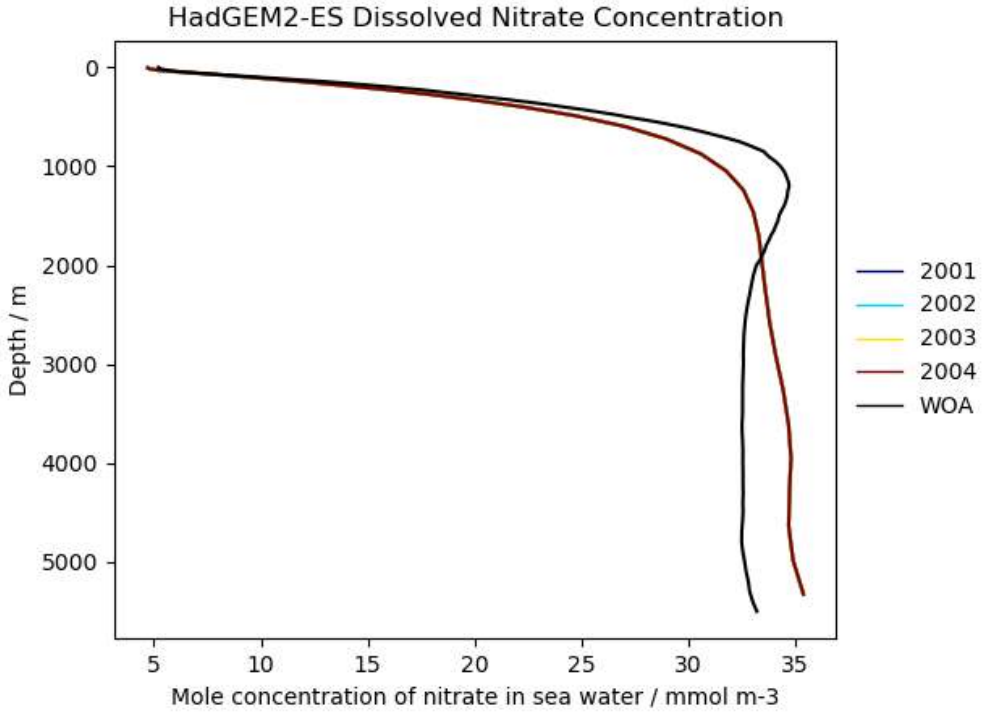

1370 **Figure 40. The global area-weighted average depth profile of the dissolved nitrate concentration in the CMIP5 HadGEM2-ES model and against the World Ocean Atlas 2013. This figure shows that while the model and the observations both show a similar overall depth structure, the model is not able to produce the observed maximum nitrate concentration at approximately 1000 m depth and overestimates the nitrate concentration deeper in the water column. Produced with *recipe_ocean_bgc.yml*, see details in Section 3.5.3.**

https://doi.org/10.5194/gmd-2019-291
Preprint. Discussion started: 26 November 2019
© Author(s) 2019. CC BY 4.0 License.

Geoscientific Model Development Discussions
Open Access
EGU

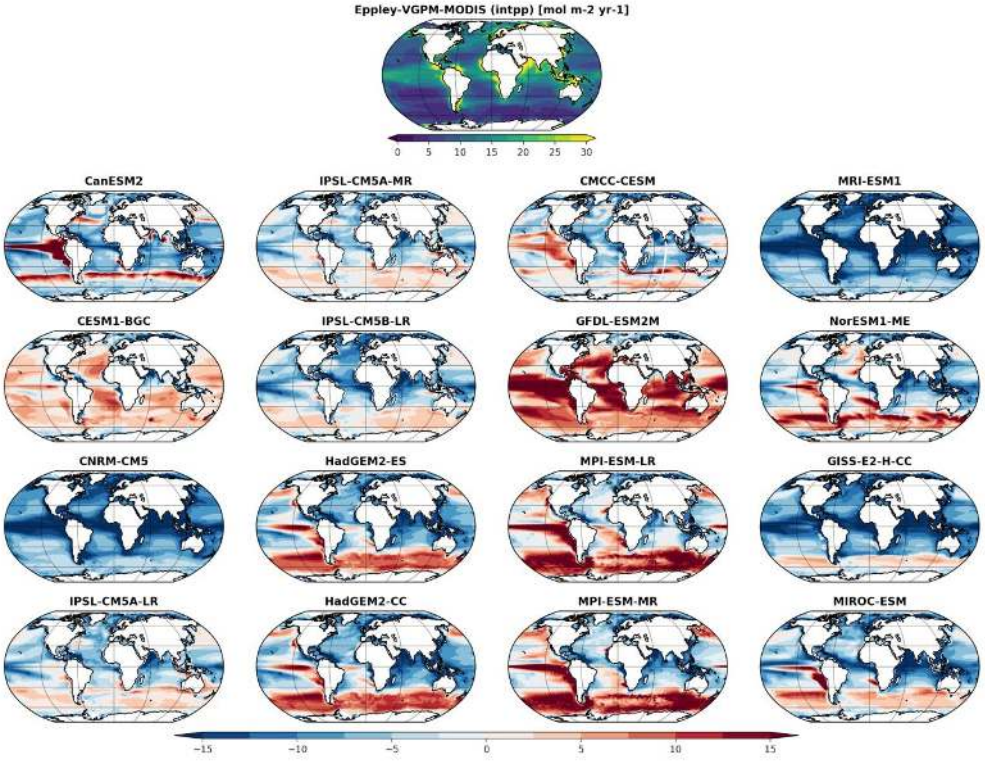

Figure 41. Global maps of marine Primary Production as carbon (mol m-2 yr-1) estimated from MODIS satellite data using Eppley-VGPM algorithm (Top panel) and differences computed for 16 CMIP5 models data averaged over the period 1995-2004. Systematic biases characterize all models mainly in the equatorial Pacific and Antarctic regions, in some cases with opposite sign, and coastal ocean productivity is generally underestimated with major deviations in the equatorial zone. See Section 3.5.3 for details on *recipe_ocean_bgc.yml*.

https://doi.org/10.5194/gmd-2019-291
Preprint. Discussion started: 26 November 2019
© Author(s) 2019. CC BY 4.0 License.

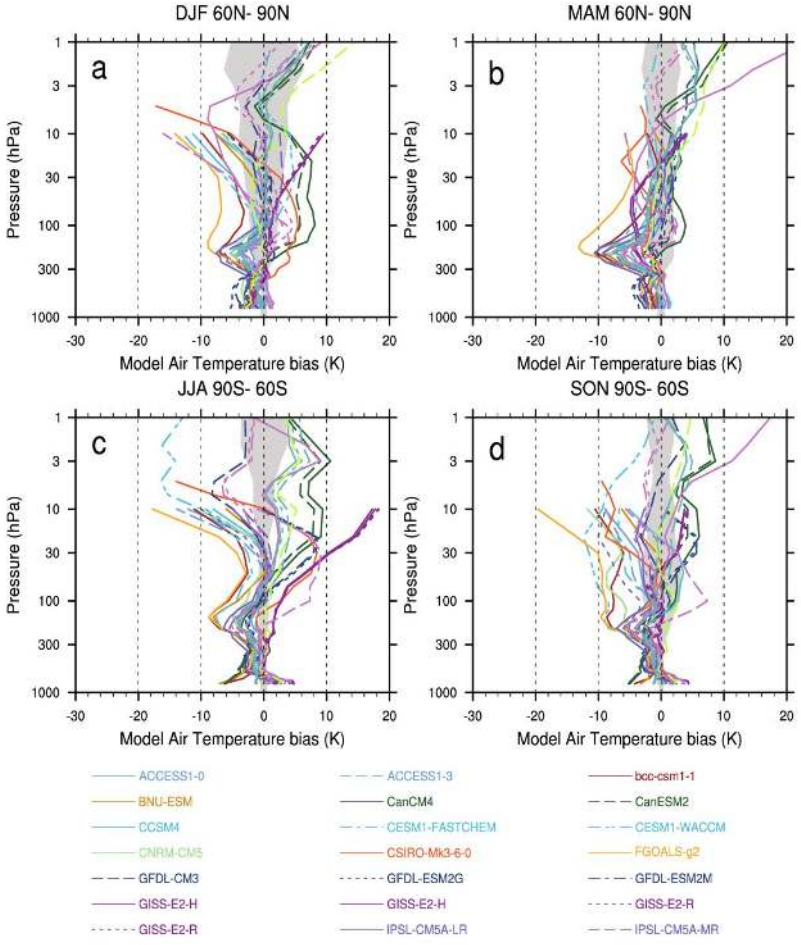

Figure 42. Climatological mean temperature biases for (top) 60–90N and (bottom) 60–90S for the (left) winter and (right) spring seasons. The climatological means for the CCMs and NCEP data from 1980 to 1999 and for UKMO from 1992 to 2001 are included. Biases are calculated relative to ERA-40 reanalyses. The grey area shows ERA-40 plus and minus 1 standard deviation about the climatological mean. High-latitude temperatures in winter and spring are particularly important for correctly modelling PSC induced polar ozone depletion. In the middle stratosphere there are large variations between the analyses and most models, with no clear bias direction, whereas the temperature bias in the troposphere between analyses and models is somewhat smaller, but is in most models negative around 200hPa. The upper stratosphere is only available for a few models, and while for most shown seasons the agreement is relatively good, the spread between analyses and models is very large for the Antarctic polar regions in JJA. Similar to Figure 1 of Eyring et al. (2006), produced with the *recipe_eyring06jgr.yml.* See details in Section 3.5.4.

https://doi.org/10.5194/gmd-2019-291
Preprint. Discussion started: 26 November 2019
© Author(s) 2019. CC BY 4.0 License.

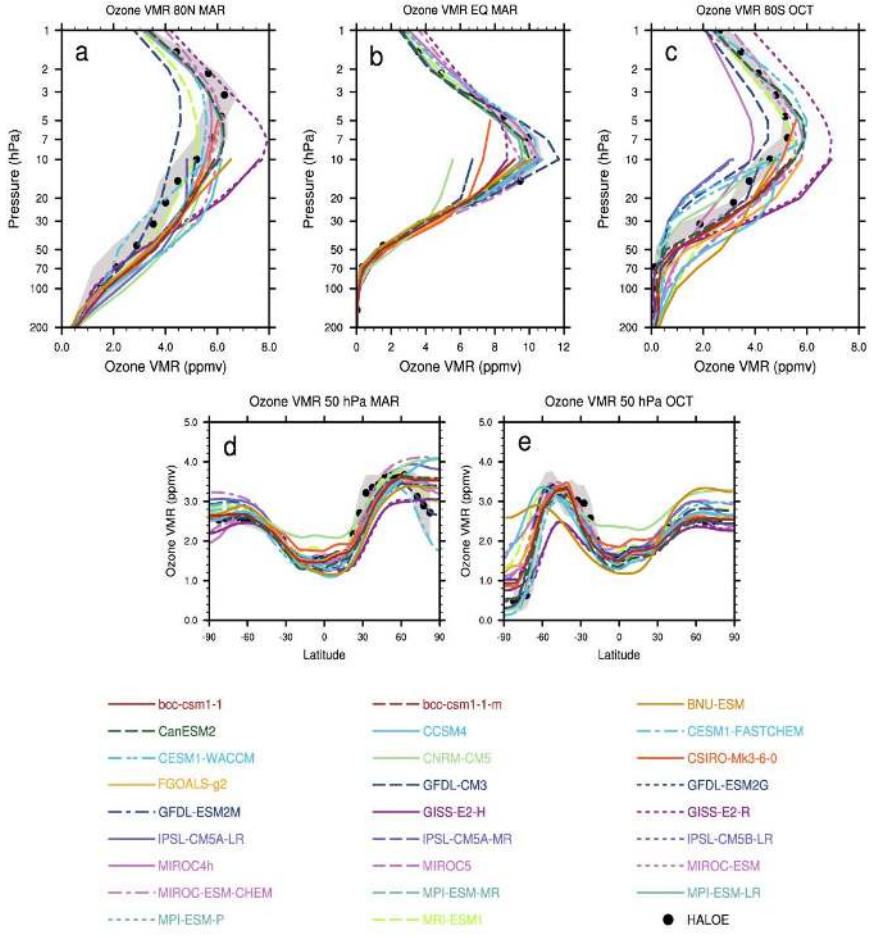

Figure 43. Climatological zonal mean ozone mixing ratios from the CMIP5 simulations and HALOE in ppmv. Vertical profiles at (a) 80N in March, (b) 0 in March, and (c) 80S in October. Latitudinal profiles at 50 hPa in (d) March and (e) October. The grey area shows HALOE plus and minus 1 standard deviation (s) about the climatological zonal mean. Ozone is clearly overestimated by most models, compared to the observations, in the Northern high latitudes between 50 hPa and 10 hPa, which becomes also apparent in the climatological zonal mean at 50 hPa. Southern high latitudes are slightly better represented in the models at 50 hPa with a more general spread around the observations, but at lower pressure levels an overestimation of ozone compared to the observations becomes apparent in some models. Similar to Figure 5 of Eyring et al. (2006), produced with the *recipe_eyring06jgr.yml.* See details in Section 3.5.4.

https://doi.org/10.5194/gmd-2019-291
Preprint. Discussion started: 26 November 2019
© Author(s) 2019. CC BY 4.0 License.

Geoscientific Model Development Discussions
Open Access
EGU

References

Achard, F., Beuchle, R., Mayaux, P., Stibig, H.J., Bodart, C., Brink, A., Carboni, S., Desclée, B., Donnay, F. and Eva, H.D., 2014. Determination of tropical deforestation rates and related carbon losses from 1990 to 2010. Global change biology, 20(8): 2540-2554.

Adler, R.F., Huffman, G.J., Chang, A., Ferraro, R., Xie, P.-P., Janowiak, J., Rudolf, B., Schneider, U., Curtis, S. and Bolvin, D., 2003. The version-2 global precipitation climatology project (GPCP) monthly precipitation analysis (1979–present). Journal of hydrometeorology, 4(6): 1147-1167.

Alkama, R. and Cescatti, A., 2016. Biophysical climate impacts of recent changes in global forest cover. Science, 351(6273): 600-604.

Ambaum, M.H., 2010. Thermal physics of the atmosphere, 1. John Wiley & Sons.

Anav, A., Friedlingstein, P., Kidston, M., Bopp, L., Ciais, P., Cox, P., Jones, C., Jung, M., Myneni, R. and Zhu, Z., 2013. Evaluating the Land and Ocean Components of the Global Carbon Cycle in the CMIP5 Earth System Models. Journal of Climate, 26(18): 6801-6843.

Arora, V.K., Boer, G.J., Friedlingstein, P., Eby, M., Jones, C.D., Christian, J.R., Bonan, G., Bopp, L., Brovkin, V. and Cadule, P.J.J.o.C., 2013. Carbon–concentration and carbon–climate feedbacks in CMIP5 Earth system models. 26(15): 5289-5314.

Balaji, V., Taylor, K.E., Juckes, M., Lautenschlager, M., Blanton, C., Cinquini, L., Denvil, S., Durack, P.J., Elkington, M., Guglielmo, F., Guilyardi, E., Hassell, D., Kharin, S., Kindermann, S., Lawrence, B.N., Nikonov, S., Radhakrishnan, A., Stockhause, M., Weigel, T. and Williams, D., 2018. Requirements for a global data infrastructure in support of CMIP6. Geosci. Model Dev. Discuss., in review: 1-28.

Baldwin, M.P. and Dunkerton, T.J.J.S., 2001. Stratospheric harbingers of anomalous weather regimes. 294(5542): 581-584.

Baldwin, M.P. and Thompson, D.W.J., 2009. A critical comparison of stratosphere–troposphere coupling indices. Quarterly Journal of the Royal Meteorological Society, 135(644): 1661-1672.

Barriopedro, D., García-Herrera, R. and Trigo, R.M., 2010. Application of blocking diagnosis methods to general circulation models. Part I: A novel detection scheme. Climate dynamics, 35(7-8): 1373-1391.

Behrenfeld, M.J., Falkowski, P.G.J.L. and oceanography, 1997. Photosynthetic rates derived from satellite-based chlorophyll concentration. 42(1): 1-20.

Bengtsson, L. and Hodges, K.I., 2019. Can an ensemble climate simulation be used to separate climate change signals from internal unforced variability? Climate Dynamics, 52(5): 3553-3573.

Boisier, J., de Noblet-Ducoudré, N., Pitman, A., Cruz, F., Delire, C., Van den Hurk, B., Van der Molen, M., Müller, C. and Voldoire, A.J.J.o.G.R.A., 2012. Attributing the impacts of land-cover changes in temperate regions on surface temperature and heat fluxes to specific causes: Results from the first LUCID set of simulations. 117(D12).

Bonan, G.B.J.s., 2008. Forests and climate change: forcings, feedbacks, and the climate benefits of forests. 320(5882): 1444-1449.

Brovkin, V., Boysen, L., Raddatz, T., Gayler, V., Loew, A. and Claussen, M.J.J.o.A.i.M.E.S., 2013. Evaluation of vegetation cover and land-surface albedo in MPI-ESM CMIP5 simulations. 5(1): 48-57.

Buitenhuis, E.T., Hashioka, T. and Le Quéré, C.J.G.B.C., 2013. Combined constraints on global ocean primary production using observations and models. 27(3): 847-858.

Carvalhais, N., Forkel, M., Khomik, M., Bellarby, J., Jung, M., Migliavacca, M., Mu, M., Saatchi, S., Santoro, M., Thurner, M., Weber, U., Ahrens, B., Beer, C., Cescatti, A., Randerson, J.T. and Reichstein, M., 2014. Global covariation of carbon turnover times with climate in terrestrial ecosystems. Nature, 514(7521): 213-7.

Cassou, C., Terray, L. and Phillips, A.S., 2005. Tropical Atlantic influence on European heat waves. Journal of Climate, 18(15): 2805-2811.

Change, I.C.J.T.i.n.c.r.f.t.r., 2013. The Physical Science Basis. Contribution of Working Group I to the Fifth Assessment Report of the Intergovernmental Panel on Climate Change. 2013. 33-118.

Charlton-Perez, A.J., Baldwin, M.P., Birner, T., Black, R.X., Butler, A.H., Calvo, N., Davis, N.A., Gerber, E.P., Gillett, N. and Hardiman, S.J.J.o.G.R.A., 2013. On the lack of stratospheric dynamical variability in low-top versions of the CMIP5 models. 118(6): 2494-2505.

Cheng, W., Chiang, J.C. and Zhang, D.J.J.o.C., 2013. Atlantic meridional overturning circulation (AMOC) in CMIP5 models: RCP and historical simulations. 26(18): 7187-7197.

Coumou, D. and Rahmstorf, S., 2012. A decade of weather extremes. Nature climate change, 2(7): 491.

Cox, P.M., Pearson, D., Booth, B.B., Friedlingstein, P., Huntingford, C., Jones, C.D. and Luke, C.M., 2013. Sensitivity of tropical carbon to climate change constrained by carbon dioxide variability. Nature, 494(7437): 341-344.

Danabasoglu, G., Bates, S.C., Briegleb, B.P., Jayne, S.R., Jochum, M., Large, W.G., Peacock, S. and Yeager, S.G., 2012. The CCSM4 ocean component. Journal of Climate, 25(5): 1361-1389.

https://doi.org/10.5194/gmd-2019-291
Preprint. Discussion started: 26 November 2019
© Author(s) 2019. CC BY 4.0 License.

Davin, E.L., Rechid, D., Breil, M., Cardoso, R.M., Coppola, E., Hoffmann, P., Jach, L.L., Katragkou, E., de Noblet-Ducoudré, N. and Radtke, K.J.E.S.D.D., 2019. Biogeophysical impacts of forestation in Europe: first results from the LUCAS Regional Climate Model intercomparison. 2019: 1-31.

Davini, P., 2018. MiLES - Mid Latitude Evaluation System (Version v0.51). Zenodo, http://doi.org/10.5281/zenodo.1237838.

Davini, P., Cagnazzo, C., Gualdi, S. and Navarra, A., 2012. Bidimensional diagnostics, variability, and trends of Northern Hemisphere blocking. Journal of Climate, 25(19): 6496-6509.

Davini, P. and D'Andrea, F., 2016. Northern Hemisphere atmospheric blocking representation in global climate models: Twenty years of improvements? Journal of Climate, 29(24): 8823-8840.

Dawson, A., Palmer, T. and Corti, S.J.G.R.L., 2012. Simulating regime structures in weather and climate prediction models. 39(21).

De Mora, L., Butenschon, M. and Allen, J.J.G.M.D., 2013. How should sparse marine in situ measurements be compared to a continuous model: an example. 6(2): 533-548.

de Noblet-Ducoudré, N., Boisier, J.-P., Pitman, A., Bonan, G., Brovkin, V., Cruz, F., Delire, C., Gayler, V., Van den Hurk, B. and Lawrence, P.J.J.o.C., 2012. Determining robust impacts of land-use-induced land cover changes on surface climate over North America and Eurasia: results from the first set of LUCID experiments. 25(9): 3261-3281.

Defourny, P., Boettcher, M., Bontemps, S., Kirches, G., Krueger, O., Lamarche, C., Lembrée, C., Radoux, J. and Verheggen, A., 2014. Algorithm theoretical basis document for land cover climate change initiative. Technical report, European Space Agency.

Defourny, P., Boettcher, M., Bontemps, S., Kirches, G., Lamarche, C., Peters, M., Santoro, M. and Schlerf, M., 2016. Land cover cci Product user guide version 2. . Technical report, European Space Agency.

Deser, C., Alexander, M.A., Xie, S.P. and Phillips, A.S., 2010. Sea Surface Temperature Variability: Patterns and Mechanisms. Annual Review of Marine Science, 2: 115-143.

Deser, C., Knutti, R., Solomon, S. and Phillips, A.S., 2012. Communication of the role of natural variability in future North American climate. Nature Climate Change, 2(11): 775.

Deser, C., Phillips, A.S., Alexander, M.A. and Smoliak, B.V., 2014. Projecting North American Climate over the Next 50 Years: Uncertainty due to Internal Variability*. Journal of Climate, 27(6): 2271-2296.

Deser, C., Simpson, I.R., McKinnon, K.A. and Phillips, A.S., 2017. The Northern Hemisphere extratropical atmospheric circulation response to ENSO: How well do we know it and how do we evaluate models accordingly? Journal of Climate, 30(13): 5059-5082.

Di Biagio, V., Calmanti, S., Dell'Aquila, A. and Ruti, P.M.J.G.R.L., 2014. Northern Hemisphere winter midlatitude atmospheric variability in CMIP5 models. 41(4): 1277-1282.

Docquier, D., Massonnet, F., Tandon, N.F., Lecomte, O. and Fichefet, T.J.T.C., 2017. Relationships between Arctic sea ice drift and strength modelled by NEMO-LIM3. 6. 11: 2829-2846.

Donohue, K., Tracey, K., Watts, D., Chidichimo, M.P. and Chereskin, T.J.G.R.L., 2016. Mean antarctic circumpolar current transport measured in drake passage. 43(22): 11,760-11,767.

Duveiller, G., Hooker, J. and Cescatti, A., 2018a. A dataset mapping the potential biophysical effects of vegetation cover change. Scientific Data, 5: 180014.

Duveiller, G., Hooker, J. and Cescatti, A., 2018b. The mark of vegetation change on Earth's surface energy balance. Nature communications, 9(1): 679.

Ellison, D., N. Futter, M. and Bishop, K.J.G.C.B., 2012. On the forest cover–water yield debate: from demand-to supply-side thinking. 18(3): 806-820.

Exarchou, E., Kuhlbrodt, T., Gregory, J.M. and Smith, R.S.J.J.o.C., 2015. Ocean heat uptake processes: a model intercomparison. 28(2): 887-908.

Eyring, V., Bony, S., Meehl, G.A., Senior, C.A., Stevens, B., Stouffer, R.J. and Taylor, K.E., 2016a. Overview of the Coupled Model Intercomparison Project Phase 6 (CMIP6) experimental design and organization. Geosci. Model Dev., 9(5): 1937-1958.

Eyring, V., Butchart, N., Waugh, D., Akiyoshi, H., Austin, J., Bekki, S., Bodeker, G., Boville, B., Brühl, C. and Chipperfield, M., 2006. Assessment of temperature, trace species, and ozone in chemistry-climate model simulations of the recent past. Journal of Geophysical Research: Atmospheres, 111(D22).

Eyring, V., Gleckler, P.J., Heinze, C., Stouffer, R.J., Taylor, K.E., Balaji, V., Guilyardi, E., Joussaume, S., Kindermann, S., Lawrence, B.N., Meehl, G.A., Righi, M. and Williams, D.N., 2016b. Towards improved and more routine Earth system model evaluation in CMIP. Earth Syst. Dynam., 7(4): 813-830.

Eyring, V., Harris, N., Rex, M., Shepherd, T.G., Fahey, D., Amanatidis, G., Austin, J., Chipperfield, M., Dameris, M. and Forster, P.D.F.J.B.o.t.A.M.S., 2005. A strategy for process-oriented validation of coupled chemistry–climate models. 86(8): 1117-1134.

Eyring, V., Righi, M., Lauer, A., Evaldsson, M., Wenzel, S., Jones, C., Anav, A., Andrews, O., Cionni, I., Davin, E.L., Deser, C., Ehbrecht, C., Friedlingstein, P., Gleckler, P., Gottschaldt, K.D., Hagemann, S., Juckes, M., Kindermann, S., Krasting, J., Kunert, D., Levine, R., Loew, A., Mäkelä, J., Martin, G., Mason, E.,

https://doi.org/10.5194/gmd-2019-291
Preprint. Discussion started: 26 November 2019
© Author(s) 2019. CC BY 4.0 License.

Phillips, A.S., Read, S., Rio, C., Roehrig, R., Senftleben, D., Sterl, A., van Ulft, L.H., Walton, J., Wang, S. and Williams, K.D., 2016c. ESMValTool (v1.0) – a community diagnostic and performance metrics tool for routine evaluation of Earth system models in CMIP. Geosci. Model Dev., 9(5): 1747-1802.

Ferranti, L., Corti, S. and Janousek, M., 2015. Flow-dependent verification of the ECMWF ensemble over the Euro-Atlantic sector. Quarterly Journal of the Royal Meteorological Society, 141(688): 916-924.

Ferraro, R., Waliser, D.E., Gleckler, P., Taylor, K.E. and Eyring, V., 2015. Evolving Obs4MIPs to Support Phase 6 of the Coupled Model Intercomparison Project (CMIP6). Bulletin of the American Meteorological Society, 96(8): ES131-ES133.

Field, C.B., Behrenfeld, M.J., Randerson, J.T. and Falkowski, P., 1998. Primary Production of the Biosphere: Integrating Terrestrial and Oceanic Components. Science, 281(5374): 237-240.

Flato, G., Marotzke, J., Abiodun, B., Braconnot, P., Chou, S.C., Collins, W., Cox, P., Driouech, F., Emori, S., Eyring, V., Forest, C., Gleckler, P., Guilyardi, E., Jakob, C., Kattsov, V., Reason, C. and Rummukainen, M., 2013. Evaluation of Climate Models. In: T.F. Stocker, D. Qin, G.-K. Plattner, M. Tignor, S.K. Allen, J. Boschung, A. Nauels, Y. Xia, V. Bex and P.M. Midgley (Editor), Climate Change 2013: The Physical Science Basis. Contribution of Working Group I to the Fifth Assessment Report of the Intergovernmental Panel on Climate Change. Cambridge University Press, Cambridge, United Kingdom and New York, NY, USA, pp. 741–866.

Fraedrich, K., Lunkeit, F.J.T.A.D.M. and Oceanography, 2008. Diagnosing the entropy budget of a climate model. 60(5): 921-931.

Frankignoul, C., Gastineau, G. and Kwon, Y.-O., 2017. Estimation of the SST response to anthropogenic and external forcing and its impact on the Atlantic Multidecadal Oscillation and the Pacific Decadal Oscillation. Journal of Climate, 30(24): 9871-9895.

Friedlingstein, P., Cox, P., Betts, R., Bopp, L., von Bloh, W., Brovkin, V., Cadule, P., Doney, S., Eby, M., Fung, I., Bala, G., John, J., Jones, C., Joos, F., Kato, T., Kawamiya, M., Knorr, W., Lindsay, K., Matthews, H.D., Raddatz, T., Rayner, P., Reick, C., Roeckner, E., Schnitzler, K.-G., Schnur, R., Strassmann, K., Weaver, A.J., Yoshikawa, C. and Zeng, N., 2006. Climate–Carbon Cycle Feedback Analysis: Results from the C4MIP Model Intercomparison. Journal of Climate, 19(14): 3337-3353.

Friedlingstein, P., Meinshausen, M., Arora, V.K., Jones, C.D., Anav, A., Liddicoat, S.K. and Knutti, R., 2014. Uncertainties in CMIP5 Climate Projections due to Carbon Cycle Feedbacks. Journal of Climate, 27(2): 511-526.

Friend, A.D., Lucht, W., Rademacher, T.T., Keribin, R., Betts, R., Cadule, P., Ciais, P., Clark, D.B., Dankers, R., Falloon, P.D., Ito, A., Kahana, R., Kleidon, A., Lomas, M.R., Nishina, K., Ostberg, S., Pavlick, R., Peylin, P., Schaphoff, S., Vuichard, N., Warszawski, L., Wiltshire, A. and Woodward, F.I., 2014. Carbon residence time dominates uncertainty in terrestrial vegetation responses to future climate and atmospheric CO2. Proc Natl Acad Sci U S A, 111(9): 3280-5.

Garcia, H.E., Locarnini, R.A., Boyer, T.P., Antonov, J.I., Baranova, O.K., Zweng, M.M., Reagan, J.R., Johnson, D.R., Mishonov, A.V. and Levitus, S., 2013. World ocean atlas 2013. Volume 4, Dissolved inorganic nutrients (phosphate, nitrate, silicate).

Gassmann, A. and Herzog, H.J.J.Q.J.o.t.R.M.S., 2015. How is local material entropy production represented in a numerical model? , 141(688): 854-869.

Georgievski, G. and Hagemann, S., 2018. Characterizing uncertainties in the ESA-CCI land cover map of the epoch 2010 and their impacts on MPI-ESM climate simulations. Theoretical and Applied Climatology: 1-17.

Gerber, E.P., Baldwin, M.P., Akiyoshi, H., Austin, J., Bekki, S., Braesicke, P., Butchart, N., Chipperfield, M., Dameris, M. and Dhomse, S.J.J.o.G.R.A., 2010. Stratosphere-troposphere coupling and annular mode variability in chemistry-climate models. 115(D3).

Gettelman, A., Eyring, V., Fischer, C., Shiona, H., Cionni, I., Neish, M., Morgenstern, O., Wood, S.W. and Li, Z., 2012. A community diagnostic tool for chemistry climate model validation. Geoscientific Model Development, 5(5): 1061-1073.

Goody, R.J.Q.J.o.t.R.M.S., 2000. Sources and sinks of climate entropy. 126(566): 1953-1970.

Goosse, H., Kay, J.E., Armour, K.C., Bodas-Salcedo, A., Chepfer, H., Docquier, D., Jonko, A., Kushner, P.J., Lecomte, O. and Massonnet, F.J.N.c., 2018. Quantifying climate feedbacks in polar regions. 9(1): 1919.

Grams, C.M., Beerli, R., Pfenninger, S., Staffell, I. and Wernli, H.J.N.c.c., 2017. Balancing Europe's wind-power output through spatial deployment informed by weather regimes. 7(8): 557.

Gregory, J., Dixon, K., Stouffer, R., Weaver, A., Driesschaert, E., Eby, M., Fichefet, T., Hasumi, H., Hu, A. and Jungclaus, J.J.G.R.L., 2005. A model intercomparison of changes in the Atlantic thermohaline circulation in response to increasing atmospheric CO2 concentration. 32(12).

Hannachi, A., Straus, D.M., Franzke, C.L., Corti, S. and Woollings, T.J.R.o.G., 2017. Low-frequency nonlinearity and regime behavior in the Northern Hemisphere extratropical atmosphere. 55(1): 199-234.

https://doi.org/10.5194/gmd-2019-291
Preprint. Discussion started: 26 November 2019
© Author(s) 2019. CC BY 4.0 License.

Hardiman, S.C., Boutle, I.A., Bushell, A.C., Butchart, N., Cullen, M.J., Field, P.R., Furtado, K., Manners, J.C., Milton, S.F. and Morcrette, C.J.J.o.C., 2015. Processes controlling tropical tropopause temperature and stratospheric water vapor in climate models. 28(16): 6516-6535.

Hartley, A., MacBean, N., Georgievski, G. and Bontemps, S.J.R.S.o.E., 2017. Uncertainty in plant functional type distributions and its impact on land surface models. 203: 71-89.

Heimann, M. and Reichstein, M., 2008. Terrestrial ecosystem carbon dynamics and climate feedbacks. Nature, 451(7176): 289-92.

Hurrell, J.W. and Deser, C., 2009. North Atlantic climate variability: The role of the North Atlantic Oscillation. Journal of Marine Systems, 78(1): 28-41.

Ilıcak, M., Drange, H., Wang, Q., Gerdes, R., Aksenov, Y., Bailey, D., Bentsen, M., Biastoch, A., Bozec, A. and Böning, C., 2016. An assessment of the Arctic Ocean in a suite of interannual CORE-II simulations. Part III: Hydrography and fluxes. Ocean Modelling, 100: 141-161.

Juckes, M., Taylor, K.E., Durack, P., Lawrence, B., Mizielinski, M., Pamment, A., Peterschmitt, J.Y., Rixen, M. and Sénésis, S., 2019. The CMIP6 Data Request (version 01.00.31). Geosci. Model Dev. Discuss., 2019: 1-35.

Jung, M., Koirala, S., Weber, U., Ichii, K., Gans, F., Camps-Valls, G., Papale, D., Schwalm, C., Tramontana, G. and Reichstein, M., 2019. The FLUXCOM ensemble of global land-atmosphere energy fluxes. Scientific Data, 6(1): 74.

Kay, J., Deser, C., Phillips, A., Mai, A., Hannay, C., Strand, G., Arblaster, J., Bates, S., Danabasoglu, G. and Edwards, J., 2015. The Community Earth System Model (CESM) large ensemble project: A community resource for studying climate change in the presence of internal climate variability. Bulletin of the American Meteorological Society, 96(8): 1333-1349.

Kleidon, A. and Lorenz, R.D., 2004. Non-equilibrium thermodynamics and the production of entropy: life, earth, and beyond. Springer Science & Business Media.

Koven, C.D., Chambers, J.Q., Georgiou, K., Knox, R., Negron-Juarez, R., Riley, W.J., Arora, V.K., Brovkin, V., Friedlingstein, P. and Jones, C.D., 2015. Controls on terrestrial carbon feedbacks by productivity versus turnover in the CMIP5 Earth System Models. Biogeosciences, 12(17): 5211-5228.

Kumar, S., Merwade, V., Kinter III, J.L. and Niyogi, D.J.J.o.C., 2013. Evaluation of temperature and precipitation trends and long-term persistence in CMIP5 twentieth-century climate simulations. 26(12): 4168-4185.

Kunz, T., Fraedrich, K. and Kirk, E.J.C.d., 2008. Optimisation of simplified GCMs using circulation indices and maximum entropy production. 30(7-8): 803-813.

Kvalevåg, M.M., Myhre, G., Bonan, G. and Levis, S.J.I.J.o.C., 2010. Anthropogenic land cover changes in a GCM with surface albedo changes based on MODIS data. 30(13): 2105-2117.

Kwok, R.J.E.R.L., 2018. Arctic sea ice thickness, volume, and multiyear ice coverage: losses and coupled variability (1958–2018). 13(10): 105005.

Landschuetzer, P., Gruber, N. and Bakker, D.C.J.G.B.C., 2016. Decadal variations and trends of the global ocean carbon sink. 30(10): 1396-1417.

Lauer, A., Eyring, V., Bock, L., Gier, B.K., Lorenz, R., Righi, M., Schlund , M., Senftleben, D. and Weigel, K., 2019. ESMValTool v2.0 – Diagnostics for emergent constraints and future projections from Earth system models in CMIP. Geosci. Model Dev. Discuss., submitted.

Lauer, A., Eyring, V., Righi, M., Buchwitz, M., Defourny, P., Evaldsson, M., Friedlingstein, P., de Jeu, R., de Leeuw, G., Loew, A., Merchant, C.J., Müller, B., Popp, T., Reuter, M., Sandven, S., Senftleben, D., Stengel, M., Van Roozendael, M., Wenzel, S. and Willén, U., 2017. Benchmarking CMIP5 models with a subset of ESA CCI Phase 2 data using the ESMValTool. Remote Sensing of Environment, 203(Supplement C): 9-39.

Lavergne, T., Sørensen, A.M., Kern, S., Tonboe, R., Notz, D., Aaboe, S., Bell, L., Dybkjær, G., Eastwood, S. and Gabarro, C.J.T.C., 2019. Version 2 of the EUMETSAT OSI SAF and ESA CCI sea-ice concentration climate data records. 13(1): 49-78.

Lejeune, Q., Seneviratne, S.I. and Davin, E.L.J.J.o.C., 2017. Historical land-cover change impacts on climate: comparative assessment of LUCID and CMIP5 multimodel experiments. 30(4): 1439-1459.

Lembo, V., Folini, D., Wild, M. and Lionello, P., 2017. Energy budgets and transports: global evolution and spatial patterns during the twentieth century as estimated in two AMIP-like experiments. Climate Dynamics, 48(5-6): 1793-1812.

Lembo, V., Lunkeit, F. and Lucarini, V., 2019. TheDiaTo (v1.0) – A new diagnostic tool for water, energy and entropy budgets in climate models. Geosci. Model Dev. Discuss., 2019: 1-50.

Liepert, B.G. and Previdi, M.J.E.R.L., 2012. Inter-model variability and biases of the global water cycle in CMIP3 coupled climate models. 7(1): 014006.

Liu, C., Allan, R.P. and Huffman, G.J.J.G.R.L., 2012. Co-variation of temperature and precipitation in CMIP5 models and satellite observations. 39(13).

https://doi.org/10.5194/gmd-2019-291
Preprint. Discussion started: 26 November 2019
© Author(s) 2019. CC BY 4.0 License.

Lucarini, V., Blender, R., Herbert, C., Ragone, F., Pascale, S. and Wouters, J., 2014. Mathematical and physical ideas for climate science. Reviews of Geophysics, 52(4): 809-859.

Lucarini, V., Calmanti, S., Dell'Aquila, A., Ruti, P.M. and Speranza, A.J.C.D., 2007. Intercomparison of the northern hemisphere winter mid-latitude atmospheric variability of the IPCC models. 28(7-8): 829-848.

Lucarini, V., Fraedrich, K. and Ragone, F., 2011. New Results on the Thermodynamic Properties of the Climate System. Journal of the Atmospheric Sciences, 68(10): 2438-2458.

Lucarini, V. and Pascale, S., 2014. Entropy production and coarse graining of the climate fields in a general circulation model. Climate Dynamics, 43(3-4): 981-1000.

Lucarini, V. and Ragone, F., 2011. Energetics of Climate Models: Net Energy Balance and Meridional Enthalpy Transport. Reviews of Geophysics, 49.

Mahmood, R., Pielke Sr, R.A., Hubbard, K.G., Niyogi, D., Dirmeyer, P.A., McAlpine, C., Carleton, A.M., Hale, R., Gameda, S. and Beltrán-Przekurat, A.J.I.J.o.C., 2014. Land cover changes and their biogeophysical effects on climate. 34(4): 929-953.

Mantua, N.J., Hare, S.R., Zhang, Y., Wallace, J.M. and Francis, R.C., 1997. A Pacific interdecadal climate oscillation with impacts on salmon production. Bulletin of the American Meteorological Society, 78(6): 1069-1079.

Marques, C., Rocha, A. and Corte-Real, J.J.C.d., 2011. Global diagnostic energetics of five state-of-the-art climate models. 36(9-10): 1767-1794.

Masato, G., Hoskins, B.J. and Woollings, T., 2013. Winter and summer Northern Hemisphere blocking in CMIP5 models. Journal of Climate, 26(18): 7044-7059.

Massonnet, F., Fichefet, T., Goosse, H., Bitz, C.M., Philippon-Berthier, G., Holland, M.M. and Barriat, P.-Y.J.T.C., 2012. Constraining projections of summer Arctic sea ice. 6(6): 1383-1394.

Massonnet, F., Vancoppenolle, M., Goosse, H., Docquier, D., Fichefet, T. and Blanchard-Wrigglesworth, E.J.N.C.C., 2018. Arctic sea-ice change tied to its mean state through thermodynamic processes. 8(7): 599.

Mauritsen, T., Stevens, B., Roeckner, E., Crueger, T., Esch, M., Giorgetta, M., Haak, H., Jungclaus, J., Klocke, D. and Matei, D.J.J.o.a.i.m.E.s., 2012. Tuning the climate of a global model. 4(3).

McCarthy, G., Smeed, D., Johns, W.E., Frajka-Williams, E., Moat, B., Rayner, D., Baringer, M., Meinen, C., Collins, J. and Bryden, H.J.P.i.O., 2015. Measuring the Atlantic meridional overturning circulation at 26 N. 130: 91-111.

Meehl, G.A., Arblaster, J.M., Chung, C.T., Holland, M.M., DuVivier, A., Thompson, L., Yang, D. and Bitz, C.M.J.N.c., 2019. Sustained ocean changes contributed to sudden Antarctic sea ice retreat in late 2016. 10(1): 14.

Meehl, G.A., Boer, G.J., Covey, C., Latif, M. and Stouffer, R.J., 2000. The Coupled Model Intercomparison Project (CMIP). Bulletin of the American Meteorological Society, 81(2): 313-318.

Meehl, G.A., Covey, C., Taylor, K.E., Delworth, T., Stouffer, R.J., Latif, M., McAvaney, B. and Mitchell, J.F.B., 2007. THE WCRP CMIP3 Multimodel Dataset: A New Era in Climate Change Research. Bulletin of the American Meteorological Society, 88(9): 1383-1394.

Mehran, A., AghaKouchak, A. and Phillips, T.J.J.J.o.G.R.A., 2014. Evaluation of CMIP5 continental precipitation simulations relative to satellite-based gauge-adjusted observations. 119(4): 1695-1707.

Michelangeli, P.-A., Vautard, R. and Legras, B.J.J.o.t.a.s., 1995. Weather regimes: Recurrence and quasi stationarity. 52(8): 1237-1256.

Morice, C.P., Kennedy, J.J., Rayner, N.A. and Jones, P.D., 2012. Quantifying uncertainties in global and regional temperature change using an ensemble of observational estimates: The HadCRUT4 data set. Journal of Geophysical Research: Atmospheres, 117(D8).

Myhre, G., Kvalevåg, M.M. and Schaaf, C.B.J.G.R.L., 2005. Radiative forcing due to anthropogenic vegetation change based on MODIS surface albedo data. 32(21).

Notz, D. and Bitz, C.M.J.S.i., 2017. Sea ice in Earth system models. 304-325.

Olason, E. and Notz, D.J.J.o.G.R.O., 2014. Drivers of variability in A rctic sea-ice drift speed. 119(9): 5755-5775.

Phillips, A.S., Deser, C. and Fasullo, J., 2014. Evaluating modes of variability in climate models. Eos, Transactions American Geophysical Union, 95(49): 453-455.

Pitman, A.J., de Noblet-Ducoudré, N., Cruz, F., Davin, E.L., Bonan, G., Brovkin, V., Claussen, M., Delire, C., Ganzeveld, L. and Gayler, V.J.G.R.L., 2009. Uncertainties in climate responses to past land cover change: First results from the LUCID intercomparison study. 36(14).

Poulter, B., MacBean, N., Hartley, A., Khlystova, I., Arino, O., Betts, R., Bontemps, S., Boettcher, M., Brockmann, C. and Defourny, P.J.G.M.D., 2015. Plant functional type classification for earth system models: results from the European Space Agency's Land Cover Climate Change Initiative. 8: 2315-2328.

https://doi.org/10.5194/gmd-2019-291
Preprint. Discussion started: 26 November 2019
© Author(s) 2019. CC BY 4.0 License.

Rampal, P., Weiss, J., Dubois, C. and Campin, J.M.J.J.o.G.R.O., 2011. IPCC climate models do not capture Arctic sea ice drift acceleration: Consequences in terms of projected sea ice thinning and decline. 116(C8).

Rayner, N., Parker, D.E., Horton, E., Folland, C.K., Alexander, L.V., Rowell, D., Kent, E. and Kaplan, A.J.J.o.G.R.A., 2003. Global analyses of sea surface temperature, sea ice, and night marine air temperature since the late nineteenth century. 108(D14).

Reichler, T. and Kim, J., 2008. How well do coupled models simulate today's climate? Bulletin of the American Meteorological Society, 89(3): 303-312.

Rex, D.F.J.T., 1950. Blocking action in the middle troposphere and its effect upon regional climate: I. An aerological study of blocking action. 2(3): 196-211.

Righi, M., Andela, B., Eyring, V., Lauer, A., Predoi, V., Schlund, M., Vegas-Regidor, J., Bock, L., Brötz, B., de Mora, L., Diblen, F., Dreyer, L., Drost, N., Earnshaw, P., Hassler, B., Koldunov, N., Little, B., Loosveldt Tomas, S. and Zimmermann, K., 2019. ESMValTool v2.0 – Technical overview. Geosci. Model Dev. Discuss., 2019: 1-28.

Roemmich, D., Church, J., Gilson, J., Monselesan, D., Sutton, P. and Wijffels, S.J.N.c.c., 2015. Unabated planetary warming and its ocean structure since 2006. 5(3): 240.

Romps, D.M., 2008. The Dry-Entropy Budget of a Moist Atmosphere. Journal of the Atmospheric Sciences, 65(12): 3779-3799.

Russell, J.L., Kamenkovich, I., Bitz, C., Ferrari, R., Gille, S.T., Goodman, P.J., Hallberg, R., Johnson, K., Khazmutdinova, K. and Marinov, I.J.J.o.G.R.O., 2018. Metrics for the evaluation of the Southern Ocean in coupled climate models and earth system models. 123(5): 3120-3143.

Saha, S., Moorthi, S., Wu, X., Wang, J., Nadiga, S., Tripp, P., Behringer, D., Hou, Y.-T., Chuang, H.-y., Iredell, M., Ek, M., Meng, J., Yang, R., Mendez, M.P., van den Dool, H., Zhang, Q., Wang, W., Chen, M. and Becker, E., 2013. The NCEP Climate Forecast System Version 2. Journal of Climate, 27(6): 2185-2208.

Schaaf, C.B., Gao, F., Strahler, A.H., Lucht, W., Li, X., Tsang, T., Strugnell, N.C., Zhang, X., Jin, Y. and Muller, J.-P.J.R.s.o.E., 2002. First operational BRDF, albedo nadir reflectance products from MODIS. 83(1-2): 135-148.

Schlosser, E., Haumann, F.A. and Raphael, M.N., 2018. Atmospheric influences on the anomalous 2016 Antarctic sea ice decay. The Cryosphere, 12(3): 1103-1119.

Serreze, M.C. and Barry, R.G., 2011. Processes and impacts of Arctic amplification: A research synthesis. Global and Planetary Change, 77(1-2): 85-96.

Sheil, D. and Murdiyarso, D.J.B., 2009. How forests attract rain: an examination of a new hypothesis. 59(4): 341-347.

Sillmann, J., Croci-Maspoli, M., Kallache, M. and Katz, R.W., 2011. Extreme cold winter temperatures in Europe under the influence of North Atlantic atmospheric blocking. Journal of Climate, 24(22): 5899-5913.

Simpson, I.R., Deser, C., McKinnon, K.A. and Barnes, E.A., 2018. Modeled and Observed Multidecadal Variability in the North Atlantic Jet Stream and Its Connection to Sea Surface Temperatures. Journal of Climate, 31(20): 8313-8338.

Steele, M., Morley, R. and Ermold, W., 2001. PHC: A global ocean hydrography with a high-quality Arctic Ocean. Journal of Climate, 14(9): 2079-2087.

Stroeve, J. and Notz, D.J.E.R.L., 2018. Changing state of Arctic sea ice across all seasons. 13(10): 103001.

Stroeve, J.C., Kattsov, V., Barrett, A., Serreze, M., Pavlova, T., Holland, M. and Meier, W.N.J.G.R.L., 2012. Trends in Arctic sea ice extent from CMIP5, CMIP3 and observations. 39(16).

Suárez-Gutiérrez, L., Li, C., Thorne, P.W. and Marotzke, J., 2017. Internal variability in simulated and observed tropical tropospheric temperature trends. Geophysical Research Letters, 44(11): 5709-5719.

Taylor, K.E., Stouffer, R.J. and Meehl, G.A., 2012. An Overview of CMIP5 and the Experiment Design. Bulletin of the American Meteorological Society, 93(4): 485-498.

Thompson, D.W.J. and Wallace, J.M., 2000. Annular modes in the extratropical circulation. Part I: Month-to-month variability. Journal of Climate, 13(5): 1000-1016.

Tibaldi, S. and Molteni, F., 1990. On the operational predictability of blocking. Tellus A, 42(3): 343-365.

Trenberth, K.E., Caron, J.M. and Stepaniak, D.P., 2001. The atmospheric energy budget and implications for surface fluxes and ocean heat transports. Climate Dynamics, 17(4): 259-276.

Trenberth, K.E. and Shea, D.J., 2006. Atlantic hurricanes and natural variability in 2005. Geophysical Research Letters, 33(12).

Tschudi, M., Fowler, C., Maslanik, J., Stewart, J., Meier, W.J.N.S. and Ice Data Center Distributed Active Archive Center, a.F., 2016. Polar Pathfinder daily 25 km EASE-Grid Sea Ice motion vectors, version 3.

Ulbrich, U., Speth, P.J.M. and Physics, A., 1991. The global energy cycle of stationary and transient atmospheric waves: results from ECMWF analyses. 45(3-4): 125-138.

UNFCCC, 2015. Report of the Conference of the Parties on its twenty-first session, held in Paris from 30 November to 13 December 2015, available at http://unfccc.int/resource/docs/2015/cop21/eng/10.pdf.

https://doi.org/10.5194/gmd-2019-291
Preprint. Discussion started: 26 November 2019
© Author(s) 2019. CC BY 4.0 License.

Vautard, R.J.M.w.r., 1990. Multiple weather regimes over the North Atlantic: Analysis of precursors and successors. 118(10): 2056-2081.

Volpe, G., Santoleri, R., Colella, S., Forneris, V., Brando, V.E., Garnesson, P., Taylor, B. and Grant, M., 2019. PRODUCT USER MANUAL For all Ocean Colour Products. http://resources.marine.copernicus.eu/documents/PUM/CMEMS-OC-PUM-009-ALL.pdf(2.2): 75pp.

Von Schuckmann, K., Palmer, M., Trenberth, K., Cazenave, A., Chambers, D., Champollion, N., Hansen, J., Josey, S., Loeb, N. and Mathieu, P.-P.J.N.C.C., 2016. An imperative to monitor Earth's energy imbalance. 6(2): 138.

Wallace, J.M. and Gutzler, D.S., 1981. Teleconnections in the Geopotential Height Field during the Northern Hemisphere Winter. Monthly Weather Review, 109(4): 784-812.

Wallace, J.M.J.Q.J.o.t.R.M.S., 2000. North Atlantic oscillatiodannular mode: two paradigms—one phenomenon. 126(564): 791-805.

Weigel, K., Eyring, V., Gier, B.K., Lauer, A., Righi, M., Schlund, M., Adeniyi, K., Andela, B., Arnone, E., Berg, P., Bock, L., Corti, S., Caron, L.-P., Cionni, I., Hunter, A., Lledó, L., Mohr, C.-M., Pérez-Zanón, N., Predoi, V., Sandstad, M., Sillmann, J., Vegas-Regidor, J. and von Hardenberg, J., 2019. ESMValTool (v2.0) – Diagnostics for extreme events, regional model and impact evaluation and analysis of Earth system models in CMIP. Geosci. Model Dev. Discuss., submitted.

Wenzel, S., Cox, P.M., Eyring, V. and Friedlingstein, P., 2014. Emergent constraints on climate-carbon cycle feedbacks in the CMIP5 Earth system models. Journal of Geophysical Research-Biogeosciences, 119(5): 794-807.

Wenzel, S., Cox, P.M., Eyring, V. and Friedlingstein, P., 2016. Projected land photosynthesis constrained by changes in the seasonal cycle of atmospheric CO 2. Nature, 538(7626): 499.

Wild, M. and Liepert, B.J.E.R.L., 2010. The Earth radiation balance as driver of the global hydrological cycle. 5(2): 025203.

Winckler, J., Reick, C.H. and Pongratz, J.J.J.o.C., 2017. Robust identification of local biogeophysical effects of land-cover change in a global climate model. 30(3): 1159-1176.

Yiou, P., Goubanova, K., Li, Z. and Nogaj, M.J.N.P.i.G., 2008. Weather regime dependence of extreme value statistics for summer temperature and precipitation. 15(3): 365-378.

Zhang, J. and Rothrock, D., 2003. Modeling global sea ice with a thickness and enthalpy distribution model in generalized curvilinear coordinates. Monthly Weather Review, 131(5): 845-861.